THE UNIVERSITY OF SHEFFIELD

DOCTORAL THESIS

EEG source imaging for improved control BCI performance

Author:
Aleksandr ZAITCEV

Supervisor:
Dr. Greg COOK
Dr. Wei LIU
Prof. Martyn PALEY
Dr. Elizabeth MILNE

A thesis submitted in fulfillment of the requirements
for the degree of Doctor of Philosophy

in the
Department of Electronic and Electrical Engineering

May 5, 2017

Abstract

Brain-computer interfaces (BCIs) provide means for direct brain-computer interaction, based solely on the user's brain neural activity, commonly captured by Electroencephalography (EEG), and do not rely on any degree of physical movement. From a general perspective the function of BCIs is to discriminate between a limited set of mental states, which the user enters voluntarily or unconsciously. This represents a foundation for various BCI applications such as assistive technologies, including neuroprosthetics and computer control BCIs for disabled users or mental state monitoring systems aimed for emotion, fatigue or workload recognition. A commonly used type of mental tasks for BCI control is imagination of physical movement or motor imagery, which is characterized by the local power deviation occurring in the brain areas responsible for muscles involved in the executed task.

This PhD manuscript is dedicated to the design of motor imagery EEG BCIs with a particular focus on signal processing and classification approaches that incorporate the background knowledge about biophysics and EEG signal generation. These aspects are considered in the EEG source reconstruction process, which estimate the cortical currents during the EEG voltage measurements from head surface. In this work it is shown that the application of the source reconstruction in a BCI signal processing scheme effectively decreases the negative effects of EEG electrode coupling providing for an increase in class separability, given that the cortical areas involved in motor imagery are anatomically segregated. Based on these observations a novel BCI feature extraction method based on source analysis and common spatial patterns (CSP) was proposed and its performance was investigated with a common motor imagery dataset and our own real-time BCI implementation. Our results show that EEG source reconstruction reduces the influence of noise and muscular artifacts, and thus the proposed approach consistently outperforms the conventional BCI sensor feature extraction methods.

Acknowledgements

First of all, I would like to express my sincere gratitude to my research supervisors Dr. Greg Cook and Dr. Wei Liu for their continuous support of my work, their motivation and immense knowledge. They have educated and guided me through both my MSc and PhD theses. I am grateful to Prof. Martyn Paley and Dr. Elizabeth Milne who have supported me at the early stages of my work and expanded my background knowledge of this multidisciplinary research.

Besides, I would like to thank Ivan Nixon and Peter Gray who have initiated a joint project that allowed me to conduct the most valuable part of my research. This practical part of work would not be possible without Dr. James Law who has enabled me to work in Sheffield Robotics laboratory and provided with workspace and equipment. My thanks also goes to Dr. Mahnaz Arvaneh for her time for detailed discussions, valuable advice on signal processing and encouragement.

I thank my fellow colleagues from Communications Research Group for the stimulating discussions and help in preparation for conference presentations and symposiums. Especially I would like to thank my dear friend and colleague James Henshaw for the time we spent working on joint project in Sheffield Robotics. Without his contribution the practical implementation and validation of my BCI system would not be possible.

Last but not the least, I would like to thank my beloved family: my parents for their continuous moral support and encouragement, and my wife for her boundless patience, optimism and faith in me.

Contents

8

List of Figures

List of Abbreviations

ALS	Amyotrophic Lateral Sclerosis
ANN	Artificial Neural Network
AP	Action Potential
AR	Autoregressive
BCI	Brain-Computer Interface
BEM	Boundary Element Method
BOLD	Blood-Oxygen-Level Dependent
BSS	Blind Source Separation
CAR	Common Average Reference
CNS	Central Nervous System
CSF	Cerebro-Spinal Fluid
CSP	Common Spatial Patterns
DASM	Differential Asymmetry
DC	Direct Current
DFT	Discrete Fourier Transform
DWT	Discrete Wavelet Transform
E-NET	Elastic Net
EEG	Electroencephalography
EIT	Eletrical Impendance Tomography
EPSP	Excitatory Postsynaptic Potential
ERD	Event-Related Desynchronization
ERP	Event-Related Potential
ERS	Event-Related Synchronization
FBCSP	Filter Bank Common Spatial Patterns
FDM	Finite Difference Method
FEM	Finite Element Method
FFT	Fast Fourier Transform
FIR	Finite Impulse Response
FLDA	Fisher's Linear Discriminant Analysis
fMRI	Functional Magnetic Resonance Imaging
fNIRS	Functional Near-Infrared Spectroscopy
GCV	Generalized Cross-Validation
HMM	Hidden Markov Model
ICA	Independent Component Analysis
IIR	Infinite Impulse Response

IPSP	Inhibitory Postsynaptic Potential
IRED	Infrared Emitting Diodes
ITR	Information Transfer Rate
LASSO	Least Absolute Shrinkage and Selection Operator
LAURA	Local Autoregressive Average
LDA	Linear Discriminant Analysis
LORETA	Low Resolution Electrical Tomography
M1	Primary Motor Cortex
MEG	Magnetoencephalography
MLP	Multilayer Perceptron
MNE	Minimum Norm Estimates
NLR	Nonlinear Regressive coefficients
NN	Neural Network
OVR	One-Vs-Rest
PCA	Principal Component Analysis
PLV	Phase Locking Value
PM	Premotor Cortex
PPC	Posterior Parietal Cortex
PSD	Power Spectral Density
RASM	Rational Asymmetry
RNASM	Rational Normalized Asymmetry
ROI	Region Of Interest
S1	Primary Somatosensory Cortex
SCP	Slow Cortical Potentials
SL	Surface Laplacian
SMA	Supplementary Motor Area
SMR	Sensorymotor Rhythms
SNR	Signal-to-Noise Ratio
SQUID	Superconducting Quantum Interference Device
SSVEP	Steady-State Visually Evoked Potentials
STFT	Short-Time Fourier Transform
SVM	Support Vector Machines
TFR	Time-Frequency Representation
WMNE	Weighted Minimum Norm Estimates

Chapter 1

Introduction to brain-computer interfacing.

1.1 Introduction and thesis outline.

The human brain represents a complex hierarchical system that governs a broad spectrum of psychophysiological functions constituting human behavior and perception. Such intricate psychological phenomena as memory, generation of movement, anticipation and imagination are generally associated with patterns of information flow between the function-specific brain regions. Access to these mechanisms, their evaluation and interpretation is not only beneficial for exploratory brain research, but also provides for a number of promising applications based on direct brain-machine communication. The development of electroencephalography (EEG) by Hans Berger (Berger 1929), a technique measuring the imprint of brain activity on the scalp, has greatly advanced the understanding of brain functioning over the years, and recently the idea of brain-computer communication channel has become feasible.

The term Brain-Computer Interface (BCI) roots back to the pioneering work of Jaques Vidal, who showed the feasibility of real-time computer control through the interpretation of the user's EEG (Vidal 1973). However, BCI research became an established field only decades later, when progress in cheap computational power provided for the development of more comprehensive analysis tools and sophisticated real-time experimentation paradigms. Since then the amount of BCI-related publications has grown intensively (see figure 1.1). Currently BCI design is a recognized multidisciplinary
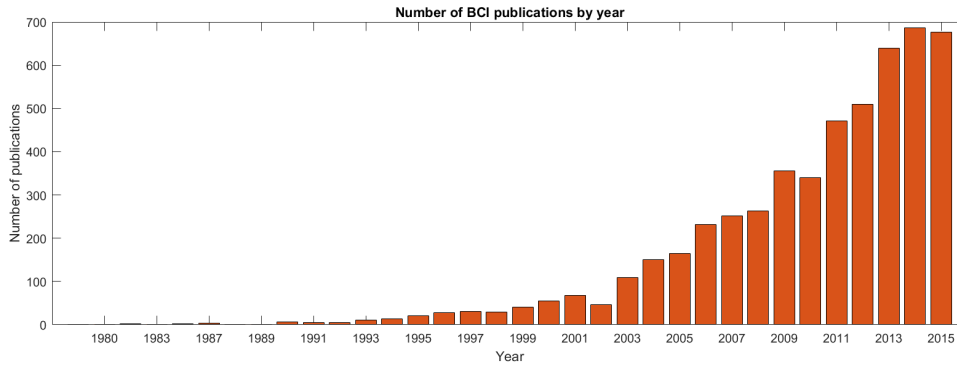
FIGURE 1.1: Number of BCI-related publications per year. The data were obtained by using the PubMed search query for the term "Brain-computer interface" or "BCI".

research field, which integrates researchers from psychology, neuroscience, rehabilitation, computer science, electronics and many other medical and engineering disciplines.

The EEG is produced by a complex mixture of distributed brain cortical activity. Due to volume propagation effects, the EEG suffers from a large degree of inter-electrode coupling, which hinders the interpretation process. A variety of source localization methods aim to reconstruct the cortical current densities that produce the scalp potentials being observed using the biophysics of EEG (Baillet, Mosher, and Leahy 2001). This process significantly alleviates the negative sensor coupling effects and maps the original data onto a source space, where spatial patterns of brain activity are more interpretable from the neurophysiological point of view. Although EEG source analysis is complicated, relying on a propagation model that incorporates multiple design parameters, it is highly beneficial to of mental state classification, and recently, due to the increase in the available computational power, it became applicable in practical real-time BCI applications, as will be shown in this thesis.

The performance of a control BCI can generally be quantified using the measure of information transfer rate (ITR). According to (Pierce 1980) the ITR can be calculated as follows:

$$B = \log_2 N + P \log_2 P + (1 - P) \log_2 \frac{1 - P}{N - 1} \ (bits)$$
$$ITR = \frac{B}{T} \ (bits/min),$$

(1.1)

where N is the number of detectable brain states, P is the accuracy of their detection and T is time required to cast a single control command.

Essentially the motivation of this work is to improve the ITR of existing control BCI systems by focusing on the increase in classification reliability (P in equation 1.1). In our approach this was achieved by addressing the spatial resolution of EEG signal using the source reconstruction technique. In summary, this PhD manuscript is dedicated to the design of EEG BCIs with a particular focus on signal processing and classification approaches that incorporate electromagnetic source analysis. The work in this thesis is aimed towards the following objectives:

- Design an EEG BCI signal processing and classification system employing the background knowledge about biophysics and EEG signal generation.

- Investigate the effects of source reconstruction on indicative signal features in EEG BCIs based on imagination of movement.

- Validate the performance of the proposed source analysis approach with practical real-time motor imagery BCI implementation.

The rest of this chapter gives an overview of the fundamental aspects of BCI design, including general BCI architecture, available signal modalities and approaches for BCI control. The remaining part of the thesis is focused on EEG signal processing and classification techniques applicable in motor imagery BCIs. The general sequence of EEG BCI signal processing, including pre-processing, feature extraction, selection and classification is discussed in Chapter 2. Next, in Chapter 3 we present the framework of electromagnetic head modelling and show the steps necessary to solve the forward problem of EEG source localization. Chapter 4 then gives a brief overview of inverse solutions and, based on simulation scenarios, characterizes the capabilities of an EEG imaging system. In Chapter 5 the previously described techniques are combined in a BCI signal processing system. Here the benefits of source representation in EEG

classification accuracy are evaluated using a well-known motor imagery dataset from BCI competition IV (Brunner et al. 2008). In Chapter 6 the proposed EEG processing and classification method is then demonstrated on a real-time control BCI implementation. This chapter describes the source-based EEG feedback system applied to the user's BCI training.

List of contributions.

- Zaitcev, A., Cook, G., Liu, W., Paley, M., & Milne, E. (2015). Source Localization for Brain-Computer Interfaces. In *Brain-Computer Interfaces* (pp. 125-153). Springer International Publishing.

- Paley, M., Kaka, S., Hilliard, H., Zaytsev, A., Bucur, A., Reynolds, S., Cook, G. (2015). Advanced fMRI and the Brain Computer Interface. In *Brain-Computer Interfaces* (pp. 185-213). Springer International Publishing.

- Zaitcev, A., Cook, G., Liu, W., Paley, M., & Milne, E. (2014, November). Application of compressive sensing for EEG source localization in Brain Computer Interfaces. In *Antennas and Propagation Conference (LAPC)*, 2014 Loughborough (pp. 272-276). IEEE.

- Zaitcev, A., Cook, G., Liu, W., Paley, M., & Milne, E. (2015, May). Feature extraction for BCIs based on electromagnetic source localization and Common Spatial Patterns. In *2015 9th European Conference on Antennas and Propagation (EuCAP)* (pp. 1-5). IEEE.

- Zaitcev, A., Cook, G., Liu, W., Paley, M., & Milne, E. (2015, August). Feature extraction for BCIs based on electromagnetic source localization and multiclass Filter Bank Common Spatial Patterns. In *2015 37th Annual International Conference of the IEEE Engineering in Medicine and Biology Society (EMBC)*(pp. 1773-1776). IEEE.

To be published:

- Zaitcev, A., Cook, G., Liu, W. (2017). Source analysis in real-time motor imagery EEG BCI applications. In *EEG Signal Processing*, IET book chapter.

- Zaitcev, A., Henshaw, J., Cook, G., Liu, W. (2017). Design of asynchronous real-time motor imagery BCI based on EEG source imaging.

1.2   BCI application areas.

In the early years of feasibility research and first implementations, the BCIs were mainly considered as an assistive communication and control device for disabled users. Although this area remains in the focus of BCI research, in the past decade a number of other promising BCI applications have emerged. With respect to how the BCIs are related to the normal body functions they can be classified into one of the categories whether their task is to *replace*, *improve*, *restore*, *enhance* various aspects of body functioning or provide data for the further BCI research. This classification was proposed by the BNCI Horizon 2020 project which incorporates the leading BCI research institutions and representatives from industry (Brunner et al. 2015). According to this classification and the relevant overview presented in (Blankertz et al. 2016), BCIs can be used in the following application scenarios:

Replace   BCIs can be applied to *replace* the natural CNS function that has been lost or impaired due to disease or injury. This category includes the majority of assistive BCIs aimed to provide means for communication (text spelling, speech synthesis) and device control (computer, wheelchair, environmental controller). A comprehensive overview of this application field and descriptions of such assistive BCI implementations can be found, for example, in (Cincotti et al. 2008; Carlson and Millan 2013; Rupp et al. 2014).

Improve   In many cases BCIs can be used as part of rehabilitation programme supporting the gradual *improvement* of natural CNS functions impaired as a result of stroke or injury. In such a scenario the role of the BCI user is to perform certain motor exercises, i.e attempt the normal CNS function. The BCI purpose then is to decode and enhance signals from the damaged brain area and reward the correct execution, for example, by supporting electrical stimulation of muscles involved in the task. An overview of this application area can be found in (Daly and Wolpaw 2008; Ang and Guan 2016).

Restore   BCIs can be used to bypass the natural CNS pathways and thus *restore* lost motor functions. Such assistive systems generally

rely on functional electric stimulation of muscles or robotic devices such as exoskeletons to drive the user limbs according to the user intent decoded directly from the brain signals (Collinger et al. 2013; Frolov et al. 2017).

Enhance   BCIs can potentially *enhance* the normal CNS function. Examples include various passive BCIs that do not rely on the user intent for control, but continuously monitor the brain state and provide metrics such as levels of attention, fatigue or stress. Such BCIs can be applied, for example, to alert the user of detected lapses of attention during prolonged demanding tasks (Gerjets et al. 2015), enhance the user reaction times in emergency situations (Haufe et al. 2011), or enhance the user learning capabilities (Galway et al. 2015).

Entertainment   In the past decade BCI technology has become a subject of interest for a larger audience and a number of non-medical applications have emerged. BCIs can be utilized by healthy able-bodied users to provide additional means for control, for example, in gaming. Besides, various measures of cognitive state such as emotion, attention and others can be used to adapt and optimize the entertainment experience to a specific user (Blankertz et al. 2010; Ahn et al. 2014).

Research tool   BCIs can be also viewed as a research tool that provides additional insight about the CNS functioning.

1.3   Neurophysiological basis for BCI control.

Generally speaking, BCIs provide the means for human-computer interaction based solely on the user's brain neural activity. Depending on the application, BCIs can be *passive*, producing continuous output regardless of the user's intent, or *active*, relying on the voluntary self-regulation of the brain.

In passive BCIs the system generally aims to produce various metrics of the brain state such as mental fatigue level, emotional

state, working memory load that can be used for ongoing monitoring in an effort, for example, to reduce the risks connected to the human factor (Muller et al. 2008; Summerer, Izzo, and Rossini 2009; Borghini et al. 2014). However, in the current state BCI research is mainly focused on the design of active interfaces that provide the means for communication and control. Since the BCIs do not rely on any degree of physical movement, it makes them an advantageous assistive technology for individuals severely lacking physical capabilities, such as ALS patients and individuals recovering from stroke (Nicolas-Alonso and Gomez-Gil 2012). Such active BCIs rely on the brain signals that are voluntarily (or semi-voluntarily) elicited by the user as a result of performing certain mental tasks such as imagination of movement, mental arithmetics or visual attention.

From the user's perspective the execution of a BCI command is done by performing a certain task, that produces indicative physical effects in the brain. This task can be voluntary, performed consciously by the user at any arbitrary time, or semi-voluntary, which corresponds to shifting of user's attention to an external stimulus. There are a number of known approaches to BCI signal generation, each associated with characteristic physical effects, such as increase/decrease of power in a certain brain area, presence of specific spectral components, time-domain sequence of amplitudes and numerous other more complex effects. Consequently, the choice of control tasks largely defines the overall system architecture, as the BCI signal processing sequence must be tailored with respect to the physics accompanying the particular type of control intent. In this context prior knowledge about the EEG physics underlying the BCI task execution is highly valuable, as it justifies the choice of signal processing elements and, besides, can provide regularization priors for the pattern recognition stage. In this section we will discuss various neurophysiological effects that are commonly used in active control BCIs, including SSVEP, P300, slow cortical potentials and sensorimotor rhythms.

1.3.1 Exogenous BCIs.

A BCI system which relies on the presence of external stimuli is often referred to as exogenous BCI. Most commonly the external stimuli is represented by a set of specific visual landmarks on the screen, that induce the detectable changes in brain neural activity when visually observed (Nicolas-Alonso and Gomez-Gil 2012). However, the use of auditory (Nijboer et al. 2008; Schreuder, Rost, and Tangermann 2011), tactile (Brouwer and Van Erp 2010; Mori et al. 2012) stimuli and their combinations (Aloise et al. 2007; Mori et al. 2013) have also been shown to be viable options for control BCI basis. In the following sections we will give an overview of the most popular types of exogenous BCI control signals, namely P300 and steady-state visually evoked potentials (SSVEP).

P300 response.

P300 response refers to a specific waveform component that is considered to reflect the brain processes linked to stimulus interpretation. This waveform component, or event-related potential (ERP), is an evident positive deflection on the EEG that occurs 250-400 ms after the *unexpected* stimulus is presented to the subject, hence the name of the effect. The amplitude of P300 depends on how unexpected the stimulus is, i.e., stimulus with the lowest probability of occurrence produces the strongest P300 response. An important advantage of P300 BCI, which makes it feasible for practical applications, is that it requires very little user training and does not involve any cognitive tasks during the operation.

An example of how this effect is employed in BCIs can be demonstrated on a very common P300 speller application, that aims to provide text input means based solely on the user's EEG. The BCI user is presented with a visual interface consisting of a symbol matrix with columns and rows alternatively flashed for a short duration (see figure 1.2). The user's role here is to focus their visual attention on a particular symbol to be typed and wait for a flicker. The flashing of adjacent symbols that are not selected corresponds to common events, causing weak P300 deflections. The anticipated flicker of a selected target corresponds to an improbable event, and hence it results

P3–SPELLE_

A	B	C	D	E	F
G	H	I	J	K	L
M	N	O	P	Q	R
S	T	U	V	W	X
Y	Z	1	2	3	4
5	6	7	8	9	-

FIGURE 1.2: Example of a P300 speller interface. Rows and columns of symbols are flashed alternatively. The user's role is to focus their visual attention on a particular target and wait for flicker. (Image from (Marchetti and Priftis 2015), published under CC BY license v3.0.)

in a stronger P300 response. With precise deterministic stimulation timing it is then possible to infer the user's selection by correlating the row and column flashing times and the instances of strong P300 occurrence.

The practical P300 BCI implementations generally achieve information-transfer rates (ITR) in the range of 20-70 bits/min (Yuan et al. 2013) with high accuracies of 80-97%. However, despite the high classification reliability these types of BCIs suffer from a number of drawbacks, such as low responsiveness due to long flash waiting periods, GUI limitations and user fatigue after lengthy sessions (Amiri et al. 2013).

Steady-state visually evoked potentials.

The rapid visual stimulation by flickering light sources with stable constant frequency of more than 3.5 Hz is known to elicit a specific component on the EEG called steady-state visually evoked potential (SSVEP). This effect originates in the visual cortex, which is located
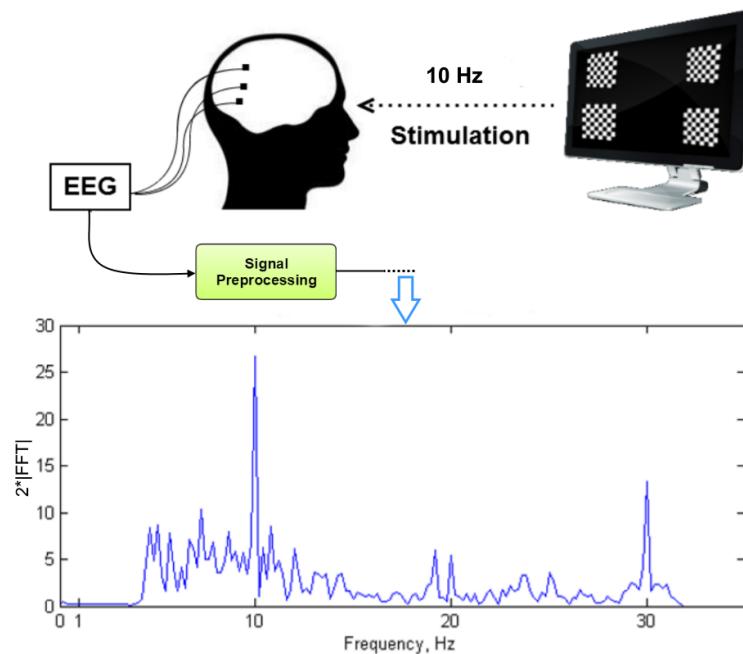
FIGURE 1.3: Principle of SSVEP BCI and an example of
typical 10 Hz SSVEP response illustrated by the spectrum of band-pass filtered EEG from a single sensor
Oz. On the spectrum there are evident peaks at the
fundamental stimulation frequency (10Hz) and its two
harmonics.

in the occipital area of the brain, and is characterized by the presence of strong spectral peaks at the frequency of visual stimulation
and its 2 harmonics. By focusing the visual attention on a particular
stimulus with unique flickering frequency the user induces SSVEP
at this frequency plus harmonics, and hence the stimulus selection
can be inferred from the EEG spectrum (see figure 1.3). By allocating
the displayed stimuli to particular computer commands (text input,
mouse movement) it is then possible to implement computer control requiring only eye movement. From the perspective of user's
cognition the generation of SSVEP is completely passive, i.e., does
not employ any mental tasks or concentration, and therefore SSVEP
BCIs do not require any user training, which is highly beneficial for
practical applications.

In its current state SSVEP BCIs represent the fastest and most reliable type of non-invasive neural interface, with ITR of up to 192
bits/min in recent implementations (Amiri et al. 2013; Nakanishi et

al. 2014). The one major drawback of SSVEP stimulation is that it quickly induces visual fatigue, as reported by many users. However, it was also found that higher stimulation frequencies of 20 Hz and more are much less visually exhausting and, hence, this negative effect can be alleviated by using stimuli with high flickering rate (Wang, Wang, and Jung 2010).

1.3.2　Endogenous BCIs.

Endogenous BCIs represent a class of neural interfaces that do not rely on any degree of external stimulation. With such BCIs the user must perform certain mental tasks that encode the control intent and modulate the brain activity in a distinguishable manner. In such settings the execution of a control command is a complex task for the unprepared user, resulting in high inter-trial variability of observations within individual classes. Therefore, endogenous BCIs require a certain degree of user training, which is generally conducted within a trial-based and cue-driven paradigm relying on a visual feedback to indicate the successful classification. For different users such training may take from several weeks to a few months. In the next sections we will introduce the most common approaches for endogenous BCI control.

Slow cortical potentials.

Another common neurophysiological basis for BCI control are slow cortical potentials (SCP), which correspond to the class of event-related potentials (ERP). Unlike the rhythmic brain activity (mu, alpha, beta, delta waves) the ERPs do not appear spontaneously, but are time-locked to the onset of some event. In case of SCPs such event is the user's intent for brain self-regulation, which is an endogenous activity, i.e., comes from within the user. From a cognitive perspective, SCPs are associated with mechanisms underlying anticipation, attention and planning. The user's ability to voluntarily modulate SCPs typically forms gradually within several weeks of regular visual feedback training (Birbaumer et al. 2003).

From a technical point of view SCPs represent slow DC shifts on the EEG originating in upper cortical layers of the brain. In SCPs the word "slow" stands for the long duration of this effect with detectable current shifts occurring roughly 300 msec after the onset of task execution. The fact that SCPs are characterized by direct current shifts makes their robust detection a challenging task, since the low frequency spectrum components of the EEG are vulnerable to noise and artifacts, such as DC drifts, breathing, heart beat and eye movement. Trained SCP BCI users generally achieve a relatively low ITR of 5-12 bits/min in trial-based feedback training sessions (Nicolas-Alonso and Gomez-Gil 2012; Garipelli, Chavarriaga, and R Millán 2013).

Sensorimotor rhythms.

In 1989 G. Pfurtscheller shown, that nearly all humans can voluntarily modulate their sensorimotor rhythms (SMR) associated with
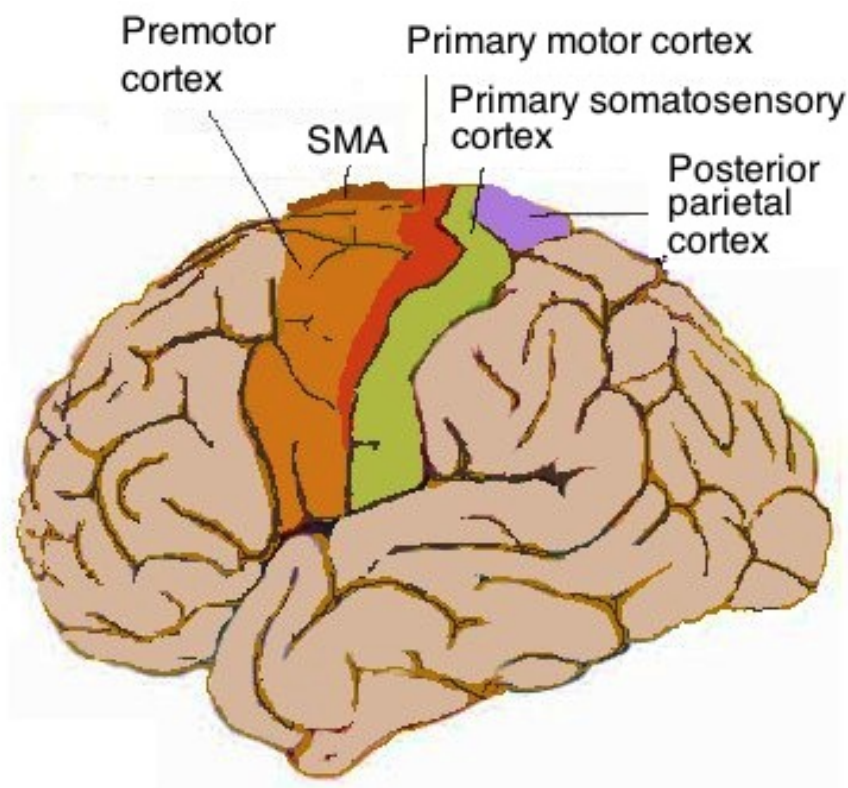
FIGURE 1.4: Anatomy of human motor cortex. Image from Wikipedia.

imagination of movement (Pfurtscheller 1989). Considering the human capabilities for SMR training (Kuhlman 1978) and that these rhythms originate from the localized cortical area related to motor functions (Pfurtscheller et al. 2006), imagination of movement was accepted as a suitable control signal for a BCI. More specifically, SMR BCIs utilize the detection of event related desynchronization/synchronization (ERD/ERS) effects during the imagination of movement. Here event related desynchronization (ERD) represents the suppression of rhythm amplitude and event related synchronization denotes the amplitude increase. The spatial patterns of ERD/ERS effects occurring in mu (7-13 Hz) and beta (16 -31 Hz) bands of the EEG can directly indicate the muscles involved in the imaginary task being performed (Pfurtscheller et al. 2006; Kaiser et al. 2014). Hence by finding the motor cortex areas that generate the signal of interest it is possible to infer the imagined type of movement and execute the BCI command associated with it.

Within the conceptual framework of motor hierarchy, the limb control is seen as a set of hierarchically arranged functions that are performed in series by a set of brain regions with dedicated functional roles. Anatomically such hierarchy is considered to be comprised of the following brain areas (see figure 1.4): premotor cortex (PM), supplementary motor area (SMA), primary motor cortex (M1), primary somatosensory cortex (S1), posterior parietal cortex (PPC) (Wolpaw and Wolpaw 2012). Figure 1.5 shows the modern reproduction of the famous Penfield's cortical sensory "homunculus", which is the mapping of various body sensory functions to the corresponding S1 regions. According to (Wolpaw and Wolpaw 2012) the imagination of movement modulates the corresponding areas of S1, while the execution of movement is more closely associated with the activity of the muscle-specific regions of M1.

The normal motor activity can be seen as a sequence of planning, followed by the actual movement execution. Hence, the task of an

SMR BCI user is to perform the comprehensive planning of movement, including limb positioning and sequence of muscular contractions, while inhibiting the actual motor execution. During this process the imagined configuration of activated muscles defines the information transfer between the functional regions of the motor cortex and the resulting topography of ERD/ERS effects in mu and beta bands or their sequences. In order to modulate the SMR the BCI user must repetitively perform kinesthetic imagery of the particular motor task, i.e., imagine the limb positioning and tactile feeling of the it, but not the visual aspects of execution. It is considered that within
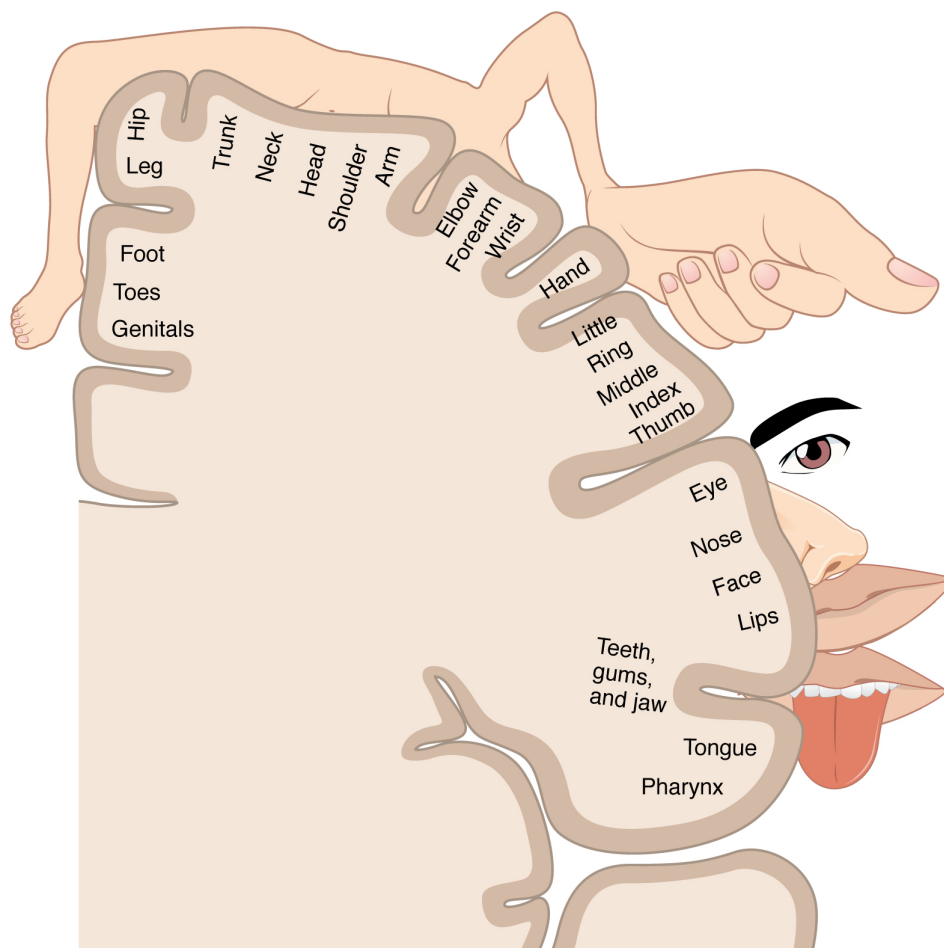
FIGURE 1.5: Penfield's cortical sensory "homunculus". Represents the mapping of body sensory functions to the corresponding areas in primary somatosensory cortex (S1). (Illustration from Anatomy and Physiology, Connexions Web site, under CC BY 3.0. http://cnx.org/content/col11496/1.6/)

this process the motor planning modulates the rhythmic activity in the premotor cortex, tactile imagination affects the somatosensory cortex and muscle selection causes the patterns of ERD/ERS effects in the primary motor cortex (Wolpaw and Wolpaw 2012). Motor imagery tasks most commonly applied in BCIs usually include imagination of left hand, right hand, feet and tongue movement. The rationale for such task selection comes from the evidence that the primary motor cortex areas associated with muscles involved in these tasks are spatially segregated, therefore the resulting spatial patterns are more distinguishable.

The SMR BCIs currently represent the most popular type of asynchronous, endogenous BCIs with ITR rates between 3 and 35 bits/min (Nicolas-Alonso and Gomez-Gil 2012). While features commonly used to describe the SMR modulation are quite robust to noise and artifacts, the main obstacle for reliable classification is the complexity of consistent imagery task execution. Besides that, motor imagery commands impose a certain cognitive disconnect in a sense, that the user must perform mental tasks not related to the application context (for example, the user must imagine squeezing a tennis ball with the right hand in order to move the mouse cursor to the right). Therefore, the further development of robust SMR BCIs requires not only the application of advanced signal processing and classification techniques, but also the design of adaptive and flexible feedback training protocols.

1.4   General BCI architecture.

The architecture of a BCI signal processing scheme is constituted by several elements, which represent essential processing steps on the path from raw EEG sensor data to an executed BCI command (Figure 1.6). After the initial signal acquisition and preprocessing, which usually includes data stream control, segmentation, frequency and spatial filtering, the feature extraction stage follows, the purpose of which is extraction of distinctive physical properties of the EEG that are indicative of the mental task being performed. In order to achieve
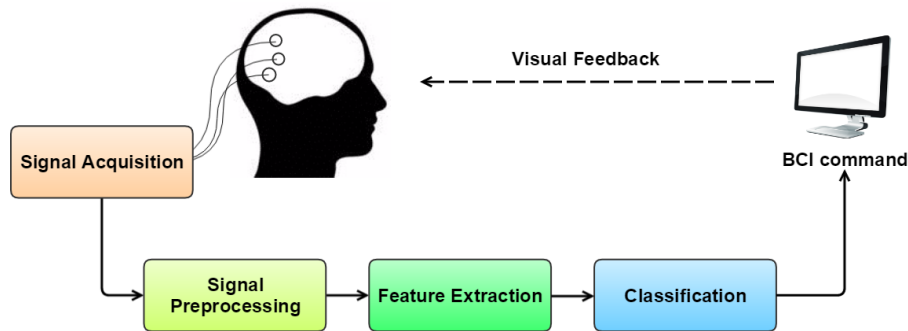
FIGURE 1.6: Common BCI functional architecture.

high classification reliability, the BCI features must effectively encode the user commands and should not contain or at least minimize noise that can hinder the classifier. The identification of such signal properties and numerical methods for their extraction has been in the focus of BCI research since the first prototype implementations. Examples of widely applied BCI features representing the time and frequency domain signal characteristics are logarithmic band power (logBP), various wavelet-based methods and autoregressive parameters (Boostani et al. 2007; Brunner et al. 2011).

Finally, at the classification stage a vector of signal features is translated into one of the possible software commands. The classifier makes an interpretation decision based on a statistical model estimated from a sufficient number of signal observations. Examples of classification algorithms widely used in BCIs are Support Vector Machines (SVM), Linear Discriminant Analysis (LDA), Naive Bayes classifier and Neural Networks (NN) (Boostani et al. 2007; Garrett et al. 2003). In control BCIs, after the feature vector is interpreted by a classifier there also must be visual feedback, which informs the user of the classification results. Besides being part of a graphic interface, such visual indication facilitates the users BCI training process required for many types of BCIs.

1.5 Signal acquisition systems.

As explained previously, the purpose of a BCI system is to provide control capabilities based solely on the user's brain neural activity.

In context of BCI architecture the signal acquisition systems aim to continuously capture various physical effects underlying the user's intent for BCI control.

1.5.1   Electroencephalography.

Electrical activity of the brain can be obtained non-invasively by the means of Electroencephalography or EEG. This technology originates from the pioneering work of Hans Berger, who expanded the previous findings in the area of bioelectricity and recorded the first ever human EEG in 1924 (Millett 2001; Berger 1929). The EEG signal is recorded by a number of metal electrodes and conductive media and represents a multichannel continuous voltage measurement from multiple locations over the surface of the human head. The individual electrode signal is recorded as an electrical potential difference between the given electrode and some reference ground.

The EEG has been repeatedly shown to be a suitable basis for BCIs and currently remains the most popular recording modality
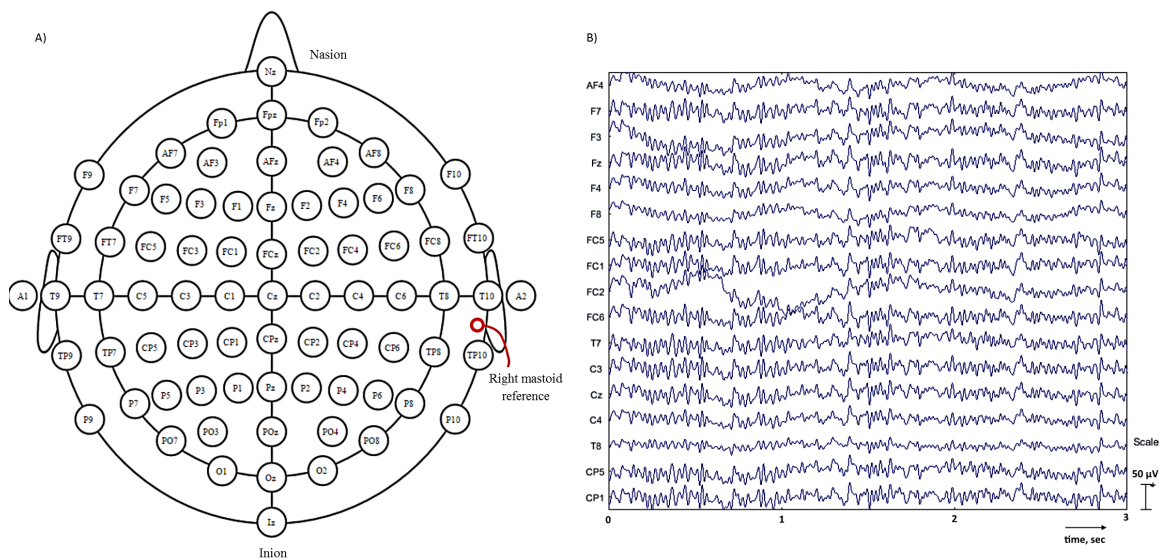
FIGURE 1.7: A) Illustration of standard 10-20 electrode placement scheme with electrode position labels and anatomical references (based on image by Marius't Hart, www.beteredingen.nl, CC BY 3.0). B) Example a 3 second segment of EEG signal from several monopolar channels with common reference at the right mastoid.

for direct brain-computer interaction due to a number of strong advantages (Nicolas-Alonso and Gomez-Gil 2012; Future BNCI Project 2012). The current flow generated during synaptic excitations of large neuronal populations is momentarily picked up by the EEG, yielding an outstanding temporal resolution on the order of milliseconds. Besides that, this acquisition technique is by far the most affordable and compact compared to alternatives, which provides the basis for BCI applications in practical settings, outside of the laboratory. However, the brain activity signal obtained by the EEG is very weak and diffuse, since the electric field passes different tissue types on the path to the electrodes. This results in strong cross-electrode coupling, meaning that in practice the signal of interest from any brain region is observed at all of the EEG channels, albeit in different proportions. The amplitudes of measured biosignals are in the order of microvolts, hence the EEG systems are highly sensitive to external electrical noise, caused for example by the power lines, as well as to internal noise sources associated with acquisition hardware (thermal, burst noise).

Further we will use the following notation for the EEG signal:

$m(t)$ - signal from a single EEG channel,

$\boldsymbol{m}(t)$ - multichannel EEG signal,

$\mathbf{M}$ - matrix, representing a finite block of multichannel EEG data.
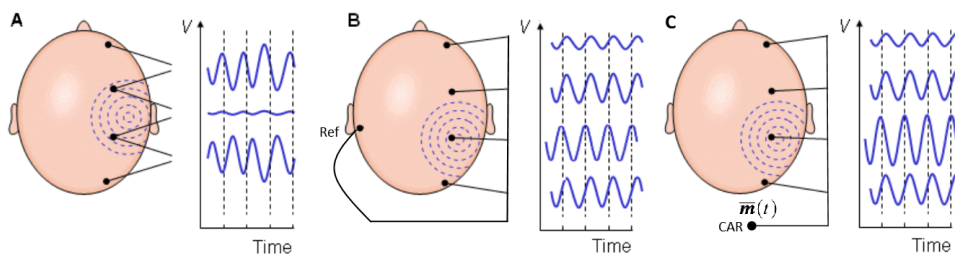
FIGURE 1.8: Different schemes of EEG channel organization. A) Bipolar channels. B) Monopolar channels with common reference electrode. C) Common Average Reference (CAR) channels. Illustration is based on image from (Malmivuo and Plonsey 1995).

EEG reference and channel organization.

The choice of the EEG reference highly affects the measured voltage amplitudes and their scalp distribution. Each EEG channel shows voltages between the given electrode and a reference point, which is typically an additional electrode placed near the main group. Channels organized in this manner are called monopolar:

$$\boldsymbol{m}(t) = \boldsymbol{m}_{scalp}(t) - m_{ref}(t) \ , \qquad (1.2)$$

where $\boldsymbol{m}_{scalp}(t)$ are scalp potentials and $m_{ref}(t)$ represents potential at the reference. The rationale for the common reference electrode placement follows from the purpose of the EEG recording – analysis of electrical **brain** activity. The desirable ground reference must be responsive to the global voltage changes, hence located as close as possible to the EEG electrodes. At the same time the reference ground must be inert to the brain activity, in order to avoid the cancellation of useful signal. As a result the common reference is typically placed over the mastoids, earlobes or nasion.

Besides that, the signal can be recorded as a voltage between two individual electrodes, which is referred to as a bipolar channel. The multichannel signal is then organized as a potential difference of two selected electrode groups:

$$\boldsymbol{m}(t) = \boldsymbol{m}_{group1}(t) - \boldsymbol{m}_{group2}(t) \ , \qquad (1.3)$$

This channel organization is typically used in clinical applications, since it provides a better signal to noise ratio (SNR) in low density electrode montages.

Alternatively, some EEG equipment allows the acquisition of signal with Common Average Reference (CAR), in which case the individual monopolar channels represent the electrical potential difference between a particular electrode and the grand average of potentials at all electrodes:

$$\boldsymbol{m}(t) = \boldsymbol{m}_{scalp}(t) - \overline{\boldsymbol{m}}_{scalp}(t) \qquad (1.4)$$

1.5.2 Magnetoencephalography.

Magnetoencephalography (MEG) is an alternative non-invasive technology capable of measuring physical effects produced by macroscopic brain currents. However, in contrast to the EEG this acquisition technique detects brain activity through magnetic induction. The neurophysiological basis underlying such magnetic field generation is identical to the one producing the EEG signal. Consequently, the MEG provides good temporal resolution similar to the EEG. However, compared to the EEG, MEG is less sensitive to secondary current sources, and hence less susceptible to distortion caused by different tissue types, which yields a higher spatial resolution.

The MEG obtains the biosignal through magnetic induction utilizing multiple superconducting quantum interference devices (SQUIDs). This type of magnetic sensors requires superconductivity, which is achieved by cooling its circuits to temperatures close to absolute zero. The magnetic flux density of the fields measured by MEG is generally as low as 10^{-9} to 10^{-6} Tesla, hence this recording technique needs comprehensive shielding from external interference, which in combination with the requirement for superconductivity and physical size of the equipment limits the use of MEG to stationary laboratory settings. Nevertheless, the outstanding spatio-temporal resolution of the MEG signal was shown to be advantageous in a number of MEG-BCI studies (Lal et al. 2005; Kauhanen et al. 2006; Mellinger et al. 2007). It was reported that MEG-based signal acquisition, significantly reduces the user's training times and facilitates a more reliable and responsive BCI control. Besides that, a number of parallel MEG-EEG studies have offered an additional insight into the neurophysiological phenomena behind the BCI control signal generation (Ahn et al. 2013; Chang et al. 2015), which provides a valuable input for the BCI research community.

1.5.3 Functional magnetic resonance imaging.

Functional Magnetic Resonance Imaging (fMRI) is a non-invasive imaging technology capable of capturing the local hemodynamic changes in various tissues. The signal is obtained using strong magnetic fields

of 3T to 9.4T. The acquisition equipment is physically large and expensive, requiring a complex cooling system generally based on liquid helium circulation in order to facilitate such high magnetic fields. Typically, the fMRI data represents the continuous variation of local blood flow, volume or local blood oxygenation levels. This acquisition technique is characterized by a high spatial resolution of 1mm, and hence it is commonly utilized for localization of active brain regions. The principle of fMRI imaging is based on the link between the neuronal activation and cerebral blood flow. Brain neuronal activity requires glucose and oxygen delivered to the cells, which in its turn requires an increased blood flow in the active region. The presence of oxygen in the blood modulates its magnetic properties, specifically how fast its molecules lose magnetization after being exposed to high magnetic fields. This principle substantiates the Blood-Oxygen-Level Dependent (BOLD) contrast signal acquisition, which is a primary fMRI modality in the context of BCI research.

However, the fMRI BOLD signal suffers from a low temporal resolution of 1-2 seconds. In combination with the physiological delay of 3 to 6 seconds occurring between the neuronal activation and characteristic hemodynamic response, this represents a major drawback for real-time fMRI-based applications. An additional obstacle for practical fMRI BCIs is the fact the subject must remain immobile ideally for the whole recording duration, which becomes exhausting for the user after several minutes. Despite the drawbacks, there have been a number of successful fMRI-based BCI implementations reported in the past decade following the development of real-time fMRI (Weiskopf et al. 2004; Lee et al. 2009; Ruiz et al. 2014). The typical information transfer rate of such implementations is between 60 and 120 bit/min, which is comparable to the ITR of EEG-based systems (Ruiz et al. 2014; Ward and Mazaheri 2008).

1.5.4   Functional near-infrared spectroscopy.

Functional near-infrared spectroscopy (fNIRS) is an optical neuroimaging technique, which uses infrared light to measure hemodynamics within a thin cortical surface layer. This acquisition method was first described nearly four decades ago in (Jöbsis 1977). However, fNIRS
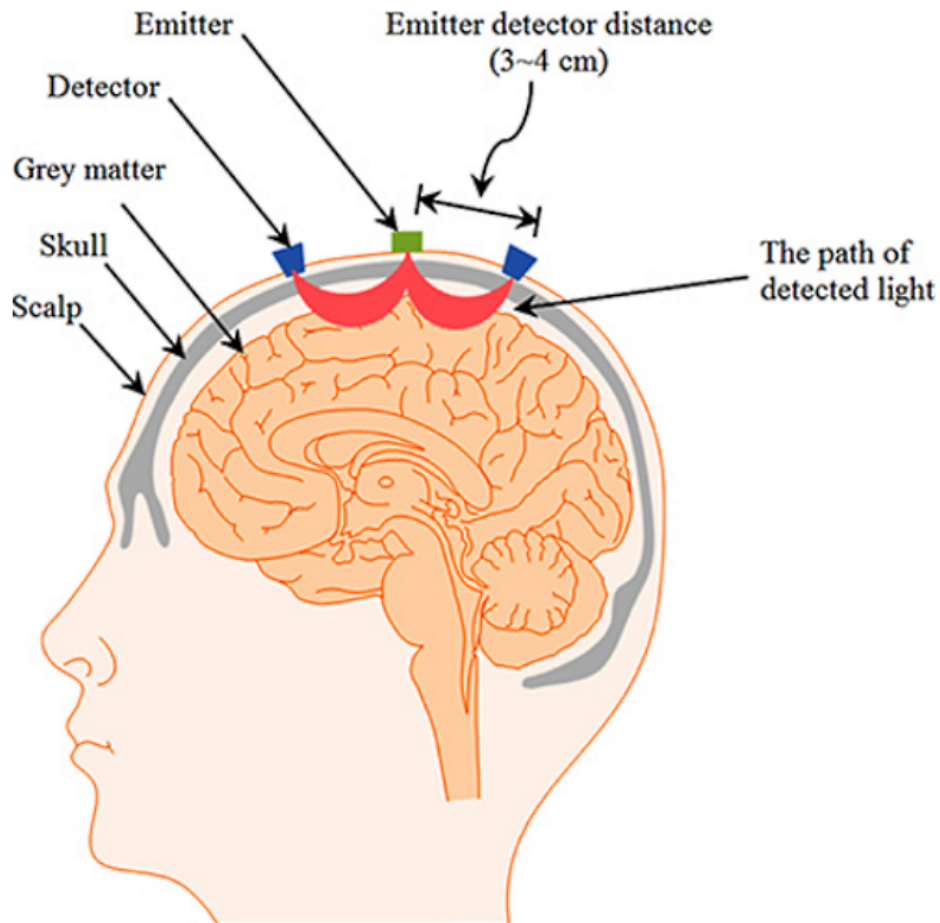
FIGURE 1.9: Principle of fNIRS signal acquisition.
Based on image from (Naseer and Hong 2015) published under CC BY 4.0.

is relatively new to the BCI design area with the first feasibility study reported in 2004 (Coyle et al. 2004). The signal acquisition equipment is comprised by a set of infrared emitting diodes (IREDs), each paired with a light detector tuned to the emitted wavelength (see figure 1.9). The infrared light propagates within 1-4 cm of the skull surface, which is similar to the EEG limiting the biosignal acquisition to a thin brain surface layer. The intensity of light penetrating brain tissues is modulated by the local oxygenation levels, providing for the acquisition of vascular response to brain activity with a physiological delay identical to fMRI. Another issue associated with fNIRS is the sensitivity of signal to subject's motions, producing characteristic spike noise patterns. These motion artifacts can be ameliorated by

ensuring tight optode-skin contact, for example by the means of helmets, individually molded to the subject's head geometry or fibers embedded in neoprene rubber forms (Strangman, Boas, and Sutton 2002).

Compared to fMRI, the fNIRS is much more affordable, portable and has a higher temporal resolution in the order of 100 ms, which satisfies the requirements for practical control BCI applications. Besides, due to the optical signal modality, fNIRS data is not susceptible to electrical noise as in EEG or MEG. Currently fNIRS is the only non-invasive and portable BCI biosignal acquisition method alternative to EEG, and is the only portable and affordable way to obtain brain hemodynamic response. Currently EEG remains the primary signal modality in BCI research, but the popularity of fNIRS in BCI applications has been increasing in the past few years (Naseer and Hong 2015). The practical realizations of fNIRS-based BCIs achieved information transfer rates similar to fMRI BCIs and showed the directions for further improvement (Hoshi and Tamura 1997; Coyle et al. 2004; Coyle, Ward, and Markham 2007). However, it is widely considered, that the main potential of fNIRS in BCI design is associated with hybrid EEG-fNIRS signal acquisition. Both methods are non-invasive, relatively affordable, allow for portability and do not require a specialized shielded environment. A number of hybrid EEG-fNIRS BCI implementations have emerged in recent years reporting an improved performance compared to single-modality BCIs (Fazli et al. 2012; Khan, Hong, and Hong 2014; Buccino, Keles, and Omurtag 2016). These implementations employ separate data acquisition and preprocessing for each data modality, and combined feature extraction, selection and classification. The features from EEG and fNIRS signals are non-redundant to each other and provide complementary information boosting the classification accuracy or alternatively the number of BCI commands.

1.6 Conclusion.

This chapter provided a general introduction to brain-computer interfacing including the state of BCI research, common application

areas and fundamental aspects of BCI design such as general BCI architecture, available brain signal acquisition systems and various approaches for BCI control. Besides, in this chapter the motivation and objectives of this thesis were formulated. Essentially the motivation of this work is to improve the performance of existing control BCI systems by focusing on the increase in classification reliability that in practice was achieved by addressing the limitations of EEG spatial resolution through the application of source reconstruction technique. The following chapters of this manuscript will give an overview of the EEG signal processing tools applicable in control BCIs, introduce the reader to the area of EEG source reconstruction and show how the control BCI performance can benefit from the application of this technique.

Chapter 2

EEG BCI signal processing sequence.

This chapter gives an overview of the essential functional elements of BCIs. The following sections are dedicated to a theoretical background of the main stages of the BCI signal processing scheme and common approaches to BCI design.

2.1 Signal preprocessing.

Immediately after acquisition the EEG signal is extremely noisy, containing signals induced by external electrical devices as well as various bioelectrical artifacts, e.g., from eye movement, heart beat, and muscle contractions. The latter is especially problematic, since the amplitudes of muscular artifacts are generally a few orders of magnitude larger than the amplitudes of signal of interest. These effects, however, can be partially alleviated by certain signal preprocessing techniques which aim to increase the SNR without discarding the useful components.

In practice this is achieved by application of various spatio-temporal filtering methods. In the following sections we will describe the main signal preprocessing techniques used in BCI design.

2.1.1 Time-domain filters.

Time-domain filters such as band-pass or high-pass filters are typically used to limit the signal analysis to a particular frequency band. For example, in motor imagery BCIs the user's control intent typically modulates μ and β rhythms, therefore in such BCIs it is common

to limit the EEG to 8-30 Hz. In the majority of BCIs the low frequency components of the EEG (< 4 Hz) generally do not carry useful information about the user's intent, and contain the high-power noise from heart beat, breathing, muscular contractions (partially), slow signal drifting due to the electrode polarization and many other unwanted effects. Also, power line interference, which causes a 50 Hz spike in the signal spectrum, can be easily removed by band-pass or low-pass filtering. In fact, in terms of noise power cancellation band-pass filtering is the most effective processing tool.

Discrete Fourier Transform filters.

Discrete Fourier Transform (DFT) represents the sampled signal as a sum of oscillations at different frequencies. The amplitudes at each frequency are encoded by the DFT coefficients, and a full set of these coefficients is the signal representation in the *frequency domain*. The DFT is applied to a limited time series, hence windowing of the signal is necessary. The DFT $S(f)$ of a signal $s(n)$ of length N is found as:

$$S(f) = \sum_{n=0}^{N-1} s(n) e^{\frac{-2j\pi fn}{N}} \ . \tag{2.1}$$

After the signal is transformed into the frequency domain, the filtering is reduced to a simple cancellation of coefficients at the unwanted frequencies. Inverse Fourier Transform is reconstruction of the time series $s(n)$ from the DFT coefficients:

$$s(n) = \frac{1}{N} \sum_{f=0}^{N-1} S(f) e^{\frac{2j\pi fn}{N}} \ . \tag{2.2}$$

The DFT is applicable to real time signal processing, due to its popular and computationally cheap implementation known as the Fast Fourier Transform (FFT) (Cooley and Tukey 1965).

Finite Impulse Response filters.

Finite Impulse Response (FIR) filters process the signal based only on the previous P samples of time series $s(n)$. The filter characteristics

are defined through its coefficients a_k and the output $y(n)$ is found as:

$$y(n) = \sum_{k=0}^{P} a_k s(n - k) \ . \tag{2.3}$$

The filtering itself is typically implemented by convolving the filter impulse response, which is the set of coefficients a_k with the finite interval of the signal. FIR filters are used as a primary filtering method in BCI design and offline signal analysis, due to their high accuracy and stability. Compared with alternatives, the only major disadvantage of FIR filters is higher memory requirements, since an accurate magnitude characteristic in pass band is achieved by a larger number of coefficients (Oppenheim and Schafer 2010).

Infinite Impulse Response filters.

Unlike FIR, Infinite Impulse Response (IIR) filters are recursive, meaning that they generate the output $y(n)$ based on the previous P samples of discrete time series $s(n)$ and also on the previous Q filter outputs. Such filtering is described and implemented by:

$$y(n) = \sum_{k=0}^{P} a_k s(n - k) + \sum_{j=1}^{Q} b_j y(n - j) \ , \tag{2.4}$$

where a_k and b_j are the feedback and the feedforward filter coefficients that define the filter response. IIR filters require very few coefficients to maintain a high accuracy in the pass band. However, in context of the EEG signal they perform poorly in the presence of high-amplitude noise spikes. For example, during recording in our laboratory settings after the occurence of a single short muscular artifact the IIR filter output is often contaminated by high-power noise for 4-7 seconds. The IIR filter implementations most commonly used in BCIs are Butterworth, Chebyshev type II and elliptic filters (Ang et al. 2012; Arvaneh et al. 2011).
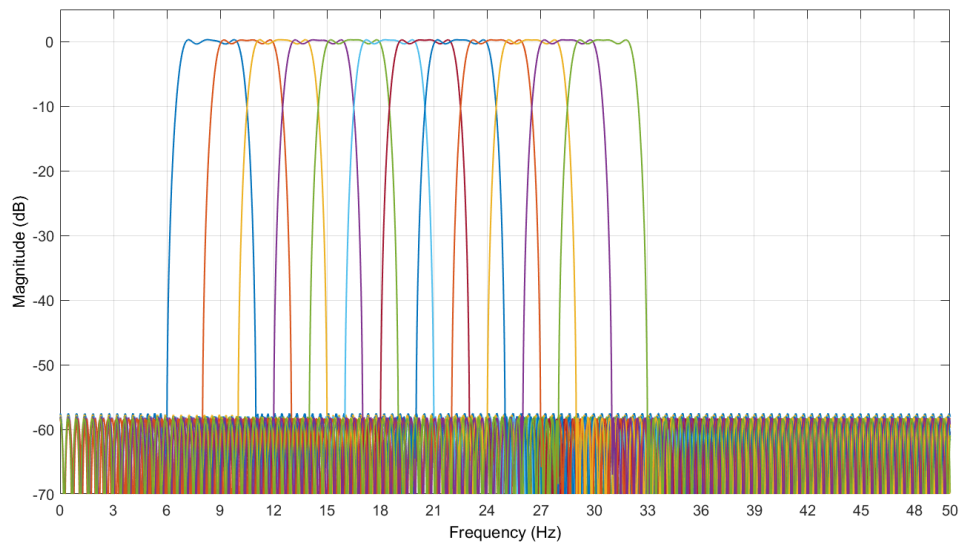
FIGURE 2.1: Magnitude characteristic of an FIR fil-
ter bank used to isolate signal components in μ and
β bands of EEG.

Subband decomposition using filter banks.

The EEG signal is known to contain multiple oscillatory processes
limited to different frequency bands, which reflect certain functional
processes of the brain including rest, cognition, perception, planning
and others. In many aspects of BCI design and EEG analysis in gen-
eral it is necessary to consider and characterize these processes sepa-
rately. Therefore, it is common to decompose the signal into multiple
components, each containing one of these functional rhythms. Typi-
cally this is achieved by the application of filter banks, which are in
essence a set of band-pass filters, each filtering the signal into a par-
ticular narrow band (Ang et al. 2012). An example of such filter bank
applicable to decomposition of μ and β bands of the EEG is shown
in figure 2.1.

2.1.2   Spatial filtering and re-referencing.

In context of the EEG, spatial filtering corresponds to various tech-
niques that enhance or isolate the signal of interest by using a com-
bination of signals from different channels.

In its simplest form spatial filtering corresponds to the selection
of a channel set and the discarding of others. For example, the SSVEP

response to rhythmic light flashing is known to originate in the occipital brain area, hence the BCIs based on this physiological principle typically use only a small set of electrodes at the back of the head, e.g., O1, Oz, O2 locations (Regan 1979; Volosyak, Cecotti, and Graser 2009; Wang, Esfahani, and Sundararajan 2012).

Common Average Reference.

The common average reference (CAR) filtering corresponds to the re-referencing of signal to the ground average of voltages at all electrodes after the signal acquisition. This operation is applied to each time sample of multichannel EEG $\mathbf{M}$ and the processed data matrix $\mathbf{M}_{CAR}$ is given by:

$$\mathbf{M}_{CAR} = \mathbf{M} - \overline{\mathbf{M}} = \mathbf{H}\mathbf{M} , \qquad (2.5)$$

with the centering matrix $\mathbf{H}$ given by:

$$\mathbf{H} = \mathbf{I} - \frac{1}{N}\mathbf{1}\mathbf{1}^{T} . \qquad (2.6)$$

Here $\mathbf{I}$ is the identity matrix, N is the number of electrodes and $\mathbf{1}$ is the column vector of ones of the size equal to the number of EEG channels. The sum of all CAR channels is zero at each time point and centering matrix corresponds to the identity matrix applied to the raw scalp potentials. Due to the properties of the centering matrix, the finite block of CAR data has at most rank $N - 1$, since one of its eigenvalues is zero (Malmivuo and Plonsey 1995).

In substance CAR provides EEG data that is nearly reference-free. Average reference accumulates electrical components that are present in a large portion of electrodes and, therefore, CAR performs as a high-pass spatial filter, accentuating components with highly focal spatial distribution (Nunez et al. 1994; McFarland et al. 1997). In the BCI-related literature it is widely speculated that the application of CAR spatial filtering improves the average SNR of data, which results in higher BCI performance (Alhaddad 2012; McFarland et al. 1997).

Surface Laplacian filter.

Similarly to the CAR re-referencing, Surface Laplacian (SL) is applied to re-reference the EEG channels to a new potential, in this case calculated within a local group of electrodes. At each time point the filtered signal at a single channel $\hat{M}_i$ is defined as follows:

$$\hat{M}_i = M_i - \frac{1}{4} \sum_{j=1}^{4} M_j \, , \tag{2.7}$$

where M_j represent the four nearest electrodes neighboring M_i. This operation corresponds to bidirectional edge detection in computational vision, reducing the blurriness of the spatial distribution of the measured fields and localizing peaks of scalp potentials. In the past years the application of SL filters has been shown to reduce the spatial noise and improve the classification accuracy of BCIs, especially in those that utilize a large number of electrodes (> 32) (Nunez et al. 1994; McFarland et al. 1997; McFarland 2015).

2.1.3 Blind Source Separation.

The EEG signal is a complex mixture of distributed brain neuronal activity, where the user's intent for BCI control, the signal of interest, comprises only a tiny portion of the overall energy. This assumption fits very well into the model of blind source separation (BSS), which represents the multidimensional signal as a limited set of simultaneous active sources. Various BSS algorithms can be utilized in EEG processing for de-noising, artifact removal or feature extraction. In the generative model of BSS the multichannel signal $\mathbf{M}$ is explained by a set of independent sources $\mathbf{S}$ through the following relationship:

$$\mathbf{M} = \mathbf{AS} + \boldsymbol{\epsilon} \, , \tag{2.8}$$

where $\mathbf{A}$ is the mixing matrix and $\boldsymbol{\epsilon}$ is the methods error ($\epsilon = 0$ in lossless case). The word 'blind' in BSS means that there is no prior knowledge about the mixing model of sources, hence $\mathbf{A}$ is typically estimated directly from the observed data under various assumptions about the sources, which define a particular BSS algorithm. In

other words BSS aims to define a new set of axes that are independent of one another in some way, and then use a certain measure of independence in order to decorrelate the data by maximizing this measure for the projections onto these axes. Thus, the sources in the BSS model are the aforementioned projections on the newly discovered axes.

After the mixing model has been estimated, de-noising is possible with the unmixing matrix $\mathbf{A}^{-1}$, which is some approximation of the inverse of $\mathbf{A}$. The actual noise cancellation is achieved by the discarding of the unwanted components, corresponding to the particular rows of $\mathbf{S}$ and columns of $\mathbf{A}$. In EEG analysis these components can be determined in semi-automatic manner (from visualizations) or automatically, e.g., through the application of some clustering algorithm.

The simplest of BSS methods used in EEG analysis and other various engineering fields is Principal Component Analysis (PCA), introduced in 1901 by Karl Pearson (Pearson 1901). The basic idea of PCA is to find a set of N component vectors $\mathbf{s}_1, \mathbf{s}_2, \mathbf{s}_3..\mathbf{s}_N$ (rows of $\mathbf{S}$), which explain the maximum amount of variance possible through N orthogonal projections. In PCA the criterion used to discover the set of axes is variance, and independence is achieved by requiring them to be orthogonal. In practice the computation of the demixing matrix is achieved simply through the eigenvalue decomposition of a sample covariance matrix $\mathbf{C} = \mathbf{M}^T\mathbf{M}$, with eigenvectors representing the columns of $\mathbf{A}$.

Independent Component Analysis.

Independent Component Analysis (ICA) is probably the most popular BSS method used in EEG exploratory analysis. ICA is a general name for a family of BSS algorithms, which seek to determine a set of statistically independent source signals from the available multichannel dataset. This fits into a generative model defined in equation 2.8. In practice, ICA is achieved by finding the minimum or maximum of a cost function representing the statistical independence of sources, based on measures such as entropy, mutual information or the fourth order moment, kurtosis.

The method of ICA, although not the name, was first described in (Ans, Hérault, and Jutten 1985; Hyvärinen, Karhunen, and Oja 2004). However, it became popular only in the middle of 1990s after the introduction of the infomax approach by (Bell and Sejnowski 1995). A number of other implementations with improved computational efficiency have appeared in the following years, which has contributed to the application of ICA to large-scale problems (Hyvärinen and Oja 1997; Bach and Jordan 2003; Miller and III 2003). Recently Akhtar *et al* have introduced the ICA approach called online recursive independent component analysis (ORICA) (Akhtar et al. 2012) with computational efficiency suitable for real-time BSS applications. A Matlab implementation of this algorithm is available in a recent toolbox named REST (Pion-Tonachini et al. 2015).

In the context of BCI design, ICA is mostly applied to suppress the ocular artifacts and for data de-noising in general (Jung et al. 2000; Gao et al. 2010). However, it has been found that such artifact removal may corrupt the power spectrum of the signal and, therefore, impede the classification (Wallstrom et al. 2004).

2.2   Feature extraction.

EEG acquisition and the follow-on preprocessing stages generally produce very high dimensional data. Considering that the number of electrodes in common EEG-BCI montages varies from 3 to 128, with sampling rates of 100-1000 Hz and BCI command durations of between 1 and 5 seconds, this yields hundreds of thousands of data points representing a single BCI command. However, the accurate classification of the control intent requires much more compact representation, which is achieved by the extraction of various physical signal properties encoding the current brain state and cancellation of components irrelevant to classification. Predictor variables, that hold these physical properties, are known as features and in practice, they are aggregated into vectors, each representing a limited time interval of EEG to be classified. Hence, the aim of feature extraction is to transform the EEG signal interval into a feature vector in a way that maximizes the classification performance.

In order to achieve high classification reliability, the BCI features must effectively encode the user's commands and should not contain, or at least minimize, noise that can hinder the classifier. The identification of such signal properties and numerical methods for their extraction has been the focus of BCI research since the first prototype implementations, leading to the creation of numerous approaches and algorithms (Boostani et al. 2007; Mason et al. 2007; Brunner et al. 2011). On the one hand, the extraction algorithm is highly dependent on the physics and neurophysiology of the processes underlying the user's control intent, and hence must be selected based on the type of mental task for BCI control. On the other hand, these key signal properties can be captured by a large number of numerical approaches. This results in a wide variety of BCI feature extraction methods, which generally operate in the time, frequency or spatial domains of signal or combinations of these. In the following sections the most popular methods for BCI feature extraction are introduced.

2.2.1 Temporal features.

Various indicative data properties can be found in the time-domain representation of a signal. Temporal features capture the time information about when a certain neurophysiological effect occurs, or a sequential configuration of such effects. Among the temporal features commonly used in BCIs we can list autoregressive coefficients, Hjorth parameters, nonlinear regressive coefficients and phase locking value.

Autoregressive parameters.

In the autoregressive (AR) model the one-dimensional discrete signal $m(n)$ is represented as a weighted linear combination of its previous p samples and a stochastic noise term ϵ, which is generally white noise:

$$m(n) = \sum_{i=1}^{p} a_i m(n-i) + \epsilon \, , \qquad (2.9)$$

where a_i are the AR parameters or coefficients, which compactly describe the sequence of amplitudes in a given time series. These coefficients were successfully used directly as features in several BCI implementations (Dornhege et al. 2004; Mason et al. 2007). Besides that, the AR parameters a_i can be used to describe the power spectrum of the EEG. For the normalized frequency ω, the AR spectrum $y(\omega)$ of time series $m(n)$ is estimated as follows:

$$y(\omega) = \frac{1}{|1 - \sum_{i=1}^{p} a_i e^{-ji\omega}|^2} \ . \tag{2.10}$$

The AR spectrum estimation is considered to be superior to the Fourier Transform in the sense that it is more accurate for short time intervals (Krusienski, McFarland, and Wolpaw 2006). The estimation of static AR coefficients is possible, for example, through Yule-Walker, Burg or forward-backward algorithms (Nicolas-Alonso and Gomez-Gil 2012). However, as predictors AR coefficients are known to perform poorly in case of recognition of non-stationary signals such as the EEG. In order to deal with this drawback the more complex and adaptive AR models were applied to BCI feature extraction, namely the multivariate adaptive AR model (MVAAR) and time varying AR model (TVAR) (Wang et al. 2010; Najeeb et al. 2016).

Hjorth parameters.

Hjorth parameters are time-domain metrics of a signal introduced by Bo Hjorth in 1970, which were originally developed for quantitative analysis of EEG signal (Hjorth 1970). By definition Hjorth parameters are represented by three metrics describing the signal $m(n)$, namely Activity, Mobility and Complexity:

$$Activity(m(n)) = \mathrm{var}(m(n)) \ ,$$

$$Mobility(m(n)) = \sqrt{\frac{Activity(\frac{d\,m(n)}{dn})}{Activity(m(n))}} \ , \tag{2.11}$$

$$Complexity(m(n)) = \frac{Mobility(\frac{d\,m(n)}{dn})}{Mobility(m(n))} \ ,$$

where var$(\cdot)$ denotes signal variance. In BCIs features based on these metrics are mainly applied to motor imagery classification (Obermaier et al. 2001a; Vidaurre et al. 2009; Oh, Lee, and Kim 2014).

Phase locking value.

Another time-domain metric of EEG signal that is increasingly being used in BCIs is the phase locking value (PLV), which describes the phase coupling between the pairs of electrodes. This metric and a numerical method for its calculation was first described by Jean-Philippe Lachaux et al. in (Lachaux et al. 1999). The perfect phase locking of a pair of continuous signals $m_x(t)$ and $m_y(t)$ with phases $\phi_x(t)$ and $\phi_y(t)$ means that:

$$\phi_x(t) - \phi_y(t) = \text{const} \tag{2.12}$$

The calculation of PLV is typically conducted in two stages: the first is estimation of instantaneous phases of a pair of signals, and at the second stage the degree of phase coupling is quantified using a statistical criteria. The instantaneous phase is obtained from the analytic signal $z(t)$, defined for $m(t)$ as:

$$z(t) = m(t) + j\hat{m}(t) = A(t)e^{j\phi(t)} \ , \tag{2.13}$$

where $\hat{m}(t)$ is the Hilbert transform of $m(t)$:

$$\hat{m}(t) = \frac{1}{\pi} \int_{-\infty}^{\infty} \frac{m(\tau)}{t - \tau} \mathrm{d}\tau \ . \tag{2.14}$$

The instantaneous phase of $m(t)$ is then found as follows:

$$\phi(t) = \arctan\left(\frac{\hat{m}(t)}{m(t)}\right). \tag{2.15}$$

The instantaneous phase is calculated for both signals in a given pair, and then the difference is obtained: $\Delta\phi(t) = \phi_x(t) - \phi_y(t)$. Finally, the instantaneous value of PLV is calculated as:

$$PLV = \left| \left\langle e^{j\Delta\phi(t)} \right\rangle_t \right| , \tag{2.16}$$

where $\langle \cdot \rangle$ denotes averaging over the given time window. In practice PLV is a continuous signal metric and averaging is conducted over the sliding window. In case of perfect synchrony $\Delta\phi(t) = const$, and hence $PLV = 1$.

For each averaged time-window the PLV metric provides a large number of features, since it is calculated for each pair of channels. For example, if a signal is recorded from 32 EEG electrodes, there are $\binom{32}{2} = 496$ combinations of channels and PLV values for each time-window. The performance of PLV-based feature extraction for BCIs, especially in the context of motor imagery classification, was described in a number of recent papers (Wang et al. 2006; Krusienski, McFarland, and Wolpaw 2012; Hwang, Im, and Park 2013; Yi et al. 2016).

Nonlinear regressive coefficients.

Similar to PLV, nonlinear regressive coefficients (NLR) provide a measure of inter-channel association, exploring nonlinear amplitude coupling between two signals.

For continuous signals NLR is defined as follows. Given signals $x(t)$ and $y(t)$, the conditional expectation $\mu_{y|x}$, also known as the regression curve of y on x, is defined as:

$$\mu_{y|x}(x) = \int_{-\infty}^{\infty} y(t)p(y|x)\mathrm{d}y \ , \tag{2.17}$$

where $p(y|x)$ is the conditional probability of $y(t)$ given $x(t)$. The NLR measure of amplitude coupling is then found as:

$$\eta_{y|x} = \frac{\mathrm{var}(y(t)) - E[(y(t) - \mu_{y|x}(x))^2]}{\mathrm{var}(y(t))} \ . \tag{2.18}$$

The term $E[(y(t) - \mu_{y|x}(x))^2]$, known as the explained variance, is obtained from the regression curve. The total variance minus the explained variance, which is the numerator of (2.18) describes the unexplained variance. The rationale behind the NLR metric is that the amplitude of signal $y(t)$ is represented as a function of the amplitude of $x(t)$. For a given value of $x(t)$ it is then possible to predict $y(t)$ at the same instant using the NLR curve (Wei et al. 2007).

In practice, the NLR estimate of two sampled signals $x(n)$ and $y(n)$ of length N is obtained as follows:

$$NLR = \frac{\sum_{n=1}^{N}(y_n - \langle y \rangle_N)^2 - \sum_{n=1}^{N}(y_n - \hat{\mu}_{y|x}(x))^2}{\sum_{n=1}^{N}(y_n - \langle y \rangle_N)^2} \, , \qquad (2.19)$$

where $\langle \cdot \rangle_N$ denotes the average over N time samples and $\hat{\mu}_{y|x}(x)$ is the piecewise approximation of the regression curve $\mu_{y|x}(x)$. The values of NLR coefficients vary from zero to one, with $NLR = 1$ showing the maximal degree of signal association. Feature extraction for BCIs based on such amplitude coupling measure was described and evaluated in (Wei et al. 2007; Liu, Zheng, and Zhang 2009; Krusienski, McFarland, and Wolpaw 2012).

2.2.2 Spectral features.

The EEG signal is known to be a summation of fields generated by complex oscillatory activity originating from the various parts of the brain. Therefore, representation of EEG in the frequency domain is a useful approach for capturing indicative spectral patterns. In the following sections various spectral feature extraction methods commonly used in BCIs are discussed, in particular band power, power spectral density, short-time Fourier transform, wavelets and time-frequency representations.

Band power features.

Band power features represent the average power of a signal in a particular frequency band. In practice they are calculated by band-pass filtering each channel, then squaring the samples and averaging over the chosen time window. It is also common to apply log-transform to the result, so that the features have a distribution close to normal, which is recommended for many classification algorithms. The filter passband is generally determined from the offline EEG analysis or is chosen with respect to the general physiological knowledge, for example μ- and β-bands of EEG. Despite the simplicity, this feature extraction method is successfully applied in many motor imagery

BCI implementations (Pfurtscheller and Neuper 2001; Boostani et al. 2007; Lotte et al. 2007b).

Short time Fourier transform.

In real-time asynchronous BCIs the FFT spectrum of a signal is typically estimated by the short time Fourier transform (STFT). In such a case the STFT refers to the signal buffering, usually with dense overlapping, application of a windowing function and the consequent FFT estimation for each tapered buffer and each EEG channel. Following the DFT definition in (2.1.1), the STFT $S(f)$ of time series $s(n)$ of length N and window function $w(n)$ is defined as:

$$S_{STFT}(f) = \sum_{n=0}^{N-1} s(n) w(n - mR) e^{\frac{-2j\pi f n}{N}} \; , \tag{2.20}$$

where m is the time lag variable and R is the hop size, in samples, between successive buffers. The simple rectangular sliding window produces 'spectral leakage', which is the occurrence of new frequency components due to the cutting of the signal by buffering. This effect is alleviated by the choice of a particular windowing function, such as Hanning, Blackman or Hamming windows, which typically represent some bell-shaped mask of a finite length that is used to suppress the signal at buffer borders (Alfred 1999). In BCIs the STFT is generally performed as part of the visualization or feature extraction based on power spectrum or time-frequency representation.

Power spectral density features.

Power spectral density (PSD) of a discrete signal describes the distribution of power over frequency. Feature extraction based on PSD is probably the most popular way to represent the signal for classification and is capable of providing discriminative properties of a wide range of BCI mental tasks (Boostani et al. 2007; Mason et al. 2007). The most straightforward method of PSD estimation is historically called *periodogram* and is achieved by squaring the magnitudes

of absolute values of STFT coefficients. Given the set of FFT coefficients $S(f)$ of discrete signal $s(n)$ of length N, the PSD estimate $P(f)$ at $N/2 + 1$ frequencies is found as:

$$P(0) = P(f_0) = \frac{1}{N^2}|S_0|^2$$

$$P(f_k) = \frac{1}{N^2}[|S_k|^2 + |S_{N-k}|^2] \,, \tag{2.21}$$

or in practice:

$$P(f_k) = \frac{2}{N^2}|S_k|^2 \,, \forall k \in [1, N/2 + 1]$$

The resulting vector of PSD values can be directly used as a feature vector at the classification stage. Despite being widely applied, this PSD estimation method suffers from low frequency resolution. Alternatively, the power spectrum can be obtained from the AR coefficients as described in (2.10) (Krusienski, McFarland, and Wolpaw 2006).

Time-frequency representation.

Time-frequency representation (TFR) of a discrete signal, also referred to as atomic decomposition, represents the continuous progression of signal power spectrum, in other words, the dynamics of power distribution over frequency. The TFR representation is a powerful tool for exploratory analysis of EEG and also a hybrid feature extraction approach, capable of capturing indicative properties of data in both time and frequency domains. In the simplest case the TFR estimation is performed using multiple STFTs in a sliding window over the given interval of the signal. Following the previous definitions, the power spectrum $P(f, m)$ of time series $s(n)$ of length N at time window m is obtained from the STFT with windowing function $w(n)$ as:

$$P(f, m) = \frac{2}{N^2}\left|\sum_{n=0}^{N-1} s(n)w(n - mR)e^{\frac{-2j\pi fn}{N}}\right|^2 \tag{2.22}$$
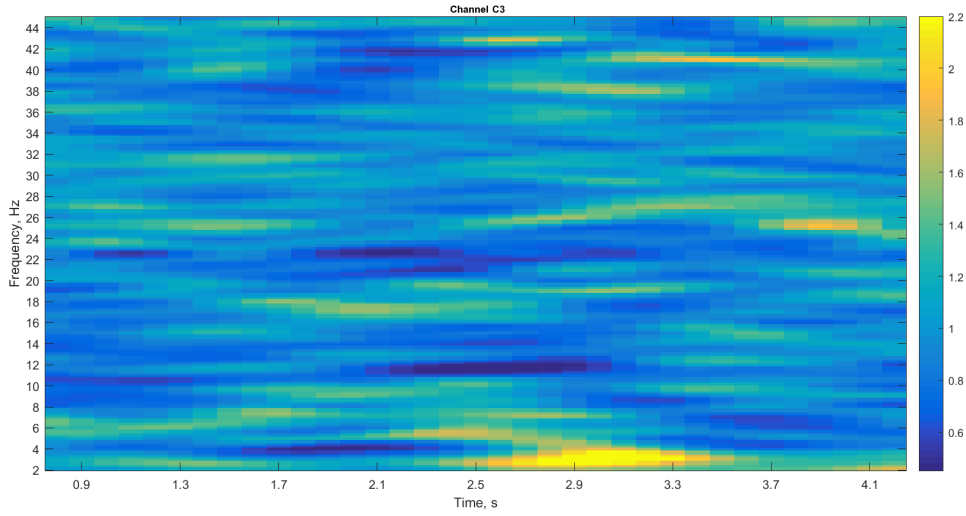
FIGURE 2.2: Example of averaged TFR of a single EEG channel during right hand motor imagery calculated using 1 second Hamming windows and 4 Hz smoothing. This image was obtained by averaging multiple right hand TFRs and contrasting them against TFRs of resting state.

It follows from the definition of a DFT that the frequency resolution of STFT-TFR is constant for all frequencies and is defined by the chosen length of the time window. Example of TFR representation of motor imagery showing the ERD effects in mu and beta bands is given in figure 2.2.

Wavelet features.

A wavelet transform is an alternative method for time-frequency representation of a signal with capabilities for flexible time-frequency resolution (figure 2.3). In a DFT the signal is represented as a sum of variously scaled periodic basis functions with the frequency resolution being fixed and defined by the length of the time window. Similarly, the discrete wavelet transform (DWT) decomposes the signal into a sum of its own flexible basis functions called wavelets. The limited set of wavelets $\Phi_{a,b}(n)$ is derived from the initial (mother) wavelet $\phi(n)$ through scaling by the dyadic dilation factor $a = 2^q$ and time-shifting by $b = k\, 2^q$:

$$\Phi_{a,b}(n) = \frac{1}{\sqrt{a}}\phi(\frac{n-b}{a}) = \frac{1}{\sqrt{2^q}}\phi(2^{-q}n - k) \qquad (2.23)$$
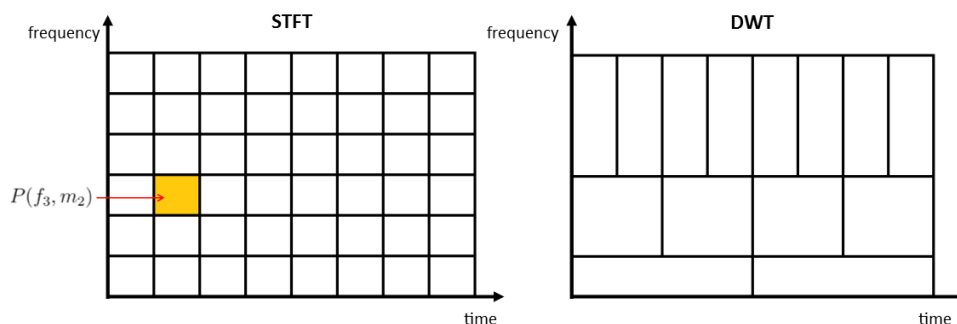
FIGURE 2.3: The comparison of time-frequency representation (TFR) methods based on STFT and DWT. Wavelet transform provides for the flexibility in time-frequency resolution.

For integer values of q and k and the shape of the mother wavelet $\phi(n)$ defined by the analytical expression (Daubechies 1990). The DWT of a sampled signal $s(n)$ of length $N = 2^p, p \in \mathbb{Z}$ is then defined as follows:

$$W a, b(s) = \sum_{n=0}^{N-1} \Phi_{a,b}(n)s(n) \tag{2.24}$$

The main advantage of the DWT is that it allows for the analysis of a signal on multiple scales simultaneously, due to the dilation and shifting of the basis functions. In such a case the frequency resolution is defined by the wavelet's scale. As a result, with DWT it is possible to analyze the high-frequency components, where the EEG features are known to be spread more over the spectrum, with a finer temporal resolution and at the same time represent the low-frequency parts of the signal, where the spectral distribution of features is denser, with a higher frequency resolution. Feature extraction based on wavelet decomposition has been applied in many BCI implementations, yielding very promising results in classification of various cognitive tasks and especially imagination of movement (Ting et al. 2008; Hsu and Sun 2009; Robinson et al. 2013; Rosas-Cholula et al. 2010).

2.2.3   Spatial features.

The typical EEG electrode montage uniformly spans the scalp surface, because many types of neurophysiological effects are characterized by the voltage spatial distribution over the sensors. In particular, various mental tasks used as control signals in BCIs, can be identified by the location of signal of interest, i.e., the distribution of temporal and spectral features over the EEG channels. For example, cortical regions, corresponding to different muscles involved in imagination of movement, are anatomically segregated, so the spatial distribution of power during the task execution is indicative of the brain state.

Spatial feature extraction is a hybrid approach, which aims to accentuate the information about where the relevant signal comes from, or focus on the signal originating from a particular brain area. In practice, this amounts to the numerical representation of distribution of temporal and frequency features over channels, or, alternatively, data-driven spatial filtering and subsequent temporal or spectral feature extraction. In the following sections the most common approaches for BCI spatial feature extraction are introduced, namely asymmetry features, common spatial patterns (CSP) and feature extraction based on source reconstruction.

Asymmetry features.

The functional brain areas activated during certain mental tasks are often anatomically segregated. If the degree of spatial separation is sufficient, the signal pattern can be characterized by the asymmetry features, which accentuate the left/right or frontal/posterior asymmetry of some metric of the signal, generally power.

In order to calculate the asymmetry features it is first necessary to define the pairs of opposite channels (see Figure. 1.7), for example, F5-F6, C3-C4, P7-P8 for left/right hemisphere asymmetry or FC3-CP3, FZ-OZ, F4-P4 for frontal/posterior asymmetry. The features are then calculated by contrasting the power in these channel pairs. In the literature it is possible to find three main approaches to such contrasting - differential asymmetry (DASM), rational asymmetry (RASM) and rational normalized asymmetry (RNASM). For a

single i-th channel pair with powers $P_{left,i}$ and $P_{right,i}$ the left/right asymmetry metrics are found as follows:

$$
\begin{aligned}
DASM_i &= P_{left,i} - P_{right,i} \\
RASM_i &= \frac{P_{left,i}}{P_{right,i}} \\
RNASM_i &= \frac{P_{left,i} - P_{right,i}}{P_{left,i} + P_{right,i}} \; .
\end{aligned}
\tag{2.25}
$$

The same applies to frontal/posterior asymmetry calculation. This feature extraction method has been shown to be particularly suitable for the identification of a subject's emotional state (Wheeler, Davidson, and Tomarken 1993; Coan and Allen 2004; Sulaiman et al. 2010; Wang, Nie, and Lu 2014). In addition to the monitoring applications, asymmetry has also been applied to the classification of a variety of BCI mental tasks, such as geometrical figure rotation, mathematical multiplication, visual counting, etc (Palaniappan 2006).

Common spatial patterns.

As mentioned previously, the extraction of spatial signal characteristics is possible through spatial filtering and subsequent temporal or frequency feature extraction. The common spatial patterns (CSP) algorithm is a method for data-driven spatial filter generation, which contrasts the data of different classes (mental tasks) in terms of variance distribution across channels. CSP feature extraction is a key method for motor imagery representation as it is capable of extracting ERD/ERS effects associated with this type of mental tasks, and hence provides for high classifier reliability (Blankertz et al. 2008; Grosse-Wentrup and Buss 2008; Ang et al. 2012).

The original CSP algorithm defined for two-class classification problem was first introduced in (Koles, Lazar, and Zhou 1990) and applied to the detection of EEG abnormalities. CSP aims to find a set of linear spatial filters $\mathbf{W}_{csp}$, the rows of which, $\hat{\mathbf{w}}_{csp}$, are found by solving the following optimization problem:

$$
\hat{\mathbf{w}}_{csp} = \underset{\mathbf{w}_{csp}}{\operatorname{argmax}} \; \frac{\mathbf{w}_{csp}\mathbf{C}_{class1}\mathbf{w}_{csp}^{T}}{\mathbf{w}_{csp}\mathbf{C}_{class2}\mathbf{w}_{csp}^{T}} \; ,
\tag{2.26}
$$

where $\mathbf{C}_{class1/2}$ denote the class-average covariances, obtained by averaging the normalized sample covariance matrices of Q EEG trials of a particular class:

$$\mathbf{C}_{class\_i} = \frac{1}{Q} \sum_{q=1}^{Q} \mathbf{C}_q \tag{2.27}$$

$$\mathbf{C}_q = \frac{\mathbf{M}_q \mathbf{M}_q^T}{\mathrm{trace}(\mathbf{M}_q \mathbf{M}_q)^T} \ ,$$

where Q is the number of EEG trials of class i, $\mathbf{M}_q$ represents the EEG data matrix of q-th trial and $\mathrm{trace}(\cdot)$ operator denotes the sum of diagonal elements of a matrix.

In other words, from equation (2.27) it follows that CSP finds a set of spatial weights, which attempt to maximize the signal variance of one class and simultaneously minimize the variance of another.

By the amended definition from (Ramoser, Müller-Gerking, and Pfurtscheller 2000) the calculation of CSP is done by simultaneous diagonalization of class-average covariances $\mathbf{C}_{class\_1}$ and $\mathbf{C}_{class\_2}$. The composite covariance $\mathbf{C}_c = \mathbf{C}_{class\_1} + \mathbf{C}_{class\_1}$ is factored by the eigenvalue decomposition into a matrix of eigenvectors $\mathbf{V}_c$ and a diagonal matrix of eigenvalues λ_c as:

$$\mathbf{C}_c = \mathbf{V}_c \lambda_c \mathbf{V}_c^T \ . \tag{2.28}$$

The whitening transform

$$\mathbf{P} = \lambda_c^{-\frac{1}{2}} \mathbf{V}_c^T \tag{2.29}$$

normalizes the composite covariance, so that $\mathbf{P}\mathbf{C}_c\mathbf{P}^T = \mathbf{I}$. When whitening $\mathbf{P}$ is applied to $\mathbf{C}_{class\_1}$ and $\mathbf{C}_{class\_2}$, it yields

$$\mathbf{C}'_{class\_1} = \mathbf{P}\mathbf{C}_{class\_1}\mathbf{P}^T \ , \ \ \mathbf{C}'_{class\_2} = \mathbf{P}\mathbf{C}_{class\_2}\mathbf{P}^T \ , \tag{2.30}$$

where matrices $\mathbf{C}'_{class\_1}$ and $\mathbf{C}'_{class\_2}$ share the common eigenvectors and the sum of their corresponding eigenvalues is always one, which

can be written as:

$$\mathbf{C}'_{class\_1} = \mathbf{B}\mathbf{\Lambda}_1\mathbf{B}^T \ , \ \ \mathbf{C}'_{class\_2} = \mathbf{B}\mathbf{\Lambda}_2\mathbf{B}^T \ , \ \mathbf{\Lambda}_1 + \mathbf{\Lambda}_2 = \mathbf{I} \ , \quad (2.31)$$

where $\mathbf{B}$ and $\mathbf{\Lambda}$ denote respectively the matrix of eigenvectors and the corresponding matrix of eigenvalues sorted in descending order. As denoted in (2.31) the sum of two corresponding eigenvalues is always one, which means that the eigenvector with the largest eigenvalue of $\mathbf{C}'_{class\_1}$ has the smallest eigenvalue of $\mathbf{C}'_{class\_2}$ and vice versa. Due to this effect, the projection of whitened EEG onto the first and last row of $\mathbf{B}$ corresponds to the maximization of ratio in equation (2.26). The full CSP projection matrix can be found as:

$$\mathbf{W}_{csp} = \mathbf{B}^T\mathbf{P} \ . \quad (2.32)$$

Since only the largest and smallest eigenvectors correspond to the desirable spatial filters that maximize (2.26), it is common to select a subset $\hat{\mathbf{W}}_{csp}$ formed by a small number u of the first and last rows of $\mathbf{W}_{csp}$ so that $2u$ spatial filters are taken from the full set.

The projection $\mathbf{Z}$ of EEG data segment $\mathbf{M}$ is then obtained as follows:

$$\mathbf{Z} = \mathbf{W}_{csp}\mathbf{M} \quad (2.33)$$

The columns of $\mathbf{W}_{csp}^{-1}$ represent the common spatial patterns, which are the spatial distributions of signal components found in the rows of $\mathbf{Z}$. The CSP features f_i are calculated for each i-th row of $\mathbf{Z}$ as the logarithm of normalized variance:

$$f_i = \log\left(\frac{\text{var}(\mathbf{Z}_i)}{\sum_{k=1}^{2u}\text{var}(\mathbf{Z}_k)}\right)$$
$$\mathbf{f} = [f_1, f_2 \ .. \ f_{2u}] \ , \quad (2.34)$$

where $\mathbf{f}$ is a feature vector of size $2u$ representing a single EEG trial $\mathbf{M}$, and $\mathbf{Z}_i$ here denotes the i-th row of $\mathbf{Z}$. The principle of CSP feature extraction and its performance for motor imagery representation is discussed further in chapters 5 and 6.

2.3 Feature selection.

The high dimensionality of feature vectors is an issue common to many BCI feature extraction methods. Generally multiple features are extracted from each EEG channel and also from multiple time segments to represent a single EEG trial to be classified. Besides that, in practical BCI applications the size of the training dataset (number of signal observations) is typically limited, since the EEG acquisition is time consuming and only subject-individual data can be used for training. The size of the training sample is tightly interconnected with the dimensionality of feature vectors. The effect known as "curse of dimensionality" describes this connection. It arises from the fact that the amount of data required for accurate class description grows exponentially with the number of predictor variables. Due to that, in practice it is recommended to use feature vectors of size 5-10 times smaller than the available number of observations (Bishop 2006).

In machine learning feature selection refers to the selection of a subset of features from the original set. Generally in the selection process features are ranked individually according to some metric such as variance over observations, one-dimensional divergence or distance between class means. Within the simplest approach the vector of desirable size is then selected from the highest ranked features. Although treating features individually has the advantage of computational simplicity, a combination of highest ranked predictors does not necessarily yield the best classification performance, since features can have high mutual correlation, i.e., carry redundant information. Therefore, a more comprehensive approach to feature selection consists of finding an optimal subset based on individual ranking of predictor variables as well as on their mutual dependencies and classifier output. In practice there is a variety of search techniques that can take into account the aforementioned aspects, e.g., sequential forward/backward selection, floating search methods or branch and bound methods (Theodoridis and Koutroumbas 2006; Bishop 2006). Matlab implementations for a large variety of feature selection algorithms are presented in FSLib (Roffo 2016) and FEAST toolboxes (Pocock and Brown 2016; Brown et al. 2012).

2.4 Classification.

The final key step in BCI signal processing is classification, which stands for the interpretation of a user intentions based on a feature vector that characterizes the brain activity within the current time window. This can be done either by regression or classification algorithms, although in the context of EEG BCIs the use of classification techniques is by far the most popular approach (Mason et al. 2007; Nicolas-Alonso and Gomez-Gil 2012). Hence, this section is dedicated to the overview of the most commonly used classification algorithms.

In machine learning terminology the supervised classifier is a mathematical model that is estimated from the available data samples from different classes, e.g. in the context of BCI, feature vectors from EEG during left and right hand motor imagery. In essence a trained classifier represents the decision boundary, which separates the clusters of feature vectors belonging to the various mental tasks being discriminated (see figure 2.4). Subsequently such a decision boundary can be used to predict the unknown data, i.e., allocate the
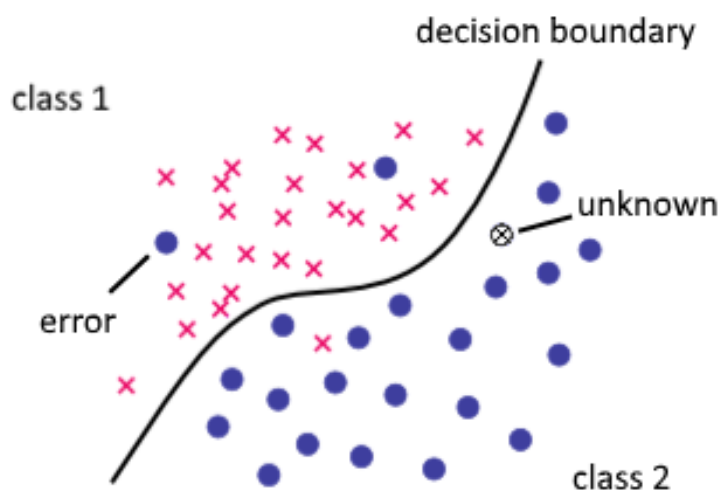
FIGURE 2.4: Principle of a supervised classifier. Here red crosses and blue dots denote the feature vectors belonging to different classes. At the classifier training the decision boundary is created based on the observations with known class labels. This decision boundary can then be used to predict the unknown data, i.e., allocate it to one of the classes (in this case - class 2).

unlabeled feature vector to a particular class, and hence infer the user's intent.

In the past 60 years hundreds of classification algorithms were proposed for a wide variety of applications such as speech and image recognition, search engines, natural language processing and interpretation, medical diagnosis and many others. A number of recent review papers highlight the most successful and popular classification methods relevant to BCI design (Mason et al. 2007; Bashashati et al. 2007; Lotte et al. 2007a; Khorshidtalab and Salami 2011; Nicolas-Alonso and Gomez-Gil 2012; Bashashati et al. 2015). In the following sections a brief survey of the most common EEG BCI classification approaches is presented.

2.4.1   Linear classifiers.

Linear classifiers combine a family of supervised learning methods that utilize only linear functions to discriminate between types of data. According to (Mason et al. 2007; Lotte et al. 2007a; Nicolas-Alonso and Gomez-Gil 2012) linear classifiers are the most popular algorithms in BCI research. .Amongst them linear discriminant analysis (LDA) and support vector machines (SVM) are the most mentioned methods.

Linear discriminant analysis.

Linear discriminant analysis (LDA), originally known as Fisher's linear discriminant analysis (FLDA), is the first formalized pattern recognition algorithm, introduced in (Fisher 1936). LDA is a simple classification method that provides for relatively accurate class discrimination without high computational requirements. Due to that, LDA is a very common choice for highly responsive control BCI systems with limited computational resource. This approach and its variations have been successfully applied to the discrimination of various neurophysiological effects, such as motor imagery (Pfurtscheller and Silva 1999; Ang et al. 2012), P300 effect (Krusienski et al. 2006; Hoffmann et al. 2008; Blankertz et al. 2011) and SSVEP response (Cecotti 2010; Ortner et al. 2010).
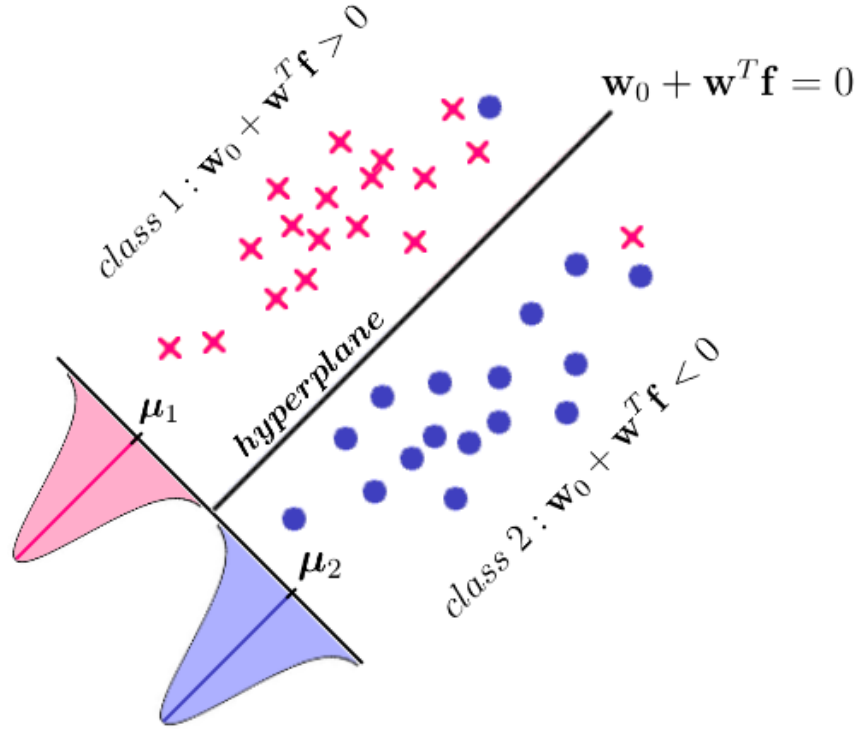
FIGURE 2.5: Two-dimensional case of LDA hyperplane separating two classes of data. Defined in a way to maximize the distance between class-means and minimize the variance within classes.

LDA is based upon the concept of finding a linear projection for features that maximizes the class separability. This method assumes a normal distribution of features and also equal feature covariances for classes being discriminated, which imposes additional requirements for feature preprocessing, more specifically, feature normalization or whitening. With LDA model parameters $\mathbf{w}$ and feature vector $\mathbf{f}$ of length d the projection $\mathbf{Z}$ is defined as:

$$\mathbf{Z} = \mathbf{w}^T\mathbf{f} = w_1f_1 + w_2f_2 + \cdots + w_df_d \tag{2.35}$$

The original Fisher's criterion for optimal separation is described by the following score function (Fisher 1936):

$$J(\mathbf{w}) = \frac{(\mathbf{w}^T\boldsymbol{\mu}_1 - \mathbf{w}^T\boldsymbol{\mu}_2)^2}{\mathbf{w}^T\mathbf{C}_c\mathbf{w}} = \frac{(\overline{\mathbf{Z}}_1 - \overline{\mathbf{Z}}_2)^2}{\mathbf{w}^T\mathbf{C}_c\mathbf{w}} , \tag{2.36}$$

where $\mathbf{C}_c = \mathbf{C}_{class1} + \mathbf{C}_{class2}$ is the composite covariance and $\overline{\mathbf{Z}}_{1/2}$ are

the projections of class means. Consequently, the maximum separation according to Fisher's criterion is achieved with the LDA parameters found as:

$$\mathbf{w} = \mathbf{C}_c^{-1}(\boldsymbol{\mu}_1 - \boldsymbol{\mu}_2)^2 \tag{2.37}$$

In other words from (2.36) it can be seen that LDA aims to find such a projection of training dataset, so that the resulting class means are as far apart as possible, whilst minimizing the feature variance within classes as shown in figure 2.5.

The estimates of mean and variance are prone to outliers, giving rise to one of the LDA's main drawbacks, poor performance in the presence of artifacts and strong noise. This disadvantage is addressed in LDA's extension known as regularized Fisher's linear discriminant analysis (RFLDA). This method introduces an additional regularization parameter that penalizes classification errors on the training set, and thus provides for better generalization capabilities with noisy data (Müller et al. 2004; Blankertz et al. 2011).

Besides that, the LDA method is capable of multiclass discrimination, that is classification into $N > 2$ classes. In practice this is achieved by one-vs-rest (OVR) training, which is estimation of N linear hyperplanes, each fitted to discriminate a particular class against all others.

Support Vector Machines.

Support vector machines (SVM) is a popular classification algorithm, that was first presented in (Boser, Guyon, and Vapnik 1992). Similarly to LDA, SVM uses a hyperplane to discriminate between data types. However, the SVM decision boundary is estimated in a way so that it maximizes the margins, i.e., the distance between features of classes being contrasted. Thus, such an optimal SVM hyperplane, or *maximum-margin* hyperplane, is set to be in the middle of two auxiliary hyperplanes passing through a set of feature vectors, called *support vectors* as shown in figure 2.6).

The original SVM algorithm is defined for two class discrimination problems. For a training set of Q observations $\mathbf{F} = [\mathbf{f}_1, \mathbf{f}_2, \ldots, \mathbf{f}_Q]$ and a set of corresponding class labels $\mathbf{y} = [y_1, y_2, \ldots, y_Q]$ that can
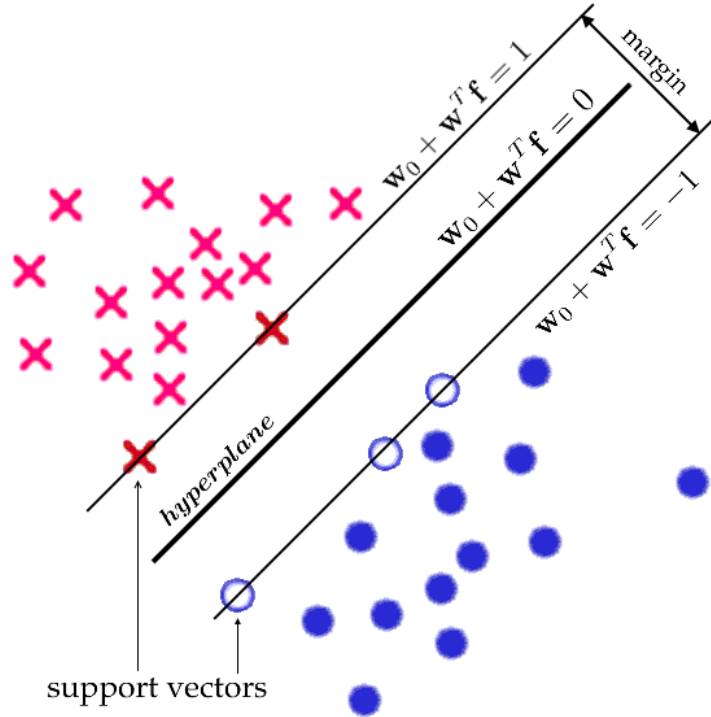
FIGURE 2.6: Two-dimensional case of SVM hyper-plane separating two classes of data. Defined in a way to maximize the margin between support hyper-planes.

only take values of 1 or -1, the margin hyperplanes can be defined by the equations:

$$\mathbf{w}_0 + \mathbf{w}^T \mathbf{f}_i = 1 \tag{2.38}$$
$$\mathbf{w}_0 + \mathbf{w}^T \mathbf{f}_i = -1 \, ,$$

where $\mathbf{w}$ are the SVM model parameters. Geometrically the distance between hyperplanes is $\frac{2}{||\mathbf{w}||_2}$ with $|| \cdot ||_2$ denoting the euclidean norm (l-2 norm). Consequently, maximization of the SVM margin is represented by the minimization of $||\mathbf{w}||_2$. In *hard-margin* SVM the data points $\mathbf{f}_i$ must lie on the correct side of the margin. This is expressed by the following constraints:

$$\mathbf{w}_0 + \mathbf{w}^T \mathbf{f}_i \geq 1 \, | y_i = 1 \tag{2.39}$$
$$\mathbf{w}_0 + \mathbf{w}^T \mathbf{f}_i \leq -1 \, | y_i = -1 \, ,$$

which can be combined into:

$$y_i(\mathbf{w}_0 + \mathbf{w}^T\mathbf{f}_i) \geq 1 \,, \forall i \in [1, Q] \tag{2.40}$$

Summing up the aforementioned considerations, the estimation of SVM model parameters can be expressed by the following optimization problem:

$$\text{minimize} \quad ||\mathbf{w}||_2 \tag{2.41}$$
$$\text{subject to} \quad y_i(\mathbf{w}_0 + \mathbf{w}^T\mathbf{f}_i) \geq 1 \,, \ \forall i \in [1, Q] \,.$$

This is a quadratic optimization problem subject to linear constraints and there exists a unique solution to it. However, if classes in the training set are not linearly separable, with outliers falling to the wrong side of the decision boundary, the strict constraints of hard-margin SVM lead to a suboptimal decision hyperplane. The outliers can be taken into account in *soft-margin* SVM, which introduces a *slack* variable $\xi_i \in [0, 1]$ that represents the degree of margin violation for each training sample, i.e., the distance from the correct side of hyperplane. The SVM optimization problem is then reformulated as:

$$\text{minimize} \quad ||\mathbf{w}||_2 + \lambda \sum_{i=1}^{Q} \xi_i \tag{2.42}$$
$$\text{subject to} \quad y_i(\mathbf{w}_0 + \mathbf{w}^T\mathbf{f}_i) \geq 1 - \xi_i \,, \ \forall i \in [1, Q] \,,$$

where λ is the regularization parameter with $\lambda = \infty$ corresponding to hard-margin SVM. The large margin of SVM reduces the chance of misclassification with noisy and artifact-contaminated data, therefore SVM is a common choice for classification in a large variety of BCIs (Lotte et al. 2007a; Li et al. 2010; Sun et al. 2010; Vallabhaneni and He 2013).

2.4.2   Nonlinear classifiers.

Nonlinear classifiers refer to a variety of classification methods capable of fitting a nonlinear decision boundary to the training set, e.g., as

shown in figure 2.4. In the context of BCI applications this family of algorithms is mainly represented by nonlinear SVM, artificial neural networks (ANN) and hidden Markov models (HMM).

Kernel SVM.

In (Boser, Guyon, and Vapnik 1992) the authors have described an extension to linear SVM, a so called "kernel trick" that maps the vectors $\mathbf{f}$ from the original training set into a feature space of higher dimensionality $\phi(\mathbf{f})$, where data can be linearly separable. A kernel $K(\mathbf{f}_i, \mathbf{f}_j)$ is a function of two vectors $\mathbf{f}_i$ and $\mathbf{f}_j$ that returns the value of the inner product of their images $\phi(\mathbf{f}_i)$ and $\phi(\mathbf{f}_j)$:

$$K(\mathbf{f}_i, \mathbf{f}_j) = \phi(\mathbf{f}_i)^T \phi(\mathbf{f}_j) \ . \tag{2.43}$$

Since only the inner product is returned, the dimensionality of the new space is not relevant. In practice, the kernel SVM is implemented by substituting the inner products $\mathbf{w}^T\mathbf{f}$ by kernel functions of a particular choice. An example of a kernel most commonly used in BCIs is the radial basis function (RBF) or Gaussian kernel (Lotte et al. 2007a):

$$K(\mathbf{x}, \mathbf{y}) = e^{-\gamma\|\mathbf{x}-\mathbf{y}\|_2} \ , \gamma > 0 \ . \tag{2.44}$$

Gaussian kernel SVM, or RBF SVM have shown a very good classification performance in a number of BCI applications (Kaper et al. 2004; Schlögl et al. 2005; Hortal et al. 2013). Similarly to LDA, the kernel and linear SVM can be extended to multiclass problems by using multiple OVR classifiers.

Hidden Markov models.

Hidden Markov model (HMM) represents a method for representing probability distributions over sequences of observations. HMMs are most commonly applied in the area of speech recognition, where the known classes (words) are inferred from the observed sequences of cepstral features (sounds). This approach fits perfectly to the EEG classification problem. Similar to human speech, the EEG physical

effects during BCI control intent have specific time courses that can be used to identify the mental state.

In HMMs the observed data $\mathbf{f}_i$, that is the feature vector sequence, is independent of previous observations $\mathbf{f}_{i-1}$ and is assumed to be the output of a hidden process, represented by a sequence of Markov chain states y_i. In terms of machine learning different class labels are encoded by certain sequences of states y. Taking into account the Markov property, the value of the observed $\mathbf{f}_i$ depends only on the concurrent state y_i, while the value of y_i is defined solely by the previous state that is y_{i-1}. Summing up these considerations, the joint probability distribution of a sequence of T states and feature vectors can be expressed in the following way:

$$P(y_{1:T}, \mathbf{f}_{1:T}) = P(y_1)P(\mathbf{f}_1|y_1) \prod_{i=2}^{T} P(y_i|y_{i-1})P(\mathbf{f}_i|y_i) \ . \qquad (2.45)$$

The HMM training corresponds to the estimation of conditional probabilities $P(y_i|y_{i-1})$ and $P(\mathbf{f}_i|y_i)$ for all sequences encoding the classes being discriminated. At the classification stage HMM selects the class that maximizes the probability of a corresponding state sequence y given the input sequence of $\mathbf{f}$. This dynamic approach has been successfully applied to the classification of time series of BCI features, yielding promising results with various types of control commands (Obermaier et al. 2001b; Cincotti et al. 2003; Mason et al. 2007; Argunsah and Cetin 2010; Lederman and Tabrikian 2012).

Artificial neural networks.

Artificial neural networks (ANNs) represent a family of nonlinear classifiers that are inspired by how the human brain processes information. ANNs are very flexible in the sense that they can fit a decision boundary of any complexity, and also have embedded capabilities for multiclass discrimination. The idea of an ANN is to mimic the brain's parallel computation, performed by layers of identical nodes (analogy for neurons) interconnected by links of different strengths (analogy for synaptic connections) as shown in figure (2.7).

The key advantage of ANN classifiers is the training mechanism, most commonly the backpropagation algorithm, which iteratively updates the nodes of NN and their connections. First, the NN is shown the training observations and the output is observed. If the output is incorrect, then the internal connection weights are iteratively updated within the optimization problem aiming to minimize the loss function with respect to weight values. Upon reaching the minimum of the loss function the ANN is in steady-state, i.e., ANN is trained to generalize on unlabeled data.

From a mathematical perspective, ANNs represent a mapping of input vector $\mathbf{f}$ to output class labels vector $\mathbf{y}$, where $\mathbf{f}$ and $\mathbf{y}$ can be of any length. The transform $\mathbf{y} = NN(\mathbf{f})$ denotes a series of layer-to-layer transforms, performed by identical nodes. Each node or neuron takes the whole output of the preceding layer, weighted by individual link strengths, and implements a nonlinear function with output bound between 0 and 1, most commonly a sigmoid function. Layer-to-layer connection weights are the ANN model parameters being estimated in the training process.

Multilayer perceptron (MLP) is the most common type of ANN classifiers used in a variety of BCI applications (R Millan et al. 2002; Nakayama and Inagaki 2006; Coyle, McGinnity, and Prasad 2010).
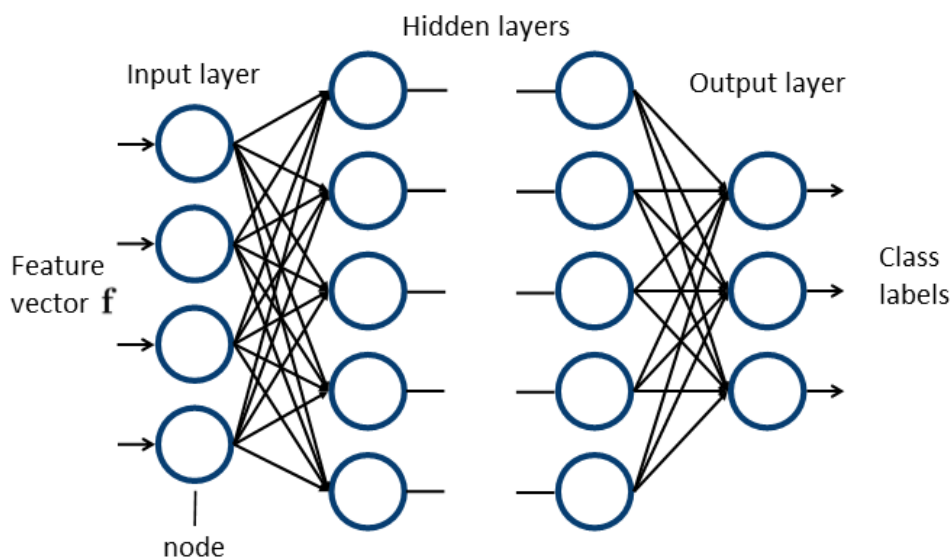
FIGURE 2.7: An example of the multilayer perceptron (MLP) architecture.

MLP represents a simple feedforward ANN architecture (without feedback loops) comprised of multiple hidden layers, as shown in figure 2.7. Other more complex ANN architectures are also used in BCIs, for example probability estimating guarded neural classifier (PeGNC) (Felzer and Freisieben 2003), fuzzy ARTMAP Neural Networks (Palaniappan et al. 2002), finite impulse response neural networks (FIRNN) (Haselsteiner and Pfurtscheller 2000).

Deep Learning

In general the variety of classification methods described above map the input features to the discrete output, i.e., known classes of data. The performance of these machine learning algorithms heavily depends on the type of features used to represent the raw data. Conventionally feature extraction methods are constructed manually with respect to the *domain knowledge* (background knowledge about the observed data). Considering the variety of methods for data representation, described for example in section 2.2 of this thesis, the search for optimal feature extraction for a specific BCI application is a complex task, which remains in the focus of current BCI research.

A possible solution to this problem is to utilize machine learning to find not only the mapping from representation to data class output, but also the optimal type of representation itself. This approach is referred to as *representation learning* and is a part of the trending deep learning paradigm (LeCun, Bengio, and Hinton 2015).

Deep learning stands for a family of machine learning algorithms that rely on a multilayer structure of identical non-linear processing units to implement both - feature extraction and output mapping (classification) (Goodfellow, Bengio, and Courville 2016). These series of hidden layers extract increasingly abstract features from the input data. This allows to represent the complex real-world data as a nested hierarchy of concepts, each defined in terms of simpler ones. Figure 2.8 illustrates this idea by visualising features from different hidden layers of the deep neural network trained to locate car wheels on images (figure was prepared using Caffe (Jia et al. 2014) and Deep Visualization Toolbox (Yosinski et al. 2015) software).
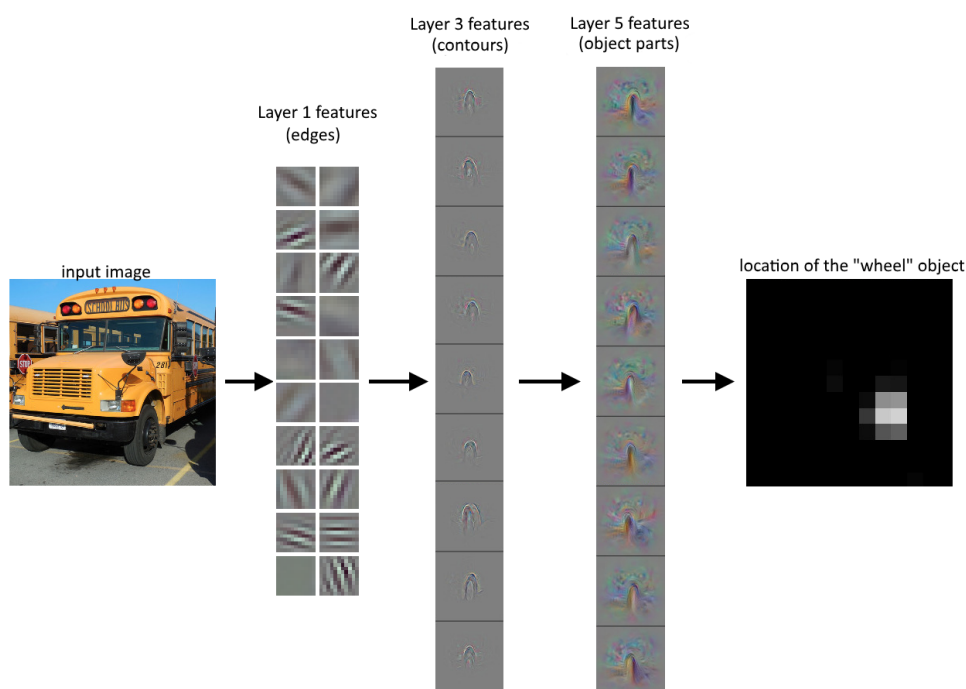
FIGURE 2.8: Hierarchy of features in deep learning applied to image classification. Complex high-level features (object parts) are defined through simpler representations (edges, contours) from preceding hidden layers. This image was prepared using Caffe (Jia et al. 2014) and Deep Visualization Toolbox (Yosinski et al. 2015) software.

The reader may notice that this approach is similar to the idea behind multilayer perceptron described in the previous subsection. In fact, a feedforward MLP with multiple hidden layers trained by raw data is a quintessential example of a deep learning algorithm. However, in recent years a number of more flexible and computationally efficient network architectures have appeared, namely deep convolutional neural networks (CNNs) and deep belief networks (DBN). Besides the breakthrough achieved in the areas of image, speech and text recognition (LeCun, Bengio, and Hinton 2015), these machine learning algorithms have shown promising results in a number of BCI applications (Cecotti and Graeser 2008; Cecotti and Graser 2011; Ren and Wu 2014; Hajinoroozi et al. 2015).

2.5 Conclusion.

This chapter aimed at reviewing the signal processing techniques used in control EEG BCIs. From the engineering perspective a control EEG BCI is essentially an EEG signal processing system that maps the acquired sensor data to one of the known brain states. Immediately after acquisition the EEG signal is extremely noisy and high-dimensional, which makes direct classification of raw data problematic.

A common solution to this problem is to include a preprocessing stage to address the negative effects of EEG signal and a subsequent feature extraction stage that represents input data in a compact form with respect to the physical properties indicative of the mental state. Signal preprocessing most commonly includes filtering in time/frequency domains or spatial filtering using laplacian operator or BSS techniques.

Various mental states induce certain characteristic effects in the observed EEG signal. At the feature extraction stage the preprocessed EEG is encoded in a compact form of feature vectors with respect to these characteristic properties, such as information about the phase or presence of a specific waveform (temporal features), indicative spectral components (spectral features) or their spatial distributions (spatial features). Based on the known observations these feature vectors are then mapped into the corresponding data classes during the classification process. Both linear and non-linear classifiers are widely used in BCI research and recently a powerful concept of deep learning has been introduced to the field.

Chapter 3

EEG source localization. The forward problem.

Electromagnetic source localization is beneficial to many application areas of the EEG. The essence of this process is calculation of cortical currents that produce the recorded surface EEG measurements. The process of EEG source reconstruction takes into account multiple aspects of EEG signal generation, such as human anatomy, electric field propagation in head tissues and cortical current generation. In the following sections these aspects will be discussed, as well as approaches commonly used to model them.

3.1 Introduction to EEG source localization.

As explained previously, the EEG signal represents continuous voltage measurement from the head skin surface, and hence measures secondary effects of electrical brain activity. There is evidence that brain neuronal cells designated to a common task are grouped together into functionally and often anatomically segregated cortical regions (Friston 2011; Sakkalis 2011). For instance, during the motor imagery commands the BCI user produces the power variation patterns that are spatially distinctive, due to such anatomical segregation. Cortical locations of ERD/ERS effects occurring in the mu and beta bands of the EEG can directly indicate the muscles involved in the imaginary task being performed (Pfurtscheller et al. 2006; Kaiser et al. 2014). Hence by finding the motor cortex areas that generate the signal of interest it is possible to infer the imagined type of movement and execute the BCI command associated with it.

Since the location of the signal of interest is highly indicative of the brain state, it is relevant to accentuate such spatial properties in the feature extraction process. The direct analysis of EEG spatial properties is problematic, as the signal acquisition itself suffers from the volume conduction effects. As the neuronal electric fields propagate from the gray matter to the skin surface, they are distorted and spread. This results in ERD/ERS patterns having high spatial correlation, which impairs interpretation of the motor imagery task being performed. One of the challenges in motor imagery BCI design, therefore, is to overcome the low spatial resolution of the EEG.

The cross-electrode correlation due to volume conduction effects can be significantly alleviated by EEG source localization (also referred to as EEG source reconstruction, EEG imaging). The essential idea of source reconstruction is estimation of primary cortical current densities from an EEG recording. Given a forward head model, which couples surface voltages to the currents inside the head, the current distribution is obtained by solving the inverse problem, which aims to find an optimal combination of active current sources for a predefined set of constraints (Baillet, Mosher, and Leahy 2001; Hallez et al. 2007). Here individual sources that comprise the source grid are
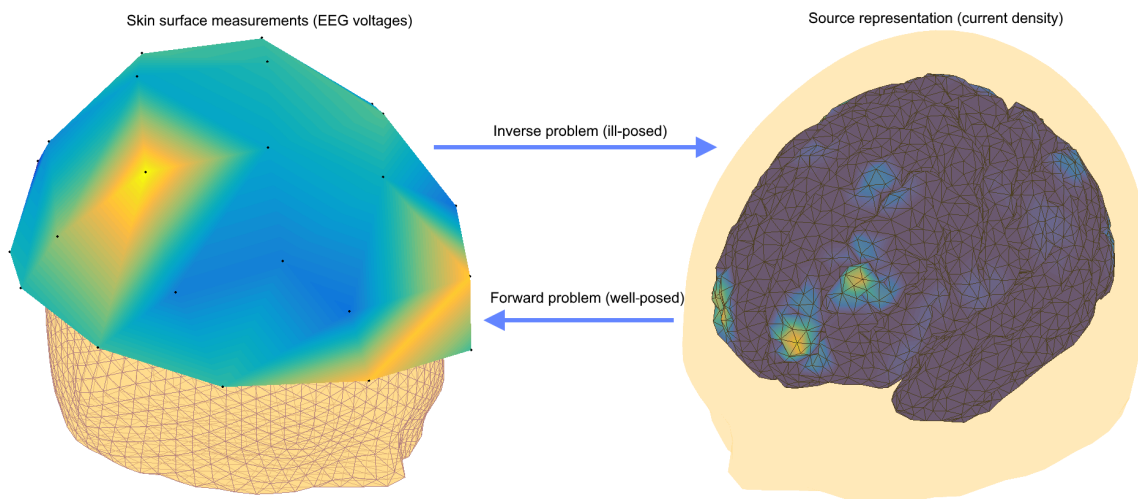
FIGURE 3.1: Forward and inverse problems of EEG
source localization.

represented by current dipoles or multipoles, and within the localization process cortical current density estimates are generally calculated separately for each time sample of the EEG measurement. The source reconstruction process is known to alleviate the negative electrode coupling effects of the EEG signal, hence providing for a more accurate extraction of spatial features. When source localization is applied to a continuous block of data it decomposes the original EEG signal into multiple spatially determined components with respect to the forward model.

In the EEG source reconstruction process, the original surface voltage data is being mapped onto a cortical source grid of higher dimensionality. Given that the number of EEG channels is generally of the order of 30 and the number of current dipoles is of the order of 5000, the source localization problem is severely underdetermined and requires a certain degree of regularization in order to obtain a unique inverse solution.

The majority of source localization methods fit into the generative model described by the following equation:

$$\mathbf{M} = \mathbf{L}\mathbf{D} + \varepsilon \qquad (3.1)$$

Here matrix $\mathbf{M}$ of size m-by-k is the EEG measurement matrix that represents the multivariate signal recorded from m channels over k time samples. Matrix $\mathbf{L}$ of size m-by-n , where n is the number of dipoles in the source model, is generally referred to as the lead field matrix (or gain matrix). Each column of $\mathbf{L}$ couples a unit activation of a particular current dipole to the resulting head surface potentials. Matrix $\mathbf{D}$ of size n-by-k holds the solution to the inverse problem of source reconstruction. It contains the magnitudes of source activations over the time course of the input EEG recording. Finally ε is the noise perturbation matrix, which takes into account the localization error.

Each column of the lead field matrix $\mathbf{L}$ represents the individual forward problem solution for each current dipole in the selected source model. In the field of EEG brain imaging the forward problem means the coupling of the source unit activations to the resulting potentials at the skin surface. Given such cortex-to-scalp electric

coupling it is then possible to find a realistic combination of active sources that would explain the input EEG data (see figure 3.1). This task is called the inverse problem of source localization and the solution to this problem is the cortical topography of current densities, which is generally the desired result of EEG source reconstruction.

3.2   Physics of EEG.

In order to calculate the coupling between cortical sources and the EEG electrodes that comprise the lead field matrix, it is essential to take into account the physics of EEG signal generation.

The scalp EEG recording represents a very large scale measure of electrical dynamics in the brain cortex. A single electrode provides the electric field estimates averaged over tissues incorporating between roughly 100 million to 1 billion neuronal cells (Nunez and Srinivasan 2006). On the individual neuron scale, these electric fields are caused by the mechanisms underlying the generation and propagation of action potentials (AP), which are considered to be the primary carriers for different types of information transmitted over the CNS (Sanei and Chambers 2007). These APs (or nerve impulses) are generated on the cell membrane as a result of a rapid membrane depolarization caused by a sufficient number of excitatory potentials being received from the connected neurons nearly at the same time (see figure 3.3). Even under these conditions however, the generation of an action potential may be thwarted if the neuron receives a
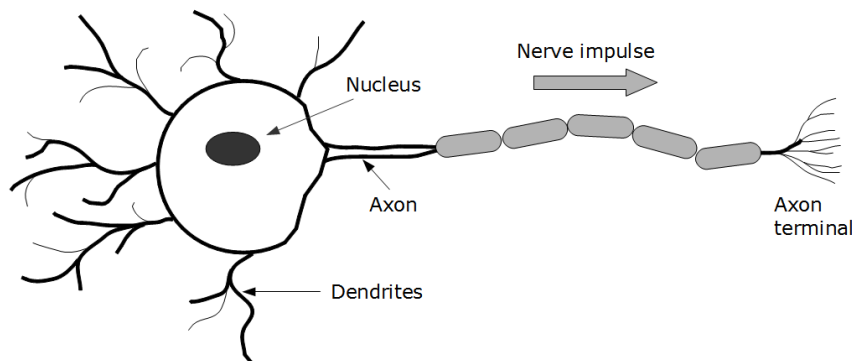
FIGURE 3.2: Basic structure of a nerve cell.
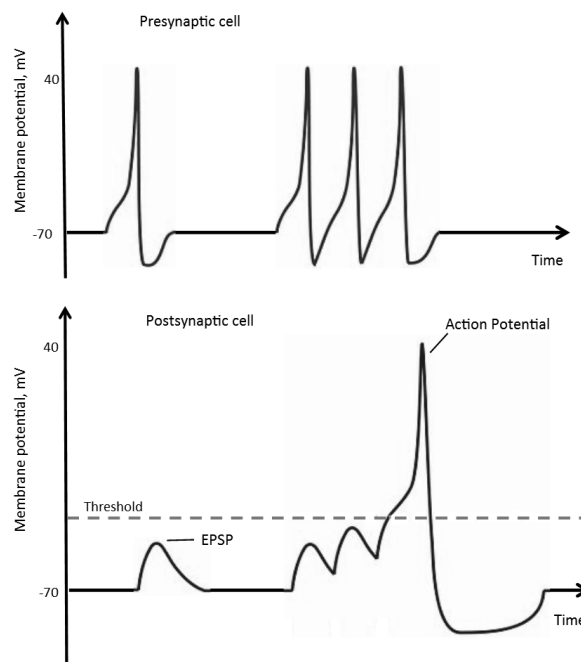
FIGURE 3.3: Principle of AP generation with approx-
imate values of membrane potentials. Electrical spike
at the presynaptic neuron is converted into EPSP at
postsynaptic neuron through electrochemical signal
transmission. A single EPSP is not capable of eliciting
an AP as it does not cross the certain potential thresh-
old at the cell membrane. An AP is generated upon
the reception of multiple EPSPs in a short time course.

sufficient number of inhibitory potentials from other cells. The exci-
tatory and inhibitory potentials occur during the signal transmission
at the neuron's synapses, which are the structures facilitating elec-
trochemical signal transmission between neuronal cells. The cortical
neural cells are very strongly interconnected. For instance, the body
of a large cortical neuron may have as many as 10 000 to 100 000
synapses connected to it. The generation of a single action poten-
tial reflects the activity of a complex network involving millions of
neurons. At synapses the neuronal activity is transmitted chemically
from one nerve cell to another via neurotransmitter emitted from the
presynaptic cell to the specific receptors at the postsynaptic cell. An
excitatory postsynaptic potential (EPSP) that contributes to AP gen-
eration or an inhibitory postsynaptic potential (IPSP) that suppresses
this process are generated at the postsynaptic neuron upon the acqui-
sition of a neurotransmitter by a corresponding receptor (figure 3.3)
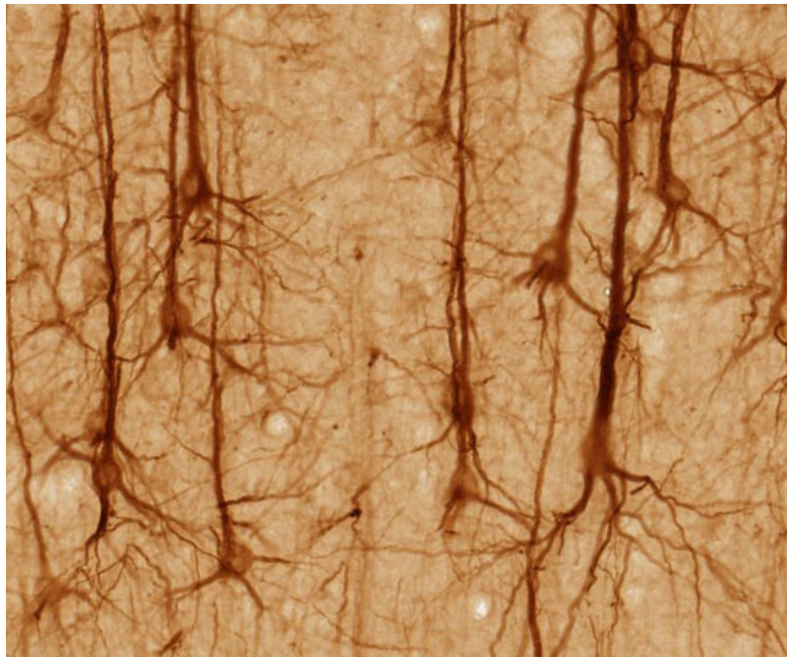
FIGURE 3.4: Imaging of SMI-32 stained pyramidal neurons, showing the parallel alignment of dendrites oriented towards the cortical surface (top). (Image by UC Regents Davis campus, www.brainmaps.org, under CC BY 3.0.)

(Kirschstein and Köhling 2009).

Compared to the individual neurons the EEG electrodes are large and remote. With the skin surface sensors it is impossible to pick the electric activity of a single neuron, since it is so overwhelmed by the activity of nearby cells. Relatively low sensitivity and the complex nature of signal propagation in human head tissues limits the EEG to detection of averaged electric activity from multiple simultaneously active cells. The APs have relatively large amplitude (up to 110 mV), but they have a very short time course of approximately 0.3 ms. Consequently, the probability of their simultaneous occurrence and hence their contribution to the surface potentials is very low. On the other hand, postsynaptic potentials underlying the AP generation process, have smaller amplitude (0.1-10 mV), but significantly longer duration (10-20 ms). Hence, the postsynaptic potentials are more likely to create sufficient electric field superposition to be detectable by the surface sensors, and therefore they are considered to be the primary EEG generators (Baillet, Mosher, and Leahy 2001;

Hallez et al. 2007; Kirschstein and Köhling 2009).

In addition to the requirement for neuronal synchrony, nerve cells must conform to certain spatial orientation properties in order to achieve such superposition. Adjacent neurons must be arranged in a way to amplify the resulting electric fields, and such alignment properties can be found in large populations of pyramidal neurons that form the grey matter of the human brain. The grey matter is a 2-4 mm thick layer mainly consisting of neuronal cell bodies, glial cells and capillaries that form the folded structure of the cerebral cortex of the brain. The neuronal patterns of grey matter are known to play the key role in perception, memory, attention, awareness and consciousness. The apical dendrites of these neurons are oriented orthogonally to the cortical surface and parallel to each other, providing for electric field superposition (Fig. 3.4). Therefore, these cells are considered to be the main contributors to EEG signal generation (Nunez and Srinivasan 2006).

However, not all of the neurons that form the cerebral cortex have such orientation features. The extracellular potential fields of cells with arbitrarily oriented dendrites may be canceled by the adjacent neuronal activity, and therefore the contribution of such cells to the EEG generation is highly unpredictable. Hence, it can be stated that the EEG predominantly reflects the postsynaptic electrical activity of a certain subgroup of neurons with specific alignment properties.

3.3 EEG source modelling.

A practical way to formalize the function of a complex system such as a human brain is to build a model that follows the operation of the system as closely as possible. In combination with relevant physiological observations the model may then be employed to characterize the relationships between the system's properties, e.g., the electrical brain sources and EEG measurements. As was discussed earlier, the EEG signal is mainly generated by the synchronous activity of large populations of certain types of neurons with common expectations about their location and orientation properties. In the following subsections the mathematical modelling of such aggregated activity is

addressed, which is required for the forward problem solving process.

3.3.1   The current dipole.

Functional EEG analysis is typically restricted to the frequency band between 0.1 and 100 Hz. The wavelengths of such electric fields in the volume conductor are overwhelmingly larger than the scale of the human brain. This means that although the brain activity changes over time, these dynamics occur considerably slower than the propagation effects of electromagnetic fields. Therefore, the neuronal electric field modelling is typically performed under quasistatic conditions (Baillet, Mosher, and Leahy 2001).

The occurrence of IPSPs and EPSPs in a pyramidal neuron creates the current source-sink configuration within the cell, therefore on the microscopic level this process is typically modelled by a current dipole. However, as was discussed earlier, individual neuronal activity does not produce sufficient field to be observable by EEG. The near-parallel alignment of pyramidal cells in the cerebral cortex (see Fig. 3.4) provides for the superposition of resulting electric fields. Therefore, on the macroscopic level a cluster of synchronously active neurons on a small nearly flat cortical patch can also be modelled as a single current dipole.

On the individual synapse level the current sink at location $\mathbf{r}_1$ describes the removal of positively charged ions (e.g. K^+) or the inflow of negatively charged ions (Cl^-) which corresponds to the EPSP generation at the apical dendrites. The current source at position $\mathbf{r}_2$ represents the injection of positive ions through the cell membrane. The current density $\mathbf{J}$ at an arbitrary location $\mathbf{r}$ in the vicinity of a dipole can be obtained from the following equation:

$$\nabla \cdot \mathbf{J} = I\delta(\mathbf{r} - \mathbf{r}_2) - I\delta(\mathbf{r} - \mathbf{r}_1) \qquad (3.2)$$

Here I stands for the current within the dipole and δ is the delta function. The current density $\mathbf{J}$ can be related to the electric field

through Ohm's law:

$$\mathbf{J} = \sigma\mathbf{E} , \tag{3.3}$$

where σ is the conductivity of the volume conductor. In EEG source localization it is typical to assume homogenous and isotropic tissue conductivity, which significantly reduces the complexity of the forward problem but with additional errors.

The potential V can be linked with electric field $\mathbf{E}$ through the Poisson's equation:

$$\mathbf{E} = -\nabla V \tag{3.4}$$

Here ∇V is a directional measure pointing to the direction of the most rapid increase of scalar V. Next, the current density of a dipole and the resulting potential field at $\mathbf{r}$ can be related by combining equations (3.2), (3.3) and (3.4):

$$\nabla \cdot (\sigma\nabla(V)) = -I\delta(\mathbf{r} - \mathbf{r}_2) + I\delta(\mathbf{r} - \mathbf{r}_1) . \tag{3.5}$$

The explicit extension of (3.5) in the Cartesian coordinate system yields the following form:

$$\frac{\partial}{\partial x}(\sigma\frac{\partial V}{\partial x}) + \frac{\partial}{\partial y}(\sigma\frac{\partial V}{\partial y}) + \frac{\partial}{\partial z}(\sigma\frac{\partial V}{\partial z}) = -I\delta(x - x_2)\delta(y - y_2)\delta(z - z_2)$$
$$+I\delta(x - x_1)\delta(y - y_1)\delta(z - z_1) . \tag{3.6}$$

Equation (3.6) relates the dipole current density I to the resulting potential V in a homogenous and isotropic volume conductor.

3.3.2 Boundary conditions.

The electric field produced by neuronal activity propagates through various tissue types on the path from cerebral cortex to the EEG electrode. These head tissues have different conductive properties, which substantially complicates the simultaneous analysis of such configurations. Therefore, it is common to consider the head volume as a set of homogenous volumetric compartments with formalized
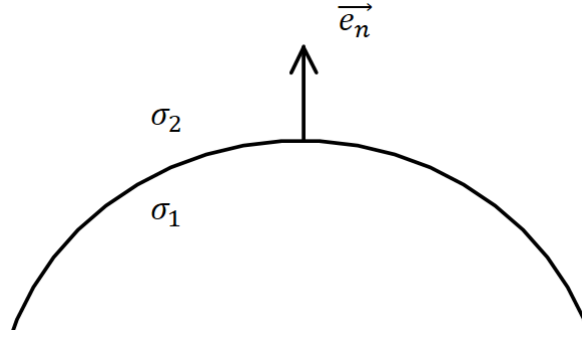
FIGURE 3.5: Boundary between two compartments with conductivity σ_1 and σ_2. Vector $\vec{e_n}$ is the boundary surface normal.

boundary conditions describing the field transition between the volumes with different conductivities as shown in figure 3.5.

The first boundary condition follows from the rationale that there is no charge pile up at the interface between two different tissues, meaning that the current is continuous as it leaves the volume with conductivity σ_1 and enters the volume with conductivity σ_2. This assumption is referred to as the Neumann boundary condition (Hallez et al. 2007):

$$\mathbf{J}_1 \cdot \mathbf{e}_{n1} = \mathbf{J}_2 \cdot \mathbf{e}_{n2}$$
$$(\sigma_1 \nabla V_1) \cdot \mathbf{e}_{n1} = (\sigma_2 \nabla V_2) \cdot \mathbf{e}_{n2} \, , \qquad (3.7)$$

where $\mathbf{e}_{n1/2}$ denote the direction of surface normal at the boundary interface. In addition, it is assumed that current does not propagate outside of the human body, due to the low air conductivity. Hence, at the skin-air boundary the condition (3.7) takes the following form:

$$\mathbf{J}_1 \cdot \mathbf{e}_{n1} = 0$$
$$(\sigma_1 \nabla V_1) \cdot \mathbf{e}_{n1} = 0 \, . \qquad (3.8)$$

The second boundary condition is a simple assumption that no

electric charge can accumulate at the interface between tissues (excluding skin-air boundary). In this case it is referred to as the Dirichlet boundary condition (Hallez et al. 2007):

$$V_1 = V_2 \ . \tag{3.9}$$

3.3.3 Dipole moment.

As was discussed earlier, both the individual and the locally aggregated neuronal activity fits into the current dipole representation. In such a configuration the amount of current I injected by the source is equal to the amount of current removed by the sink. The magnitude of local electrical activity can be reflected by the dipole moment parameter $\mathbf{d}$ (Hallez et al. 2007):

$$\mathbf{d} = I p \mathbf{e_d} \ , \tag{3.10}$$

where p is the length between source and sink and $\mathbf{e_d}$ is the unit vector, which represents the dipole orientation (direction from sink to source). The scalar value of $\mathbf{d}$ is defined as:

$$d = |\mathbf{d}| = I p \ . \tag{3.11}$$
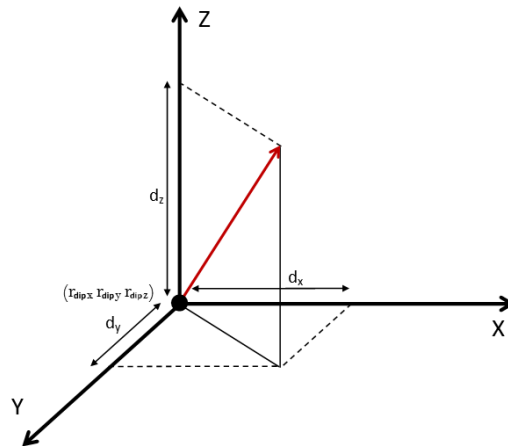
FIGURE 3.6: The six parameters defining a source in EEG imaging. Three values (r_x, r_y, r_z) denote the source location and (d_x, d_y, d_z) are the Cartesian components of dipole moment.

It is common to represent such a current dipole as a set of components oriented along the Cartesian axes. Hence, an arbitrarily directed dipole is typically modelled by three dipoles with fixed orientations:

$$\mathbf{d} = d_x\mathbf{e_x} + d_y\mathbf{e_y} + d_z\mathbf{e_z} \ . \tag{3.12}$$

The location of a dipole $\mathbf{r}_{dip}$ is generally considered to be in the middle between the source and the sink. Generalizing the aforementioned modelling aspects, a single EEG source representing a small patch of cerebral cortex can be described by 6 parameters: three values defining the source coordinates and the moment described by three Cartesian components d_x, d_y and d_z (Fig. 3.6).

Likewise, the surface potential V at scalp location $\mathbf{r}$ produced by such a dipole at location $\mathbf{r}_{dip}$ is described in a following manner as given in (Baillet, Mosher, and Leahy 2001)

$$\mathbf{V}(\mathbf{r},\mathbf{r}_{dip},\mathbf{d}) = d_x V(\mathbf{r},\mathbf{r}_{dip},\mathbf{e_x}) + d_y V(\mathbf{r},\mathbf{r}_{dip},\mathbf{e_y}) + d_z V(\mathbf{r},\mathbf{r}_{dip},\mathbf{e_z}) \ . \tag{3.13}$$

3.3.4   General forward problem formulation.

In the previous sections we have formulated the mathematical basis for EEG source modelling. Now it is possible to define the forward problem of source reconstruction and relate an individual current dipole $\mathbf{d}$ at location $\mathbf{r}_{dip}$ to the EEG sensor at location $\mathbf{r}$. The forward problem solution in this case is the skin surface potential $l(\mathbf{r}, \mathbf{r}_{dip}, \mathbf{d})$ at the EEG electrode, which can be obtained from the Poisson's equation in (3.6). When taking into account multiple dipole sources and quasi-static conditions, the resulting potential at $\mathbf{r}$ is the linear instantaneous superposition of potentials produced by all given sources (Baillet, Mosher, and Leahy 2001):

$$V(\mathbf{r}) = \sum_i l(\mathbf{r}, \mathbf{r}_{dip\,i}, \mathbf{d}_i) = \sum_i l(\mathbf{r}, \mathbf{r}_{dip\,i}, \mathbf{e}_i)d_i \ . \tag{3.14}$$

The EEG signal is generally recorded from multiple locations spanning the head surface area. Hence, for n dipole sources and m EEG electrodes the surface potential field becomes:

$$\mathbf{V} = \begin{bmatrix} V(\mathbf{r}_1) \\ \vdots \\ V(\mathbf{r}_m) \end{bmatrix} = \begin{bmatrix} l(\mathbf{r}_1, \mathbf{r}_{dip_1}, \mathbf{e}_1) & \cdots & l(\mathbf{r}_1, \mathbf{r}_{dip_n}, \mathbf{e}_n) \\ \vdots & \ddots & \vdots \\ l(\mathbf{r}_m, \mathbf{r}_{dip_1}, \mathbf{e}_1) & \cdots & l(\mathbf{r}_m, \mathbf{r}_{dip_n}, \mathbf{e}_n) \end{bmatrix} \begin{bmatrix} d_1 \\ \vdots \\ d_n \end{bmatrix} = \mathbf{L} \begin{bmatrix} d_1 \\ \vdots \\ d_n \end{bmatrix}.$$

(3.15)

The matrix $\mathbf{L}$ in (3.15) is referred to as lead field matrix or gain matrix representing the volume conductor model, which is the target of forward head modelling. More specifically, the columns of $\mathbf{L}$ represent the potentials at m skin surface points produced by each individual dipole given its moment equals 1. In equation (3.15) the fixed source orientations are assumed. One way to take into account the unrestricted source orientations is to consider 3 current dipoles aligned along the Cartesian axes at each location $\mathbf{r}_{dip}$, which expands the formulation into:

$$\mathbf{V} = \begin{bmatrix} l(\mathbf{r}_1, \mathbf{r}_{dip_{1x}}) & l(\mathbf{r}_1, \mathbf{r}_{dip_{1y}}) & l(\mathbf{r}_1, \mathbf{r}_{dip_{1z}}) & \cdots & l(\mathbf{r}_1, \mathbf{r}_{dip_{ny}}) & l(\mathbf{r}_1, \mathbf{r}_{dip_{nz}}) \\ \vdots & \vdots & \vdots & \ddots & \vdots & \vdots \\ l(\mathbf{r}_m, \mathbf{r}_{dip_{1x}}) & l(\mathbf{r}_m, \mathbf{r}_{dip_{1y}}) & l(\mathbf{r}_m, \mathbf{r}_{dip_{1z}}) & \cdots & l(\mathbf{r}_m, \mathbf{r}_{dip_{ny}}) & l(\mathbf{r}_m, \mathbf{r}_{dip_{nz}}) \end{bmatrix} \begin{bmatrix} d_{1x} \\ d_{1y} \\ d_{1z} \\ \vdots \\ d_{ny} \\ d_{nz} \end{bmatrix} =$$

$$= \mathbf{L}\mathbf{D}$$

(3.16)

Equation (3.16) links the current dipole moments to the resulting surface potentials at multiple sensors for a given source model and EEG electrode montage. One can notice that it is very similar to the generative model of source localization from equation (3.1). The difference is that in practice each value of the EEG recording M represents the voltage (potential difference) between a particular electrode and the reference electrode, while V represents the surface potentials at the same electrode position. Hence, it is generally necessary to re-reference the EEG data, for example to a common average reference, to obtain surface potential approximations.

3.4   Head volume modeling.

3.4.1   Head geometry.

Previously we have formulated the forward problem of source local-
ization as the calculation of skin surface potentials at the predefined
EEG electrode locations induced by the set of brain current sources
comprising the source model. On the path from cortex to surface
sensor the electric field passes through a number of different tissues,
each typically modeled as an isotropic homogeneous volume con-
ductor with formalized boundary conditions at tissue interfaces. For
each dipole-electrode pair the forward solution is largely defined by
the spatial configuration of tissues on this path, and hence by the
chosen geometry of the head and tissue conductive properties.

There are various approaches to head model generation applied
in the field of EEG source reconstruction. In its simplest form the
head geometry can be represented by a single spherical boundary
with isotropic homogeneous conductivity within its volume. In this
case the variation of conductivity in different tissues is not taken into
account directly, but can be averaged over all brain compartments.
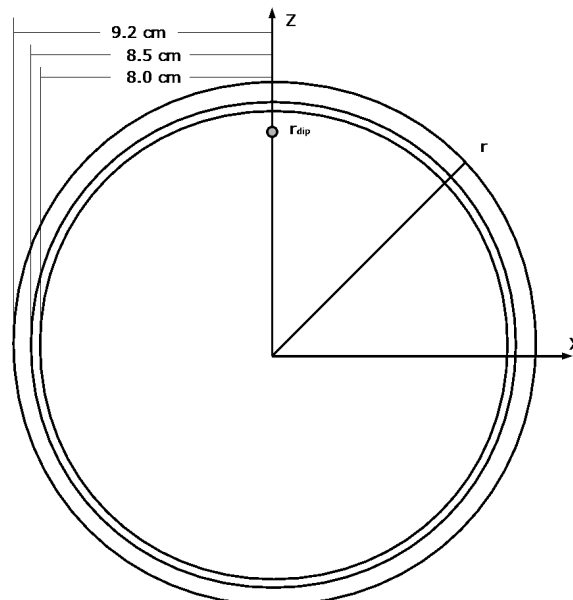
FIGURE 3.7: Visualization of a three-shell concetric
sphere model.

Such head representation substantially reduces the calculation complexity of the forward modeling, but obviously results in localization errors due to the approximations made.

The further development of a single-shell model is a multi-shell head geometry, typically incorporating three or four concentric spheres each representing a boundary between different head tissues as shown in figure (3.7). Such a model typically accounts for brain volume, cerebro-spinal fluid (CSF), skull bone and scalp tissues (Baillet, Mosher, and Leahy 2001).

Since the CSF conductivity is relatively large compared to other head tissues, this layer is often excluded from the analysis, which yields a simplified three-shell model. The typical radii of surface boundaries used in such representation are 8.0 cm, 8.5 cm and 9.2 cm for brain tissue, skull and skin respectively (Hallez et al. 2007).

While spherical head models are computationally cheap and provide sufficient accuracy for some imaging applications, it is obvious that such representation does not reflect the realistic geometry properties of the human head. In reality, the human head is inhomogeneous, anisotropic and has a more complex configuration of tissues.
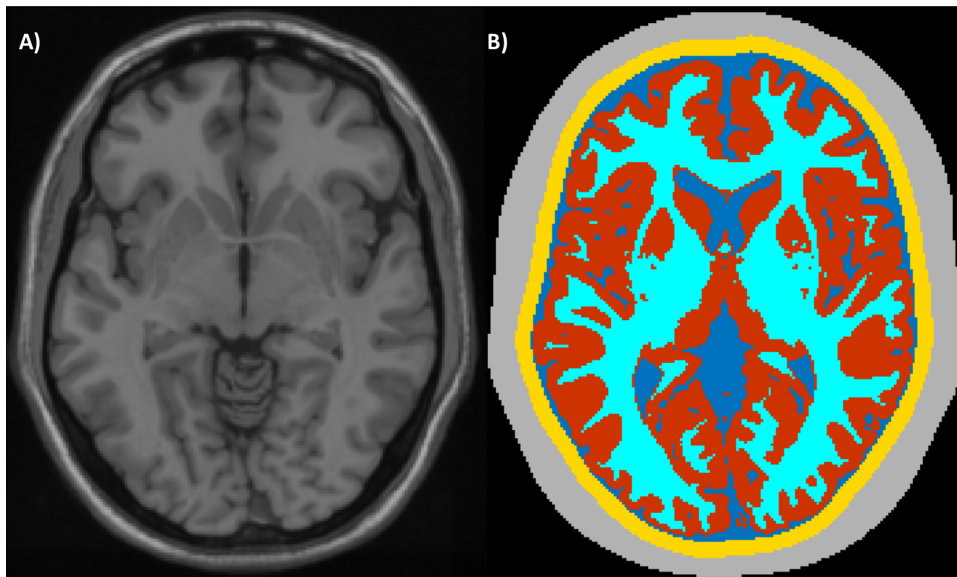
FIGURE 3.8: A) A single slice of 1 mm resolution anatomical MRI image. B) Tissue segmentation map for the corresponding slice.

A data-driven approach based on MRI imaging is a more accurate way for realistic head modeling therefore. The anatomical MR image provides a detailed high-resolution volumetric imaging of tissues with spatial resolution of up to 0.5 mm, where contrast represents tissue magnetization properties. With the subsequent analysis of MR images it is possible to identify the particular types of tissues and obtain a comprehensive configuration of head compartments as shown in figure (3.8). This task is carried out by various automated and semi-automated MRI segmentation algorithms, which solve the classification problem for each voxel of the image with regards to the general anatomy expectations and adjacent areas. In addition to the electromagnetic head modeling these segmentation methods are employed in a wide variety of medical applications such as surgical planning, post-surgical assessment, abnormality detection and many others (Balafar et al. 2010).

The anatomical MRI and tissue segmentation maps provide for a comprehensive conductive head model definition. The resulting head volume is typically defined as a set of volumetric elements (tetrahedral or cuboid) spanning the whole 3D volume of the head, or alternatively as a set of tessellated boundaries between the head tissues. The particular choice of representation is closely connected to the numerical method used to solve the forward problem, which will be discussed in later sections.

3.4.2   Tissue conductivity.

Besides the head geometry, the forward solution to (3.16) is largely dependent on the conductive properties of the modelled tissues. For a long time EEG/MEG neuroimaging relied on the general conductivity values obtained from post-mortem tissues, which typically led to controversial results, due to subject-individual changes in tissues after death. Commonly the results obtained this way vary vastly: 0.22-0.75 S/m for skin tissue, 0.0081-0.015 S/m for skull, and 0.22-0.33 S/m for brain volume. The CSF conductivity was quite precisely estimated to be 1.79 S/m.

However, more recently the conductivity estimates can be empirically obtained in vivo by means of electrical impedance tomography (EIT), which is an imaging method based on injection of relatively small alternating currents of 1-10 μA between pairs of sensors (Gonçalves et al. 2003). Similar to EEG source imaging this method relies on solution of the ill-posed inverse problem, which in the case of thorough anatomical regularization can be quite computationally intensive. The measurement accuracy has recently been improved with the development of functional EIT (f-EIT) based on continuous imaging in multiple physiological states associated with linear changes in conductivity. In addition, the acquisition of abstract parameters of the body, currently f-EIT represents a promising medical imaging technique with multiple clinical monitoring applications, continuously providing information about lung ventilation, brain haemorrhage, cerebral ischemia, hypoglycemia and many other conditions (Bayford and Lionheart 2004). Applied to EEG source localization, EIT can provide individual estimates of tissue conductivity maps allowing for more accurate forward head modelling with realistic heterogeneous (location dependent) tissue representation. As was recently shown by Dabek et al., the individually tailored head model provided by frequency-dependant EIT data significantly improves the accuracy of EEG source analysis (Dabek et al. 2016). For comparison, the average conductivity values at 2 Hz obtained in the aforementioned research are 0.34 S/m for skin and brain and 0.0066 S/m for skull. In the range from 11 to 127 Hz the corresponding conductivities increased by 1.6 % for brain and scalp tissues and by 6.7 % for skull.

In practice besides being inhomogeneous the conductivity of various head tissues is often anisotropic, meaning that it is direction dependent. For instance, the bone structure of skull is comprised of two hard layers with a tangentially oriented spongiform layer between them. Consequently, the skull conductivity in the direction normal to the surface is about 10 times smaller than in the tangential direction. The effect of such skull anisotropy on forward and inverse modelling was thoroughly studied and quantified in (Marin et al. 1998).

3.5   Forward problem solving.

3.5.1   Simple head models.

As pointed out earlier, the inverse problem of EEG source reconstruction relies on the prior knowledge about the nature of the EEG signal and human anatomy, which are partially embedded in the forward problem solution $\mathbf{L}$ in (3.16).

Generally the forward problem is treated as multiple simpler problems coupling each individual cortical current source to the induced potential value at the modelled skin surface. The potential at point $\mathbf{r}$ created by a single current dipole $\mathbf{d}$ at location $\mathbf{r}_{dip}$ in infinite homogenous isotropic volume with conductivity σ can be estimated as:

$$V(\mathbf{r}, \mathbf{r}_{dip}, \mathbf{d}) = \frac{d(\mathbf{r} - \mathbf{r}_{dip})}{4\pi\sigma \left\| \mathbf{r} - \mathbf{r}_{dip} \right\|^3} \; . \tag{3.17}$$

This formulation can be simplified if we assume a current dipole to be set at the origin of the coordinate system and aligned in along the z-axis:

$$V(\mathbf{r}, 0, d) = \frac{d\cos\theta}{4\pi\sigma \left\| \mathbf{r} \right\|^2} \; , \tag{3.18}$$

where θ is the angle between $\mathbf{r}$ and the z-axis. As can be seen from (3.18) the potential attenuates with $1/r^2$. The coordinate system may be rotated in a particular way in order to obtain similar solutions for the x- and y-components of dipole moment.

The concentric sphere model generally assumes homogeneity and isotropy of volumes encapsulated by the spheres. A simple analytic solution for the forward problem for such model was described in (Salu et al. 1990). Based on geometrical configuration described in figure 3.7 the potential field at scalp point $\mathbf{r}$ in the xz-plane induced by an arbitrarily oriented current dipole at location $\mathbf{r}_{dip}$ on z-axis can be found by solving the following:

$$V = \frac{1}{4\pi\sigma R^2} \sum_{i=1}^{\infty} \frac{X(2i+1)^3}{g_i(i+1)i} b^{(i-1)}[id_r P_i(cos(\theta)) + id_t P_i{}^1(cos(\theta))] \; , \tag{3.19}$$

where

$$g_i = [(i+1)X + i][\frac{iX}{i+1} + 1] + \qquad (3.20)$$
$$+ (1-X)[(i+1)X + i](f_1{}^{i_1} - f_2{}^{i_1}) - i(1-X)^2(\frac{f_1}{f_2})^{i_1}$$

In this equation R is the radius of the skin boundary in meters; σ is the conductivity of skin and brain volumes in S/m; X - unitless ratio between skull bone and brain (or skin) conductivities; b is the unitless relative distance to the dipole from the center; θ is the polar angle between the z-axis and the radius towards surface location r; d_r and d_t are radial and tangential dipole components respectively; $P_i(\cdot)$ and $P_i^1(\cdot)$ are the Legendre polynomial and the associated Legendre polynomial respectively; i is the series index; i_1 is an auxiliary variable with $i_1 = 2i + 1$; f_1 is relative distance with $f_1 = r_1/R$, where r_1 is the radius of brain-skull boundary; f_2 is relative distance with $f_2 = r_2/R$, where r_2 is the radius of skull-scalp boundary.

Also, this forward problem solution method was extended in order to handle anisotropic volume conductors, where the conductivity in the tangential direction can be set to be different from the radial conductivity (Zhang 1995) (Munck and Peters 1993).

3.5.2 Realistic head models.

As discussed earlier the realistic head geometry is generally obtained from the anatomical MRI with subsequent image segmentation. The task of forward problem solving in such settings is complex due to asymmetry and irregularity of head compartments, hence it is typically reduced to multiple simpler problems depending on the particular numerical method employed. The finite element method (FEM) and the finite difference method (FDM) are computational numerical methods that are most commonly applied to such physical problems. More specifically these methods are used to solve multiple partial differential equations describing the physical processes of interest defined in multiple simple volumetric elements spanning the whole 3D domain under analysis. As a result this produces a volume conduction model, which is a comprehensive definition of electric
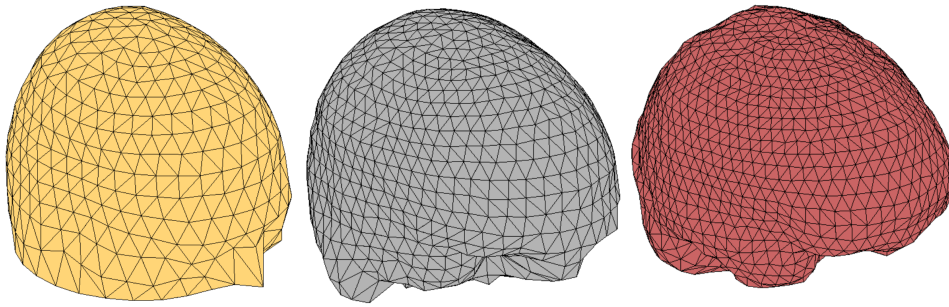
FIGURE 3.9: Triangulated surface boundaries of realistic head model used with BEM. From left to right: skin-air boundary, skull-skin boundary, brain-skull boundary.

field transfer between the neighboring volumetric elements. Given such a definition it is then possible to calculate the columns of lead field matrix by analyzing electric field transfer between each source and the EEG electrodes.

The lead field obtained by these methods shows a narrow point spread function, meaning that the scalar potential field generated by a single dipole has a relatively small skin surface area (Li and Yan 2009; Vattaa et al. 2010). Hence, it is recommended to apply FEM and FDM to EEG forward problem solving, when very accurate anatomical data and precise electrode co-registration are available. The FDM and FEM solvers commonly used to obtain the volume conduction model are provided by FNS software (Dang and Ng 2011) and BESA, and are a part of the Fieldtrip toolbox for Matlab (Oostenveld et al. 2010).

The boundary element method (BEM), which originated in the early 1960s, is a numerical method employed in a wide range of engineering and physical applications (Cheng and Cheng 2005). More specifically BEM is used to solve multiple integro-differential equations. In contrast to FEM and FDM, this computational method considers the head geometry to be a set of surfaces, which represent interfaces between different tissue types (figure 3.9), rather than a set of identical volumetric elements filling the whole problem domain. In order to solve the integral equations these surfaces or boundaries

are tessellated to preserve the natural head geometry and are represented as multiple triangular 2D elements. In BEM the volume encapsulated by the boundaries is assumed to be an homogeneous isotropic conductive medium with a set of boundary conditions at the interfaces. When skull anisotropy is not taken into account the forward problem solutions provided by BEM typically converge to FEM and FDM results. A number of software solvers, which implement the BEM, can be found in Fieldtrip toolbox for Matlab (Oostenveld et al. 2010).

3.5.3 Precision in forward modelling.

In the previous sections theoretical framework of forward head modelling was introduced. The product of such modelling is lead field matrix, which is mainly defined by the choice of head geometry, allowed source locations and EEG electrode positions. Intuitively, the most accurate source reconstruction is achieved when these prerequisites precisely reflect the actual experimental setup during the EEG recording. In practice this requires an anatomical MRI scan of each subject and accurate electrode co-registration at each recording session using specialized equipment, such as xensor from ANT Neuro (Product page) or PATRIOT digitizer from Polhemus (Product page). These requirements are problematic for practical assisitive BCIs, however averaged head atlases such as ICBM 152 template (Collins et al. 1999; Fonov et al. 2009; Fonov et al. 2011) with standardized electrode locations offer a trade-off between the design complexity and accuracy of source reconstruction.

In 2013 Zeynep Acar and Scott Makeig have published a comprehensive analysis of localization errors caused by inaccurate forward modelling (Acar and Makeig 2013). By taking the individual head model with digitized electrode positions as a reference this report quantified the localization errors produced, when a simple spherical model or the realistic MNI head template were used in source reconstruction. In the ideal case of noise-free EEG data the median localization errors of 5 mm were observed with MNI template and 12.4 mm with spherical head model. The electrode co-registration error induced by shifting the electrode locations by $5 \deg$ in one direction

resulted in median localization errors of 4-5 mm. These results were obtained for noise-free simulated EEG data. In a practical real-life scenario however, such localization errors may be insignificant considering the low SNR of EEG and limitations of source reconstruction methods applicable in real-time. Despite the certain degree of forward modelling errors, the use of source reconstruction with realistic template models and heuristic electrode locations is still beneficial for EEG BCI signal processing, as will be shown in chapters 5 and 6 of this thesis.

3.6   Conclusion.

This chapter was dedicated to the overview of forward head modelling for EEG source localization. Specifically, neurophysiological basis underlying the EEG signal generation was discussed and mathematical framework for the comprehensive modelling of such processes was introduced.

In summary, EEG signal is recorded from scalp surface by non-invasive metal electrodes in a form of voltages between each individual electrode and the reference ground. The measured potentials are induced at the skin surface by the primary currents of large populations of specific type of neurons that are oriented in parallel and located within 4-5 mm from the cortical surface of the brain. These neuronal populations are generally modelled as current dipoles and propagation effects of the produced fields are considered to be much slower than the neuronal dynamics. The matching alignment of these cells providing for field amplification and quasi-static assumptions yield, that the EEG signal at each measurement point on scalp is a *linear instantaneous superposition* of distributed brain neuronal activity.

The product of forward modelling necessary for source reconstruction is a lead field matrix, which relates cortical currents to the resulting EEG measurements. Head geometry, source model and EEG electrode positions are the essentials required to obtain the lead field. After these design parameters are defined the lead field matrix is calculated using a solver based on BEM, FEM or FDM. In the

ideal case the highest source localization precision with noise-free EEG data is achieved with individual head models (obtained from subject-specific anatomical MRI) and digitized EEG electrode locations.

Chapter 4

EEG source localization. The inverse problem.

The aim of the forward problem of source localization is to quantitatively link the cortical dipolar activations to the produced scalp potential fields. After such a coupling has been obtained it is then possible to explain the EEG data through a realistic combination of active cortical sources, which is the aim of the inverse problem of EEG source localization. This chapter is dedicated to the various aspects of EEG inverse solutions, including numerical approaches to distributed source localization, constraints to the inverse problem and examples of EEG source reconstruction applied to simulated data.

4.1 Inverse solutions.

In the inverse problem of source analysis matrix $\mathbf{L}$ is a known prerequisite, the skin potentials obtained by EEG are stored in a measurement matrix $\mathbf{M}$ and matrix $\mathbf{D}$ is the unknown of the problem. The noise perturbation matrix is commonly added to the model in order to represent the error introduced by the inverse solution. As given in the previous chapter the final form of the generative model of source reconstruction then becomes:

$$\mathbf{M} = \mathbf{L}\mathbf{D} + \varepsilon \; . \tag{4.1}$$

Under this notation the aim of the inverse problem is to find an estimate set of dipoles $\hat{\mathbf{D}}$ satisfying the predefined ε given the pre-calculated lead field $\mathbf{L}$ and EEG measurements $\mathbf{M}$.

Typically practical BCI implementations impose high computational requirements, due to the complexity of signal processing sequence and real-time constraints. Therefore, in online analysis scenarios the choice of inverse solver is generally limited to a family of linear source localization methods. This class of inverse solutions is linear in the sense that the cortical currents $\hat{\mathbf{D}}$ are obtained through a simple matrix multiplication of inverse operator by a segment of sensor data:

$$\hat{\mathbf{D}} = \mathbf{GM} \,, \tag{4.2}$$

where $\mathbf{G}$ is an inverse operator obtained as a certain approximation of the lead field matrix inverse.

At each time point of the EEG measurement the scalp potential map is induced by the distributed activity of billions of brain neurons. In order to accurately represent the complex cortical activity with anatomically realistic geometry it is necessary to use a dense grid of sources, typically employing thousands of dipoles spanning the brain volume. Considering that the number of EEG channels generally varies from 14 to 128 and even more in high-density montages, this leads to the fundamental difficulty of the EEG inverse problem - the non-uniqueness of its solution. Infinite number of combinations of active neuronal sources can lead to the same skin surface potential map, meaning that the EEG source localization is an example of an ill-posed inverse problem.

However, the integration of multiple constraints to such problem can limit the solution space and point to a unique combination of active sources. These constraints are the formalized representations of various hypotheses about biophysical processes in the brain, and in combination with various computational numerical techniques this results in numerous methods and algorithms of source localization.

The following sections describe a number of inverse solutions based on a flexible framework of penalized least squares problem. In these methods the solution is obtained by minimizing the cost function, that typically incorporates a residual error term $\|\mathbf{M}-\mathbf{LD}\|_2$ plus

a regularization term taking the form of $\lambda\|\mathbf{\Gamma D}\|_p$:

$$\hat{\mathbf{D}} = \arg\min_{\mathbf{D}}\|\mathbf{M} - \mathbf{LD}\|_2 + \lambda\|\mathbf{\Gamma D}\|_p \qquad (4.3)$$

Here $\mathbf{\Gamma}$ generally represents the linear matrix operator that implements a certain assumption about the desirable inverse solution and λ is the regularization parameter defining the relative importance of such an assumption.

The reader may notice that the EEG source localization and the blind source separation techniques share a similar generative model (comparing (2.8) to (4.1)). Indeed the both approaches aim to explain the given multivariate signal as a certain mixture of independent latent variables (mixing matrix in BSS and lead field in source localization). However, the mixing models and the latent sources are obtained quite differently with these two techniques. In BSS the mixing matrix is calculated in a purely data-driven manner from the available signal observations with respect to a certain assumed measure of statistical independence of sources. The source components which in BSS generally have the same dimensionality as the original data are obtained by simply projecting the given measurements onto the mixing matrix inverse (unmixing matrix). On the other hand, in source reconstruction the mixing model or lead field matrix is obtained analytically by solving the forward problem as was described in the previous chapter, while dimensionality of source data is generally assumed to be few orders higher than of the given sensor measurements. The source components then are obtained by solving the ill-posed inverse problem as will be shown in the following sections.

4.1.1 Minimum norm estimates.

Minimum norm estimates (MNE) inverse solver aims to find a solution with minimum power based on the minimization of l-2 norm of a solution vector (Baillet 1998; Grech et al. 2008). MNE corresponds to Tikhonov regularization and the solution $\hat{\mathbf{D}}$ is obtained as a vector or matrix that minimizes the following cost function:

$$F_{MNE}(\mathbf{D}) = \|\mathbf{M} - \mathbf{LD}\|_2 + \lambda\|\mathbf{D}\|_2 \,, \qquad (4.4)$$

where $\lambda > 0$ is the Tikhonov regularization parameter, which is used to control the relative weight between the penalty for inaccurate reconstruction (first term) and penalty for large norm of the solution vector (second term). By taking the derivative of the cost function, setting it to zero and solving the equation for $\mathbf{D}$ it is possible to obtain an inverse operator $\mathbf{G}_{MNE}$ and then the solution $\hat{\mathbf{D}}$:

$$\hat{\mathbf{D}}_{MNE} = \mathbf{L}^T(\mathbf{L}\mathbf{L}^T + \lambda\mathbf{I}_m)^{-1}\mathbf{M} = \mathbf{G}_{MNE}\mathbf{M} \ . \qquad (4.5)$$

4.1.2   Weighted minimum norm estimates.

A certain disadvantage of MNE solutions is that MNE favors the superficial sources located close to the electrodes, which may result in distorted and unrealistic images. This negative effect is reduced in weighted minimum norm estimates (WMNE), which finds the solution through the *weighted* minimization of the optimization vector $\mathbf{D}$ (Hämäläinen and Ilmoniemi 1994). For this purpose WMNE utilizes a matrix of source weights $\mathbf{W} \in \mathbb{R}^{3n \times 3n}$, which implements the location-dependent penalty for high-energy sources. Typically the weight matrix is defined as diagonal matrix with the i-th element on the main diagonal obtained by calculating the l-2 norm of the i-th column of the lead field:

$$\mathbf{L} = [\mathbf{l}_1, \mathbf{l}_2, \ldots, \mathbf{l}_{3n}];$$
$$w_{ij} = \begin{cases} \|\mathbf{l}_i\|_2 \ , & i = j \\ 0 \ , & i \neq j \end{cases} \qquad (4.6)$$

After introducing the source weights the cost function to be minimized takes the following form:

$$F_{WMNE}(\mathbf{D}) = \|\mathbf{M} - \mathbf{L}\mathbf{D}\|_2 + \lambda\|\mathbf{W}\mathbf{D}\|_2 \ . \qquad (4.7)$$

Derived in a way similar to MNE, the WMNE solution vector is calculated as follows:

$$\hat{\mathbf{D}}_{WMNE} = (\mathbf{W}^T\mathbf{W})^{-1}\mathbf{L}^T(\mathbf{L}(\mathbf{W}^T\mathbf{W})^{-1}\mathbf{L}^T + \lambda\mathbf{I}_m)^{-1}\mathbf{M} = \mathbf{G}_{WMNE}\mathbf{M} \ .$$
$$(4.8)$$

4.1.3 Low resolution electrical tomography.

Introduced in 1994 by Pascual-Marqui low resolution electrical tomography (LORETA) aims to find a distributed inverse solution under constraints assuming the simultaneous and synchronous activation of neighboring cortical patches (Pascual-Marqui, Michel, and Lehmann 1994). In LORETA the current density at any cortical location is assumed to be maximally similar to the average current density in the adjacent area. This leads to the inverse solutions with low spatial resolution, but excellent temporal resolution of reconstructed source data.

From computational perspective such solutions are obtained by penalizing the highly focal current topographies. Besides the source depth compensation, LORETA utilizes the discrete Laplacian operator $\mathbf{B}$ in the cost function formulation:

$$F_{LORETA}(\mathbf{D}) = \|\mathbf{M} - \mathbf{LD}\|_2 + \lambda\|\mathbf{BWD}\|_2 \ , \tag{4.9}$$

where $\mathbf{W}$ is a source depth compensation matrix calculated in the same manner as described in (4.6). Discrete Laplacian operator $\mathbf{B}$ is defined with respect to the source grid configuration. Let $\mathbf{Z} = \mathbf{WD} = (z_1, z_2, z_3, \ldots, z_{3n})^T$ be the weighted instantaneous current density vector and let $\mathbf{BZ} = (l_1, l_2, l_3, \ldots, l_{3n})$ be the corresponding Laplacian. Then for a regular 3d grid of source locations with constant inter-node distance d and a maximum of 6 neighbors for each point the matrix $\mathbf{B}$ is defined in a way so that:

$$l_i = \frac{1}{d^2}(6z_i - \sum_{p=1}^{6} z_p) \ . \tag{4.10}$$

The calculation of Laplace operator $\mathbf{B}$ by 4.10 is simple due to the constant inter-node distance d. If the realistic head model is used, then the source model is generally represented by the irregular cloud of points spanning the brain surface. In this case the calculation of discrete Laplacian must take into account such an irregularity and, besides, must be adaptive to the local mesh size. The methodology of discrete mesh Laplacian calculation with Euclidean and geodesic distances is detailed in (Belkin, Sun, and Wang 2008; Thangudu 2009).

Similarly to WMNE after all the prerequisites are defined the LORETA solution is found as:

$$\hat{\mathbf{D}}_{LORETA} = (\mathbf{W}\mathbf{B}^T\mathbf{B}\mathbf{W})^{-1}\mathbf{L}^T(\mathbf{L}(\mathbf{W}\mathbf{B}^T\mathbf{B}\mathbf{W})^{-1}\mathbf{L}^T + \lambda\mathbf{I}_m)^{-1}\mathbf{M} =$$
$$= \mathbf{G}_{LORETA}\mathbf{M} \ .$$
$$(4.11)$$

4.1.4 Local autoregressive average.

Local autoregressive average (LAURA), introduced in 2004 (Peralta Menendez et al. 2004), finds a unique distributed inverse solution based on the biophysical constraints that express the reciprocal dependence of adjacent cortical patches. As discussed in (Michel et al. 2004), the source reconstruction through norm minimization is based on assumptions that are often purely mathematical, i.e., indirectly linked to the actual physical nature of brain currents. LAURA aims to incorporate biophysical laws in the norm minimization approach.

By definition in (Peralta Menendez et al. 2004) LAURA is based on minimization of the following cost function:

$$F_{LAURA}(\mathbf{D}) = (\mathbf{M} - \mathbf{L}\mathbf{D})^T\mathbf{W}_{sens}(\mathbf{M} - \mathbf{L}\mathbf{D}) + \lambda\mathbf{D}^T\mathbf{W}_{source}\mathbf{D} \ , \quad (4.12)$$

where $\mathbf{W}_{sens}$ and $\mathbf{W}_{source}$ are the metrics in sensor and source spaces respectively, used for regularization. $\mathbf{W}_{sens}$ can be chosen as a covariance matrix of an input EEG segment, or alternatively an identity matrix. $\mathbf{W}_{source}$ is calculated in the following way:

1. Let $\mathcal{V}_i$ represent the vicinity of each source location defined as a hexahedron centered at the point and containing a maximum of $\mathcal{V}_{max} = 26$ neighbors.

2. Then let N_k denote the number of neighbors of k-th source and let d_{ik} be the Euclidean distance between points k and i.

3. Obtain matrix $\mathbf{A}$ using $e_i = 3$ for vector fields (for source models with unrestricted orientations):

$$A_{ii} = \frac{\mathcal{V}_{max}}{N_i} \sum_{k \in \mathcal{V}_i} d_{ki}^{-e_i}$$
$$A_{ki} = A_{ik} = -d_{ki}^{-e_i} \ . \qquad (4.13)$$

4. Finally, weight matrix $\mathbf{W}_{source}$ is defined as:

$$\mathbf{P} = \mathbf{W}_m \mathbf{A} \otimes \mathbf{I}_3$$
$$\mathbf{W}_{source} = \mathbf{P}^T \mathbf{P} \,, \tag{4.14}$$

where $\mathbf{I}_3$ denotes the 3×3 identity matrix, $\otimes$ denotes the Kronecker product and $\mathbf{W}_m$ is a diagonal source depth compensation matrix with diagonal elements calculated as a norm of the three corresponding columns of lead field matrix $\mathbf{L}$.

Finally, LAURA estimate inverse solution is calculated as follows:

$$\hat{\mathbf{D}}_{LAURA} = (\mathbf{W}_j)^{-1} \mathbf{L}^T (\mathbf{L}(\mathbf{W}_j)^{-1} \mathbf{L}^T + \lambda \mathbf{I}_m)^{-1} \mathbf{M} =$$
$$= \mathbf{G}_{LAURA} \mathbf{M} \,. \tag{4.15}$$

4.1.5 Least absolute shrinkage and selection operator.

In the previous sections we have described several inverse solutions which correspond to Tikhonov regularization, in other words, they simultaneously minimize the residual error and the regularization term, which all together can be expressed as a minimization of cost function:

$$F(\mathbf{D}) = \|\mathbf{M} - \mathbf{L}\mathbf{D}\|_2 + \lambda \|\Gamma \mathbf{D}\|_2 \,, \tag{4.16}$$

where Γ represents some generalized regularization matrix. While l-2 norm regularization is an effective way of achieving numerically stable solutions, it does not encourage sparsity. As a result the associated source reconstruction methods produce results with non-zero values at all locations.

This issue can be addressed by applying the least absolute shrinkage and selection operator (LASSO) (Tibshirani 1996), which also corresponds to penalized least squares, however does not fit into Tikhonov regularization framework. Intuitively sparse solutions with minimal number of non-zero elements can be achieved by introducing the regularization term $\lambda \|\mathbf{D}\|_0$ employing the l-0 norm $\|\cdot\|_0$, which returns the number of non-zero entries in a vector or matrix. Unfortunately the numerical implementation of l-0 norm minimization is

extremely computationally expensive, since it makes the cost function non-convex and, hence, incompatible with optimization algorithms such as gradient descent. However, it is possible to obtain an approximate solution through *convex relaxation* of l-0 minimization problem, i.e., use l-1 norm instead (Lin, Foster, and Ungar 2010). This idea is behind the least absolute shrinkage and selection operator (LASSO), which finds a solution through minimization of the following convex cost function:

$$F(\mathbf{D})_{LASSO} = \|\mathbf{M} - \mathbf{LD}\|_2 + \lambda\|\mathbf{D}\|_1 \ . \qquad (4.17)$$

Since the cost function is convex, it is possible to find its unique global minimum by applying convex optimization solvers, for example, SeDuMi (Sturm 1999) or SDPT$_3$ (Toh, Todd, and Tütüncü 1999; Tütüncü, Toh, and Todd 2003). While these generalized solvers are capable of finding a unique stable solution, the optimization process is relatively slow and typically not applicable to real-time source localization applications. However, it is worth noting that there exists a number of promising approximate but fast algorithms for l-1 norm minimization, such as Orthogonal Matching Pursuit (OMP) (Davis, Mallat, and Avellaneda 1997), Least Angle Regression (LARS) (Efron et al. 2004) or Polytope Faces Pursuit (PFP) (Plumbley 2006).

4.1.6 Elastic net.

LASSO method for source localization provides highly focal solutions with exponential spatial field priors. It is considered that such results are not realistic from biophysical perspective, since brain is a conductive media and, hence, a strong local current must be accompanied by correlated adjacent sources, due to the secondary current effects. Elastic net (E-NET) expresses this assumption by adding a quadratic regularization term to the LASSO cost function:

$$F(\mathbf{D})_{LASSO} = \|\mathbf{M} - \mathbf{LD}\|_2 + \lambda_{sparse}\|\mathbf{D}\|_1 + \lambda_{smooth}\|\mathbf{D}\|_2 \ , \qquad (4.18)$$

where λ_{sparse} and λ_{smooth} are regularization parameters defining the relative weight of sparse l-1 norm and smooth l-2 norm penalties

respectively. Simultaneous selection of two regularization parameters is computationally more complex, but on the other hand it provides for greater flexibility in terms of sparsity profile definition. The cost function (4.18) is convex and the minimum can be found using generic convex optimization solvers such as CVX or specialized algorithms such as `lasso` function in Matlab.

4.1.7 Summary of the employed inverse solutions.

Table 4.1 lists a number of inverse solutions based on a flexible framework of penalized least squares. All of the methods listed in the table except for LASSO and E-NET can be implemented as a linear matrix operator, which makes them easily applicable to real-time source analysis. On the other hand, as will be shown in the next sections LASSO and E-NET are capable of more accurate and focal reconstruction of sources, which makes them advantageous in source analysis scenarios with no real-time constraints.

TABLE 4.1: Names, equations and references of inverse solutions.

Name	Equation	Reference
MNE	$\hat{\mathbf{D}}_{\text{MNE}} = \arg\min_{\mathbf{D}} \|\mathbf{M} - \mathbf{LD}\|_2 + \lambda\|\mathbf{D}\|_2$	(Baillet 1998; Grech et al. 2008)
WMNE	$\hat{\mathbf{D}}_{\text{WMNE}} = \arg\min_{\mathbf{D}} \|\mathbf{M} - \mathbf{LD}\|_2 + \lambda\|\mathbf{WD}\|_2$	(Hämäläinen and Ilmoniemi 1994)
LORETA	$\hat{\mathbf{D}}_{\text{LORETA}} = \arg\min_{\mathbf{D}} \|\mathbf{M} - \mathbf{LD}\|_2 + \lambda\|\mathbf{BWD}\|_2$	(Pascual-Marqui, Michel, and Lehmann 1994)
LAURA	$\hat{\mathbf{D}}_{\text{LAURA}} = \arg\min_{\mathbf{D}} \|\mathbf{M} - \mathbf{W}_{sens}\mathbf{LD}\|_2 + \lambda\|\mathbf{W}_{source}\mathbf{D}\|_2$	(Peralta Menendez et al. 2004)
LASSO	$\hat{\mathbf{D}}_{\text{LASSO}} = \arg\min_{\mathbf{D}} \|\mathbf{M} - \mathbf{LD}\|_2 + \lambda\|\mathbf{D}\|_1$	(Tibshirani 1996)
E-NET	$\hat{\mathbf{D}}_{\text{E-NET}} = \arg\min_{\mathbf{D}} \|\mathbf{M} - \mathbf{LD}\|_2 + \lambda_{sparse}\|\mathbf{D}\|_1 + \lambda_{smooth}\|\mathbf{D}\|_2$	(Zou and Hastie 2005)

$\mathbf{W}$ - is the source depth compensation matrix

$\mathbf{B}$ - Laplacian operator

4.2   Source localization of simulated data.

In order to characterize the capabilities and properties of source reconstruction as of EEG analysis tool it is necessary to demonstrate its performance on simulated data. In the following sections the simulation protocol will be described, then the point-spread function of an EEG source imaging system and the source separation properties will be demonstrated.

4.2.1   Simulation protocol.

Prior to source reconstruction it is necessary to define the forward model, i.e., prepare the head geometry, EEG sensor configuration, source grid and obtain the lead field matrix. In the following examples we utilize the head geometry provided by ICBM 152 head atlas, which was obtained by non-linear averaging of 152 adult anatomical MRI scans (Collins et al. 1999; Fonov et al. 2009; Fonov et al. 2011). In order to conform to the BEM requirements, the head geometry was defined as a set of boundary surfaces including skin surface, outer skull, inner skull and a detailed cortical surface. The original triangular cortical surface mesh provided with the atlas is comprised by 15002 vertices and 29984 faces. In order to meet the computational requirements this mesh was downsampled using iso2mesh method (Fang and Boas 2009) yielding a total of 4504 vertices and 9000 faces. Then the source grid was defined at the vertices of the cortical surface with three dipoles oriented along the Cartesian axes set at each point in order to allow for unrestricted source orientations. The EEG electrode locations corresponding to g.tec's g.Nautilus EEG headset (http://www.gtec.at/Products/Hardware-and-Accessories/g.Nautilus-Specs-Features) was selected from the standard extended 10-5 electrode configuration provided in Brainstorm suite for Matlab (Tadel et al. 2011).
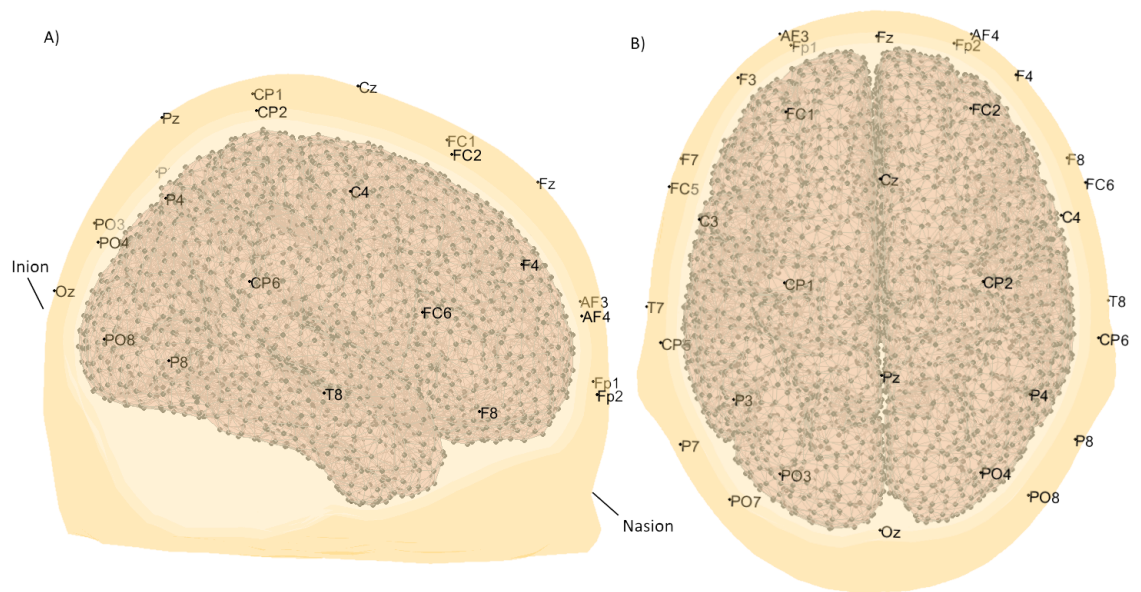
FIGURE 4.1: Visualization of forward head model used in simulations. EEG sensor locations are marked by channel labels and source locations on the cortical surface are represented by black dots. A) Side view from the right. B) Top down view.

After the necessary prerequisites are defined the symmetric BEM (Clerc et al. 2010) implementation from OpenMEEG software (Kybic et al. 2005; Gramfort et al. 2010) was used to obtain the volume conduction model and the resulting lead field matrix. Figure 4.1 shows the visualization of the described forward model including four boundary surfaces, source locations marked by black dots and labeled EEG electrode montage.

4.2.2 Point-spread function.

A combination of forward model and an inverse solver comprises an EEG imaging system. One way to characterize such a system is to estimate its point-spead function, which can be defined as an image produced in response to a single unit active source, in other words, as a spatial impulse response of a system. In this section a common simulation scenario is used in order to demonstrate the capabilities of various inverse solvers.

In order to estimate the point-spread function it is first necessary to define the simulated sensor measurements. For this purpose
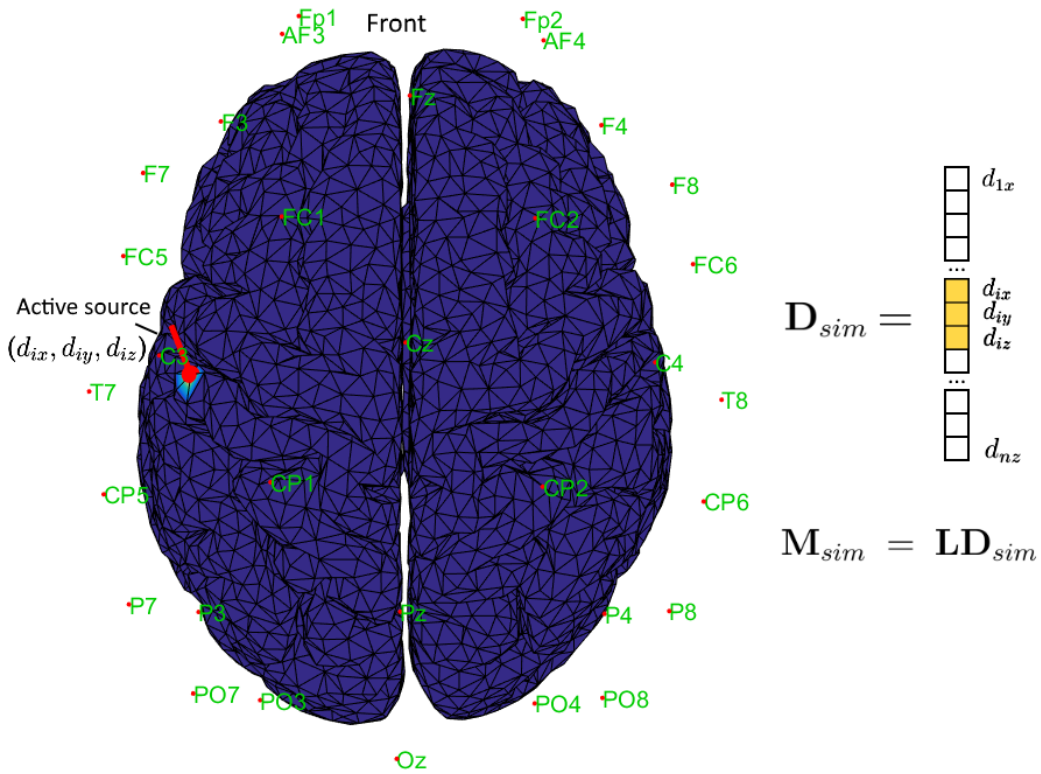
FIGURE 4.2: Visualization of the simulation protocol for instantaneous source localization including triangulated ICBM 152 cortical surface, a single simulated source with shown orientation and EEG sensor locations (in green font) for reference.

we defined a simulated source vector $\mathbf{D}_{sim} \in \mathbb{R}^{3n \times 1}$ with zero values at all locations except for a single active point i. The Cartesian components (d_{ix}, d_{iy}, d_{iz}) of the simulated source were scaled with respect to the orientation of vertex normal at this point. Then, according to (3.16), a vector of simulated sensor measurements $\mathbf{M}_{sim} = \mathbf{L}\mathbf{D}_{sim}$ was calculated. The visualization of this simulation scenario is shown in figure (4.2).

The power distribution topographies obtained by several different inverse solvers for the described simulation scenario are given in figure 4.3. As was discussed before, each source location is modeled by a set of three dipoles oriented along the Cartesian axes. The power estimate at location k was calculated as Euclidean norm of (d_{kx}, d_{ky}, d_{kz}). Inverse solutions for MNE, WMNE, LORETA and LAURA were calculated using the methods given in sections (4.1.1)-(4.1.4). For these solvers the regularization parameters λ from the range of
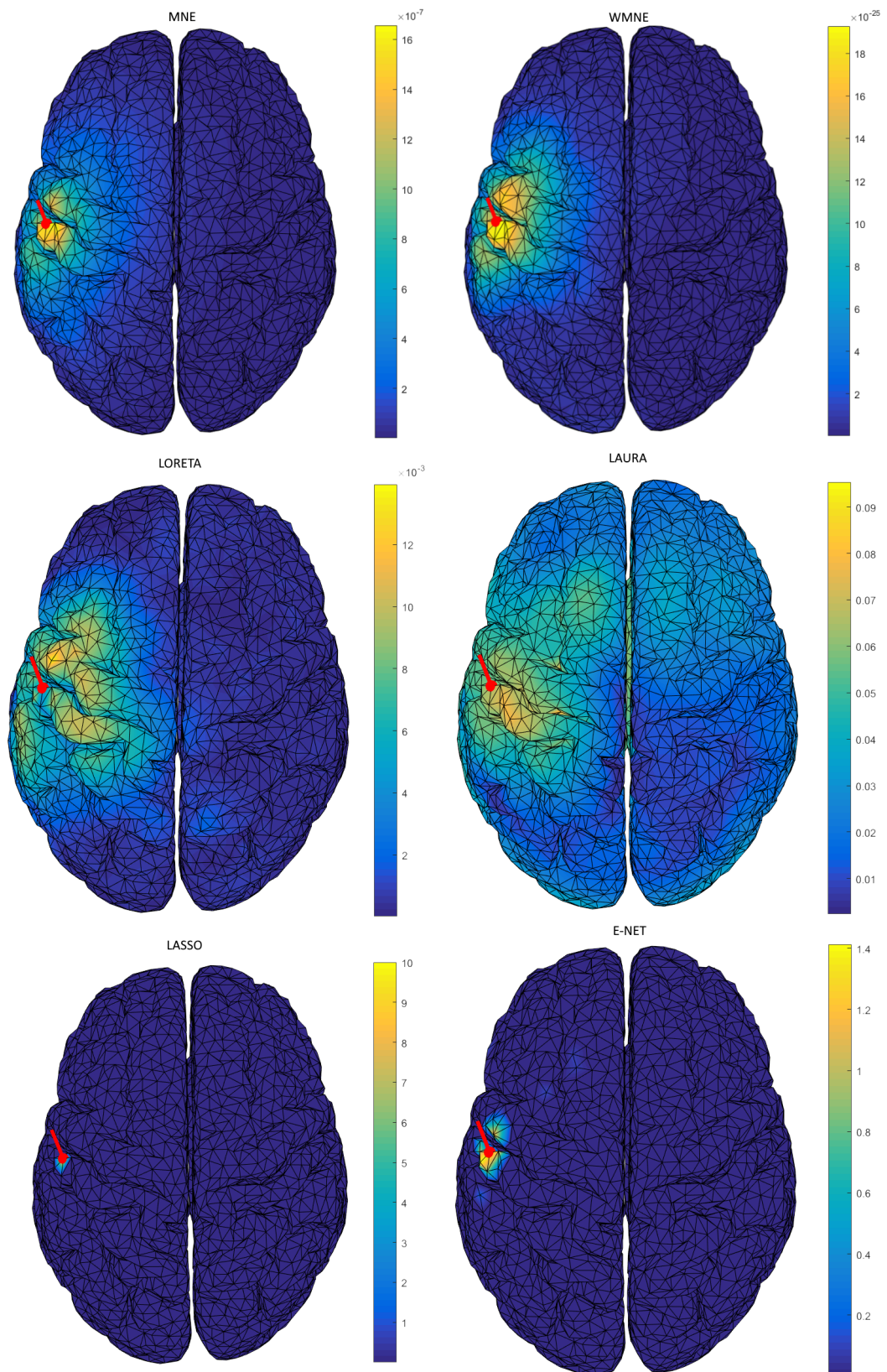
FIGURE 4.3: Power distribution topographies of instantaneous source localization simulation results obtained with different inverse solvers.

$[10^{-20}, \ 10^{10}]$ were selected according to the L-curve generalized cross-validation (GCV) procedure (Golub, Heath, and Wahba 1979; Hansen 1999; Grech et al. 2008) yielding the most focal solutions possible for these methods.

Sparse solutions of LASSO and E-NET were obtained using the CVX package for Matlab (Grant, Boyd, and Ye 2008; Grant and Boyd 2008). For these methods the GCV selection procedure is not applicable, therefore, regularization parameters were selected heuristically from the range of $[10^{-20}, \ 10^{10}]$ with the aim of minimizing the spatial spread of electrically active area, which was calculated as a number of vertices at which the power is more than half of the maximal power within the whole solution (minimizing FWHM of the solution).

As it could be seen from the results, each source localization method has its own limitations and characteristic artifacts. In general, inverse solutions based on *l*-2 norm minimization produce more distributed, 'blurry', topographies with Gaussian spatial distribution of source components and negligible calculation time (less than 0.001 seconds in our settings), which makes them suitable for real-time applications. On the contrary, sparse source localization methods, which employ *l*-1 norm minimization, yield very focal results with exponential spatial priors and capabilities for exact reconstruction of sources in absence of noise. However, the estimation of such sparse solutions is computationally complex, typically taking >7 seconds per time sample, which currently makes it inapplicable to real-time applications.

4.2.3   Source reconstruction in the presence of noise.

In the previous section a number of inverse solutions were characterized with respect to their point-spread function, i.e. imaging system's response to a single activation. These results were obtained assuming the ideal EEG with no embedded noise. However, in a practical source analysis scenario the given EEG segment is generally contaminated by noise and artifacts, which may largely affect the produced source estimates. In this section the effect of noise on
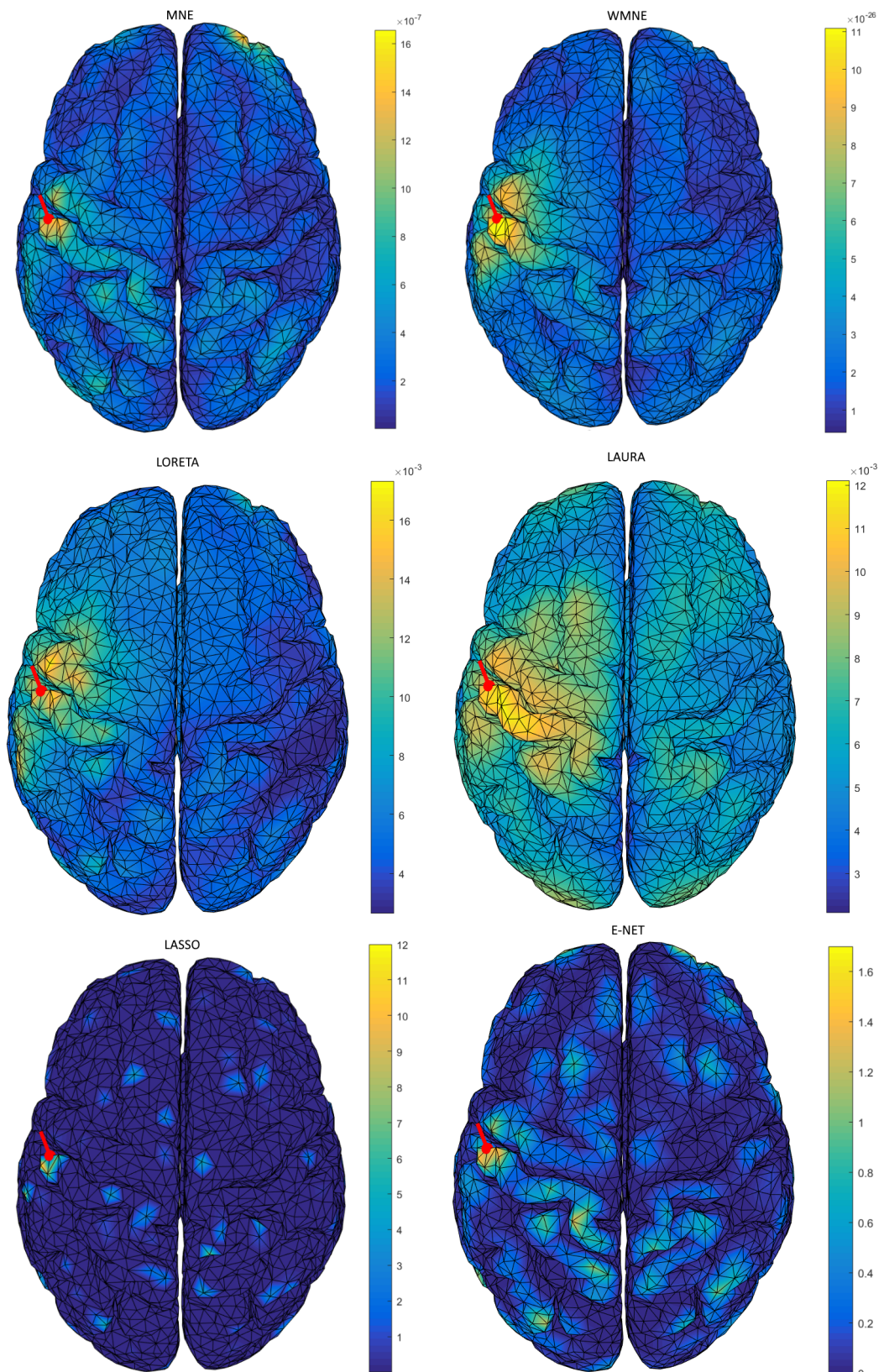
FIGURE 4.4: Power distribution topographies of sources reconstructed from simulated noisy EEG using different inverse solvers.

source reconstruction is demonstrated on a set of inverse solutions described earlier in this chapter.

Prior to source reconstruction it is necessary to define the simulated EEG segment for the same forward model as described in 4.2.1. For this purpose it is required to define a continuous simulated source matrix $\mathbf{D}_{sim} \in \mathbb{R}^{3n \times q}$ varying over q time samples with zero values at all locations except for a single active point i. At this vertex a sinusoidal component $d_i = \sin(2\pi ft)$ was set with $t \in [1 \dots 200]$ and frequency $f = 10$ Hz. Cartesian components (d_{ix}, d_{iy}, d_{iz}) of the simulated source were then scaled with respect to the orientation of vertex normal at this location. Then, according to (3.16), a block of simulated sensor measurements was obtained as $\mathbf{M}_{sim} = \mathbf{L}\mathbf{D}_{sim}$. Next, white gaussian noise was added to the simulated EEG data using the `awgn` function in Matlab to produce a signal with SNR of -10 dB.

The power distribution topographies obtained by different inverse solvers for the described simulation scenario are given in figure 4.4. These results demonstrate that linear inverse solvers such as WMNE, LORETA and LAURA that generally produce more distributed "blurry" results are less affected by noise. On the other hand, sparse solutions (LASSO and E-NET) were largely affected by noise. As can be seen from the results, these solvers tend to explain the spatially distributed noise through a small number of focally active points, which contradicts the physiological expectations. Therefore, these methods are applicable in analysis scenarios where the signal of interest is strong compared to noise, for example localization of an ERP waveform obtained by averaging hundreds of observations or localization of SSVEP effect.

4.2.4   Spatial component decorrelation.

One of the common disadvantages of EEG is high degree of cross-electrode coupling. Due to the volume conduction effects, a strong electrical activity at any cortical region is observable at all available EEG sensors. In this context source reconstruction is beneficial, since it can effectively reduce the coupling effects and represent the EEG

recording segment as a superposition of *spatially independent* components. In this section we present a simulation scenario that demonstrates such useful properties of source localization.

In order to demonstrate the separation capabilities of source reconstruction it is first necessary to define the simulated sensor measurements within the same forward model as described in 4.2.1. For this purpose it is required to define a continuous simulated source matrix $\mathbf{D}_{sim} \in \mathbb{R}^{3n \times q}$ varying over q time samples with zero values at all locations except for three active points i, j and k. At each active vertex a sinusoidal component $\sin(2\pi ft + \phi)$ was set with $t \in [1 \dots q]$, individual frequencies f_i, f_j, f_k and phases ϕ_i, ϕ_j, ϕ_k. Then, using the definition in (3.16) a matrix of simulated sensor measurements $\mathbf{M}_{sim} = \mathbf{L}\mathbf{D}_{sim}$ was calculated. With $q = 1500$ $\mathbf{M}_{sim}$ represents 3 seconds of EEG, recorded with sampling frequency of 500 Hz. Visualization of this simulation scenario with sources i, j and k and their
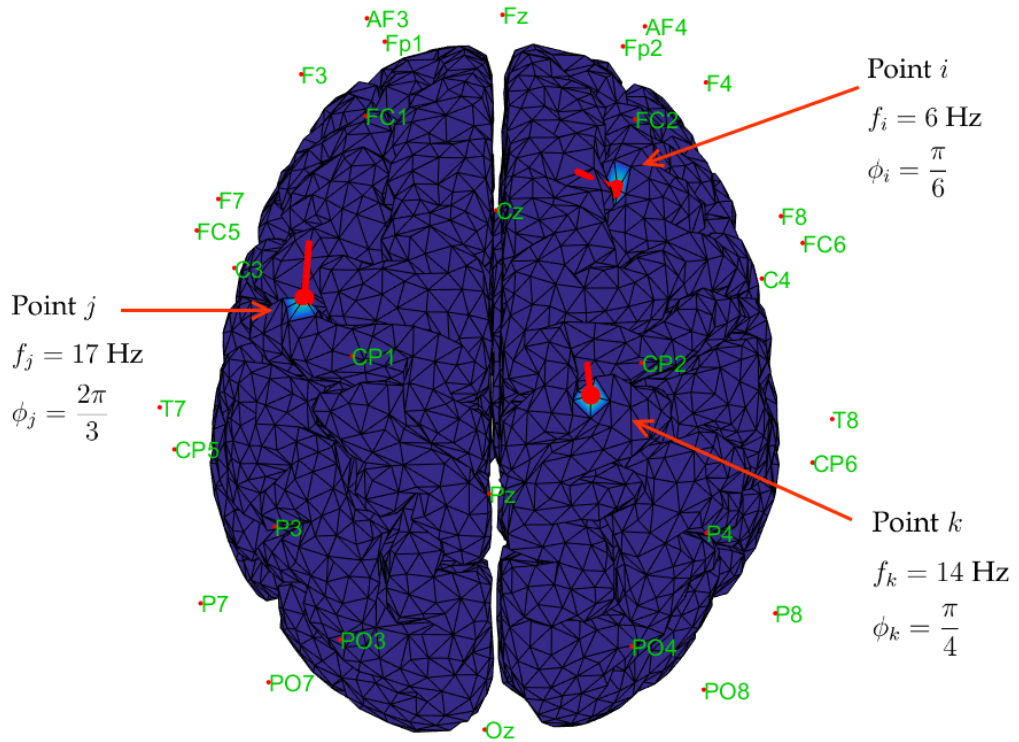
FIGURE 4.5: Visualization of the simulation protocol for continuous source localization including triangulated ICBM 152 cortical surface, EEG sensor locations (in green font) and simulated sources i, j, k with shown orientations and simulated signal parameters.
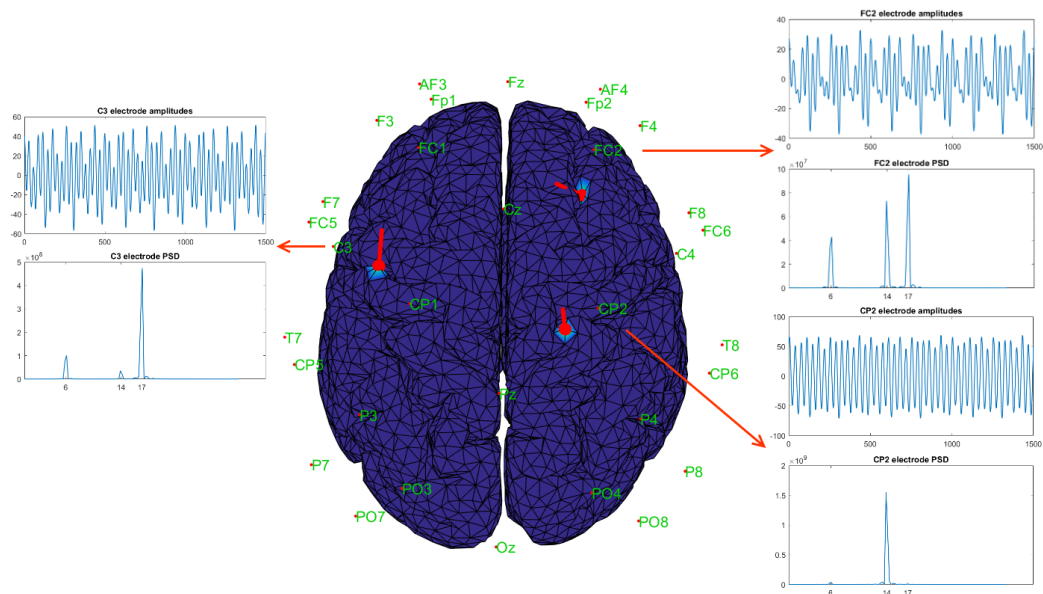
FIGURE 4.6: Visualization of continuous simulated EEG data at channels closest to simulated active points. There is an evident mixture of simulated frequency components at all presented channels, especially at channel FC2.

parameters are illustrated in figure 4.5. Figure 4.5 shows the mixture of simulated frequency components at sensors closest to the active sources.

Next, WMNE linear inverse operator was obtained for the given forward model and regularization parameter $\lambda = 0.01$ (see section 4.1.2). Matrix of continuous source components $\hat{\mathbf{D}}$ was obtained according to equation (4.2).

The simulation results, illustrated in figure 4.7, demonstrate two important benefits of source reconstruction. First, this type of processing is capable of isolating the signal components on the basis of their spatial origins. As shown in figure 4.6, each channel of the original simulated data $\mathbf{M}_{sim}$ contains a mixture of all active frequency components, especially at channel FC2. In this simulation scenario the WMNE source localization has achieved evident, although imperfect, reconstruction of the simulated frequency components.

Secondly, source reconstruction greatly expands the dimensionality of data - the original simulated EEG signal $\mathbf{M}_{sim} \in \mathbb{R}^{32 \times 1500}$ is defined over 32 variables, while the inverse solution $\hat{\mathbf{D}} \in \mathbb{R}^{13512 \times 1500}$
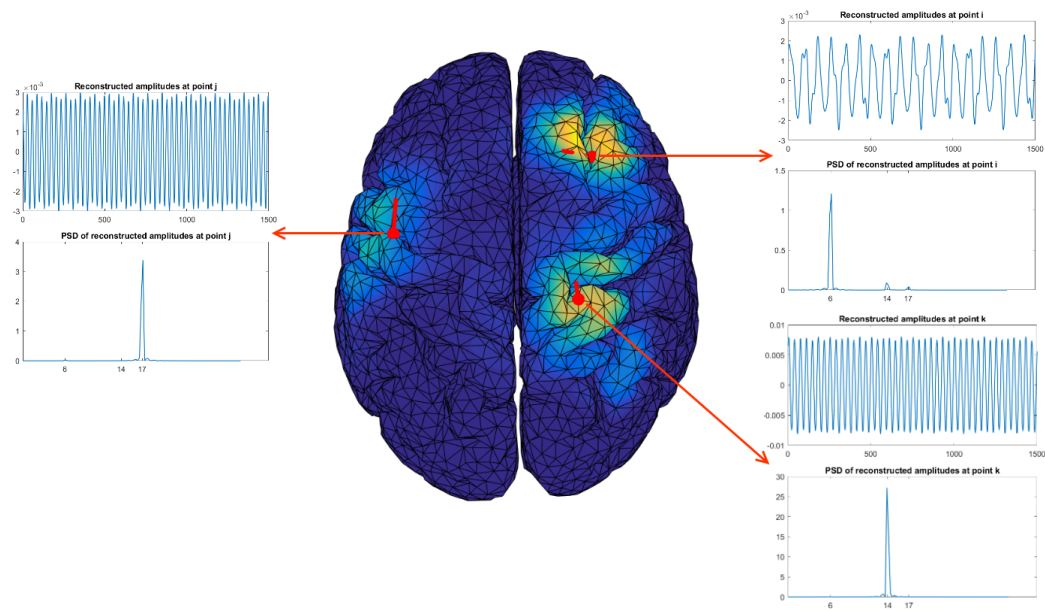
FIGURE 4.7: Results of source reconstruction on the simulated data. The topography of variance distribution is shown in color over the cortical surface. Graphs of reconstructed amplitudes at the original active locations and corresponding power spectral densities demonstrate the capabilities for source separation.

represents each time sample by 13512 variables defined over 4504 locations. Considering that each of these variables has individually allocated spatial properties, such a dimensionality expansion provides for more accurate signal component selection and spatial filter design, which in this case also corresponds to region-of-interest (ROI) selection. Considering the spatial component segregation, source reconstruction and subsequent ROI extraction achieves the partial cancellation of noise and artifact energy, i.e., improves the SNR of signal of interest and alleviates the negative effects of muscular artifacts.

4.3 Conclusion.

This chapter was dedicated to the inverse problem of EEG source localization, which is solved to obtain estimates of cortical currents for a given block of EEG data and a forward head model. Following the general problem formulation a number of essential inverse

solutions was presented. A particular inverse solver is generally defined through a cost function which includes some specific optimization constraints representing various physiological assumptions. An inverse solution is then obtained by finding a minimum of such a function for a given EEG segment.

These methods for source reconstruction were then characterized in a number of simulations. Although the linear inverse solvers that can be implemented as a matrix operator (WMNE, LAURA, LORETA) have broader point-spread function, i.e. produce more spatially distributed solutions, they perform consistently in the presence of noise and have small computational requirements which makes them applicable for real-time signal processing. Besides, the capabilities of these source reconstruction techniques for electrode de-coupling were demonstrated in the simulation which involved demixing of spatially independent components.

On the other hand, sparse localization methods based on l-1 norm minimization (LASSO, E-NET) produce sharp, focal solutions and are capable of complete accurate reconstruction of sources in the ideal noiseless case. However, these solvers are computationally expensive, perform poorly in the presence of noise, and therefore, are generally not applicable to real-time EEG processing in BCIs, but are more suitable for exploratory analysis and visualizations.

Chapter 5

Source localization in motor imagery BCIs.

Previous chapters were dedicated to the overview of various aspects of BCI design and introduction to the area of EEG imaging. The use of source localization introduces an additional layer of complexity to the BCI design problem, as it relies on a large number of design parameters to be selected by the developer, such as the choice of head geometry, source grid definition, selection of regularization parameters for forward/inverse solutions and many others. Nevertheless, this signal processing tool provides for greater flexibility in spatial filter design, and besides, as shown in our simulations, source reconstruction and subsequent ROI extraction may significantly improve the SNR and therefore facilitate more reliable EEG classification. This chapter is dedicated to the analysis of SMR BCI feature extraction performance employing the novel extension of the CSP method in source space. Here the beneficial effect of source reconstruction will be demonstrated applied to the openly available dataset 2a from BCI competition IV (Brunner et al. 2008).

5.1 BCI feature extraction based on EEG source localization.

In the past few decades there have been a large number of proposed BCI design approaches focusing on feature extraction, classification or other aspects with more than 300 designs described only in (Mason et al. 2007; Nicolas-Alonso and Gomez-Gil 2012). Considering the wide variety of design choices, including the signal acquisition

systems, sensor montages, feature extraction, selection and classi-
fication methods, it becomes almost impossible to reproduce and,
thus, validate the reported results. This issue partially underlies
the idea of BCI competitions organized by the Universities of Berlin,
Graz, Freiburg and Washington over several years from 2001 to 2008.
Within these events the competing research groups were given a
single common dataset, designed with focus on a specific BCI de-
sign challenge, and a common evaluation protocol. Consequently,
classification accuracies or ITRs reported in publications using such
datasets can be directly compared. The following sections are dedi-
cated to the description of our proposed feature extraction method
employing source reconstruction and demonstration of its perfor-
mance using a dataset from BCI competition IV.

5.1.1   EEG dataset.

The BCI Competition IV EEG dataset 2a (Brunner et al. 2008) consists
of EEG recordings of 4 types of mental tasks, namely left-hand, right-
hand, feet and tongue imaginary movement, to which will further be
referred to as data of class 1, class 2, class 3 and class 4 respectively.
The motor imagery signals from 9 healthy adult subjects with little
or no previous BCI experience were recorded over two sessions, one
for classifier training purposes and one for evaluation. Each session
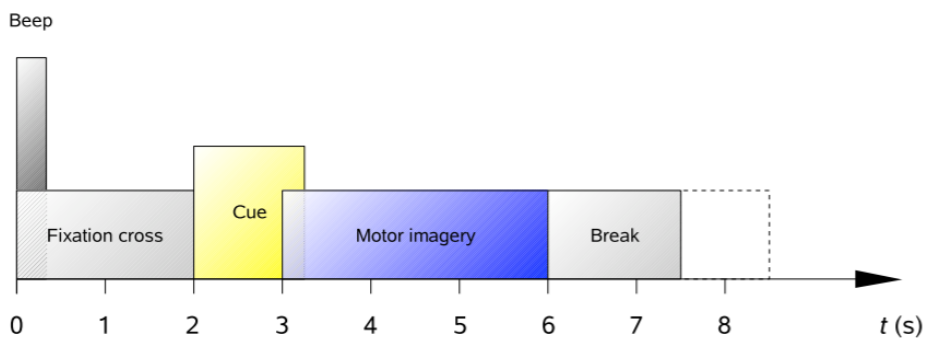
FIGURE 5.1: Timing scheme of the recording
paradigm. Each trial consists of 2 second long prepara-
tion interval and 3-4 seconds of mental task execution
following the visual cue being displayed to the subject.
Image from the original dataset description (Brunner
et al. 2008).

consisted of $N_{trl} = 288$ trials, each structured in a way described in figure 5.1, and recorded by $N_{ch} = 22$ gel EEG sensors with 250 Hz sampling rate and a single common reference at left mastoid.

5.1.2 Overview of the signal processing sequence.

At the actual BCI competition the design that achieved the highest classification reliability was based on the filter bank common spatial patterns (FBCSP) feature extraction approach (Tangermann et al. 2012). As shown in (Pfurtscheller et al. 2006), characteristic frequency of ERD/ERS varies greatly between different motor imagery tasks and the subjects performing them. In addition, untrained BCI users often show a certain disconnect between the activity in mu and beta bands of EEG with ERD effects generally occurring more consistently in the mu band. These observations are taken into account in FBCSP feature extraction, which combines the capabilities of CSP for extraction of ERD/ERS effects of motor imagery with the subject-specific estimation of indicative frequency bands. FBCSP utilizes a set of bandpass filters to decompose the original data into a set of narrow band components. Within each individual band a feature
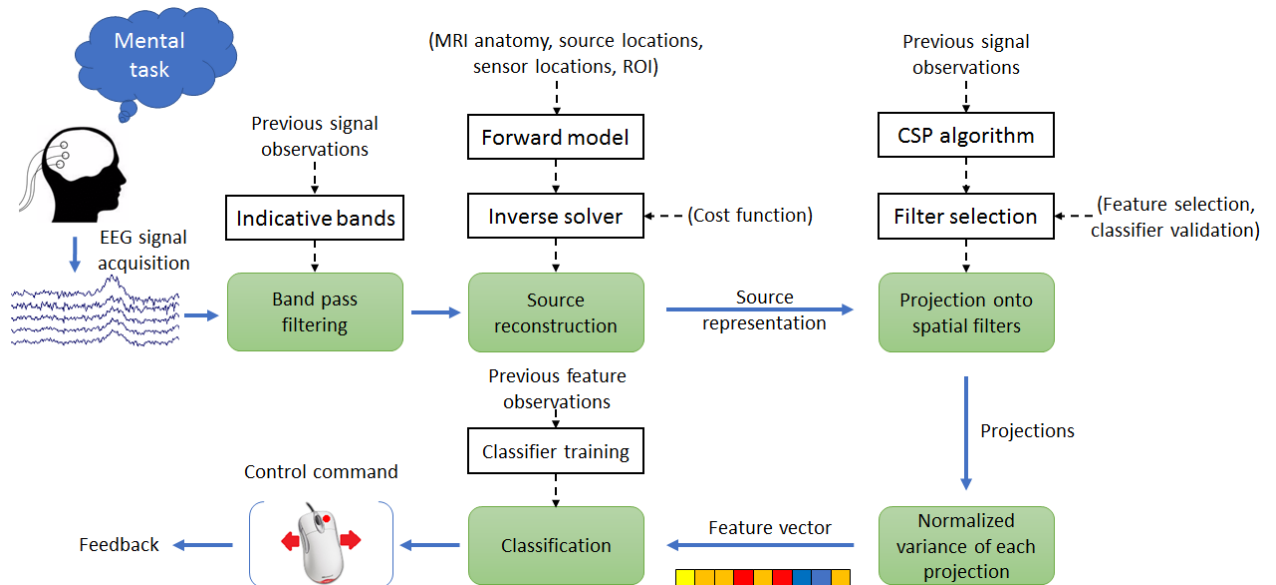
FIGURE 5.2: Schematic description of the proposed source CSP BCI.
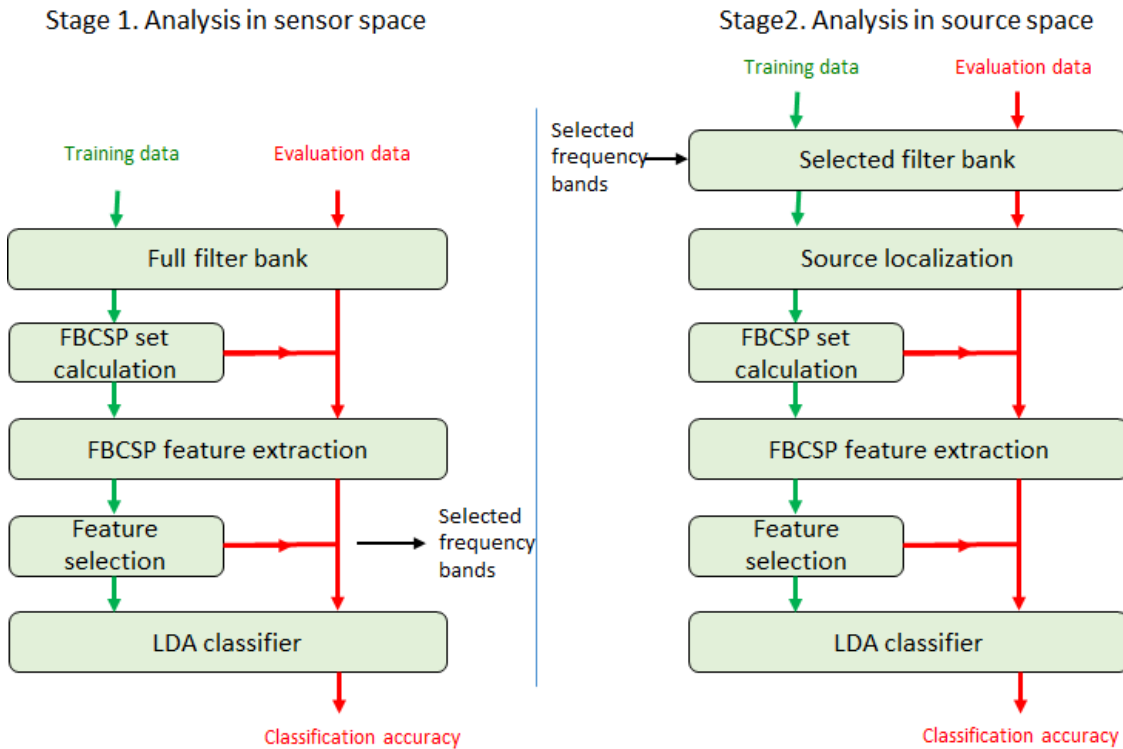
FIGURE 5.3: Two-stage signal processing scheme for motor imagery classification. At the first stage the indicative frequency bands are selected based on the sensor feature ranking and classifier evaluation procedure. At the second stage only a small number of bands is used for source reconstruction and subsequent feature extraction.

vector is extracted using the conventional CSP method. Feature vectors from separate bands are then concatenated and fed to feature selection and classifier training stages, where a small number of indicative features is selected from the whole set and used to fit a multiclass LDA classifier.

Considering the reported high efficiency of the FBCSP feature extraction method, it was used as a basis for our proposed signal processing scheme incorporating source reconstruction. Schematically the proposed BCI system is illustrated in figure 5.2 which lists the essential stages of signal processing including the data-driven estimation of indicative frequency bands, source reconstruction, data-driven calculation of CSP filters and finally classification.

From the design architecture perspective the source localization

step may be employed here in two different ways - prior to subband decomposition, or individually within each individual band after filtering. Although the latter approach provides better results it is extremely computationally expensive. For example, with the forward model described in 4.2.1 and a filter bank of 14 bands a set of narrow band covariance matrices from a single trial with single precision would take up $14 \times 13512 \times 13512 \times 4$ bytes = 9.5 Gb of RAM. Besides that, one of the aims of this analysis was to demonstrate the advantages of source reconstruction compared to conventional analysis in sensor space. Therefore, the EEG processing was performed in two separate stages (Figure 5.3). The aim of the first stage was to estimate the subject-specific bands of signal that are indicative of mental state by utilizing the metrics of CSP features from a large number of narrow bands. Based on these results a small number (2-3) of subbands was selected for each subject and at the second stage source reconstruction and ROI extraction were applied separately within individual bands. Alternatively, subband selection can be performed heuristically, based on, e.g., simple visual assessment of trial-averaged TFRs of different mental tasks. However, taking into account the large number of subjects in a dataset, the proposed two-stage scheme is significantly faster and also more autonomous, facilitating the data-driven estimation of design parameters. The following sections provide detailed descriptions of the elements in the proposed signal processing scheme.

5.1.3 Stage 1. Analysis in sensor space.

Signal preprocessing.

Generally, during EEG recording the trial timing structure is embedded into the data by the means of an auxiliary channel containing event triggers, marking the time of trial onset and the type of visual cue shown to the subject. Such markers embedded in dataset 2a were used to segment the continuous session recordings into a set of trials comprising 1 second of pre-stimulus intervals (before the cue was shown to the subject) and 3 seconds of mental task execution. The original EEG data was recorded with 250 Hz sampling frequency. Considering that the effects indicative of motor imagery type arise mainly in mu (7-13 Hz) and beta (16-31 Hz) bands of the EEG, and high the computational requirements of source analysis, the signal was downsampled to 100 Hz sampling rate giving a maximum EEG component frequency of 50 Hz.

Filter bank.

As explained earlier, FBCSP aims to find subject-specific frequency bands indicative of mental state and process them separately, which involves separating the original signal into a set of narrow-band components.
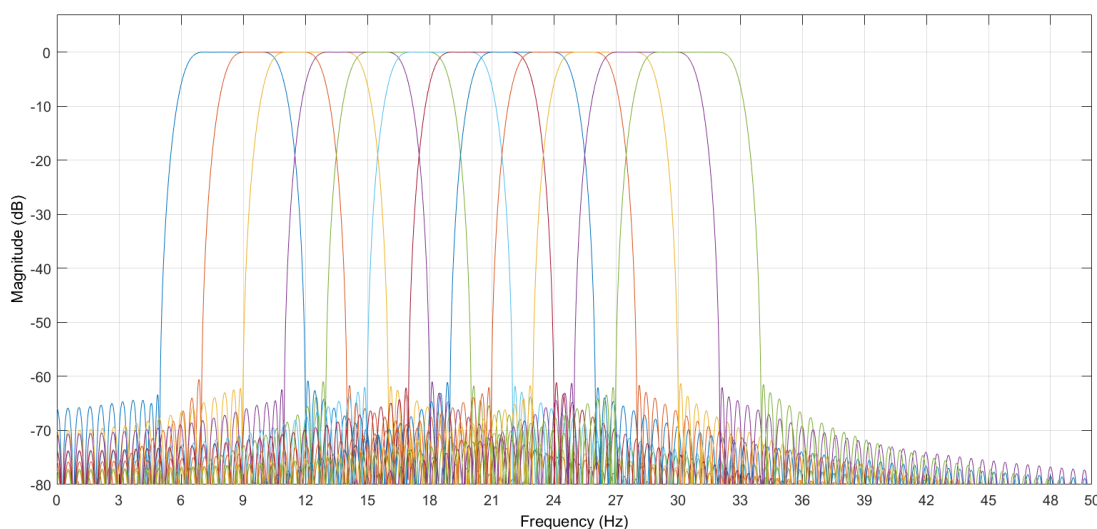
FIGURE 5.4: Magnitude response of the employed filter bank.

Such subband decomposition of each trial was achieved by applying a filter bank comprised of $N_f = 12$ bandpass FIR filters implemented using a Kaiser window method and spanning the 7-33 Hz frequency range. Each filter was designed with a 3 Hz pass band, 2 Hz transition width and a stop band attenuation of 60 dB. The magnitude response of the employed filter bank with individual filters denoted by color is shown in figure 5.4.

CSP estimation and feature extraction.

Next the subband data from each trial was used to estimate a set of CSP filters within the individual bands. The description of a two-class CSP method is given in section 2.2.3. While the conventional CSP is defined for two class discrimination problems, the dataset contains data from 4 different classes (types of mental tasks), therefore for each subject and within each subband the CSP problem was solved 4 times, contrasting every class of data separately in a one-vs-rest (OVR) manner. Within the i-th subband the most desirable spatial filter for a certain class, that maximizes the variance contrast with the remaining classes can be found as a vector that maximizes the following ratio:

$$\hat{\mathbf{w}}_{csp} = \underset{\mathbf{w}_{csp}}{\mathrm{argmax}} \; \frac{\mathbf{w}_{csp}\mathbf{C}^i_+\mathbf{w}^T_{csp}}{\mathbf{w}_{csp}\mathbf{C}^i_-\mathbf{w}^T_{csp}} \; , \qquad (5.1)$$

where $\mathbf{C}^i_+$ is the average covariance of the class being contrasted, obtained by averaging the covariances of a single type of motor imagery trials processed by i-th filter. $\mathbf{C}^i_-$ then denotes the average covariances of the remaining data classes. For example, when estimating the OVR CSP set for right hand motor imagery (class 2), $\mathbf{C}^i_+ = \mathbf{C}^i_{class\,2}$ and $\mathbf{C}^i_- = (\mathbf{C}^i_{class\,1} + \mathbf{C}^i_{class\,3} + \mathbf{C}^i_{class\,4})/3$. In practice the spatial filters within each frequency bin are calculated as eigenvectors of the following generalized eigenvalue problem:

$$\mathbf{C}^i_+\mathbf{W} = \mathbf{\Lambda}\mathbf{C}^i_-\mathbf{W} \; , \qquad (5.2)$$

with $\mathbf{W}$ denoting the matrix of eigenvectors and $\mathbf{\Lambda}$ representing a diagonal matrix with eigenvalues on the main diagonal. The eigenvector of problem (5.2) corresponding to the largest eigenvalue is the

spatial filter that maximizes the ratio in (5.1). Therefore, only two spatial filters corresponding to the largest eigenvalues were selected for each class of data, yielding a total of $N_{csp} = 8$ filters per frequency band. These filters were then combined in the matrix $\hat{\mathbf{W}}^i_{\mathbf{csp}} \in \mathbb{R}^{N_{csp} \times N_{ch}}$, which denotes the multiclass CSP set for i-th frequency bin. Next the feature vector $\mathbf{F}_{full}$ that combines the CSP features from all subbands of EEG observation $\mathbf{M}$ was formed in the following way:

$$\mathbf{Z}^i = \hat{\mathbf{W}}^i_{\mathbf{csp}}\mathbf{M}^i \ , \forall i \in [1 \ldots N_f]$$
$$f^i_j = \log\left(\frac{\text{var}(\mathbf{Z}^i_j)}{\sum_{p=1}^{N_{csp}} \text{var}(\mathbf{Z}_p)}\right) , \forall i \in [1 \ldots N_f], \forall j \in [1 \ldots N_{csp}]$$
$$\mathbf{f}^i = [f_1, f_2 \ .. \ f_{N_{csp}}] , \forall i \in [1 \ldots N_f] \tag{5.3}$$
$$\mathbf{F}_{full} = [\mathbf{f}^1, \mathbf{f}^2, \ldots, \mathbf{f}^{N_f}] ,$$

where $\mathbf{M}^i$ represents the i-th subband of signal observation $\mathbf{M}$ and $\mathbf{Z}^i_j$ denotes the j-th row of $\mathbf{Z}^i$, obtained as a 1D projection of $\mathbf{M}^i$ onto the j-th row of $\hat{\mathbf{W}}^i_{\mathbf{csp}}$. In other words, conventional CSP feature extraction was applied to each subband of trial $\mathbf{M}$ and the full feature vector $\mathbf{F}_{full}$ was obtained by concatenating features from all frequency bands. Considering that $N_f = 12$ and $N_{csp} = 8$ in our settings, this yields a total of 96 predictor variables representing a single observation of motor imagery. For each subject in the dataset this process was repeated over all given EEG trials, resulting in 288 feature vectors per subject.

In order to demonstrate the principle of CSP feature extraction, the visualization of CSP filters and corresponding projections for two conditions are shown: left-hand and right-hand motor imagery. Figure 5.5 A)-B) contains the weight distribution topographies of the most desirable CSP filters $\mathbf{w}_{LH}$ and $\mathbf{w}_{RH}$ for left-hand and right-hand imagery respectively, displayed in color over the given electrode montage. These filters were obtained using the data for subject 8 in the dataset and a single subband of 9-12 Hz. The areas of high weight magnitude point to the electrodes with large variance difference between the two conditions. For example, the variance at channel CP4 is significantly lower during the left-hand imagery compared to other mental tasks, therefore channel CP4 has a
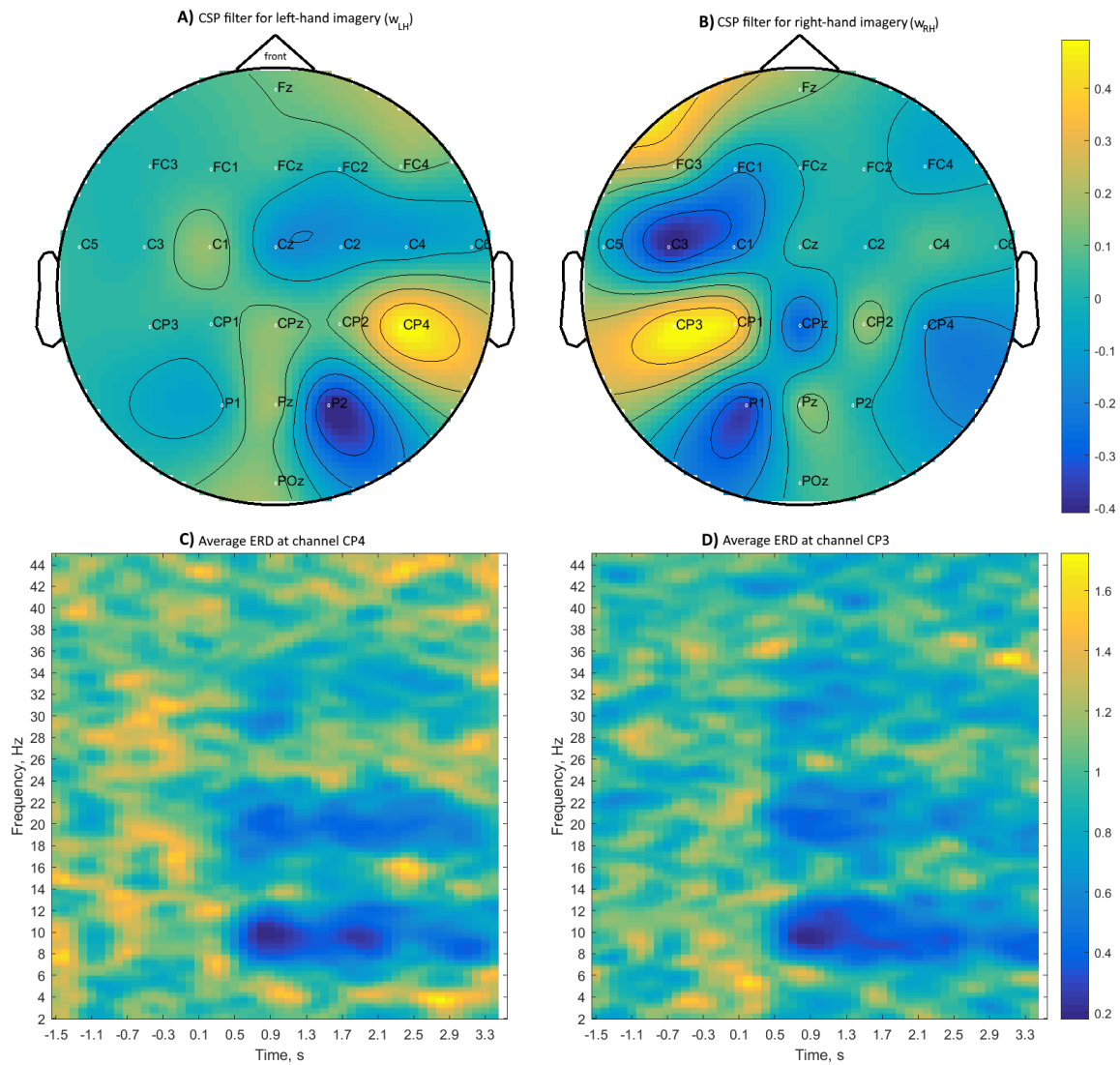
FIGURE 5.5: CSP filters for the left-hand and right-hand motor imagery tasks and characteristic ERD effects. A)-B) Spatial filter weight coefficients shown in color over the given EEG montage. C)-D) Average time-frequency maps of the effects that filters $\mathbf{w}_{LH}$ and $\mathbf{w}_{RH}$ aim to extract. On average there was an evident reduction in μ and β band power during the task execution.

large weight magnitude associated with it. Figures 5.5 C)-D) illustrate such variance contrast, which CSP aims to pinpoint. These figures were obtained by averaging the time-frequency representations (TFRs) of raw data from the highlighted sensor and all trials of the corresponding mental task, and normalizing it to the average PSD of

the pre-stimulus interval. As a result, figures 5.5 C)-D) highlight the relative reduction in μ and β band power during the mental task execution, i.e. the ERD effect, which on average occurred roughly 500 msec after the cue was shown to the user at time point 0. Such visual representations may be used to directly select the bands of interest, in cases when the characteristic effect is as evident as in graphs 5.5 C)-D).

Next, figure 5.6 illustrates the projection of EEG data onto the spatial filters $\mathbf{w}_{LH}$ and $\mathbf{w}_{RH}$, described above. For this purpose, we used two arbitrarily selected trials - one of left hand motor imagery, $\mathbf{M}_{LH}$, and one of right hand motor imagery, $\mathbf{M}_{RH}$. The four graphs in figure 5.6 demonstrate how CSP filters may be used to contrast two different conditions on the basis of their projection's variance. Note how the filter produces a low variance projection when the trial matches its desired class, which corresponds to the extraction of the ERD effect.
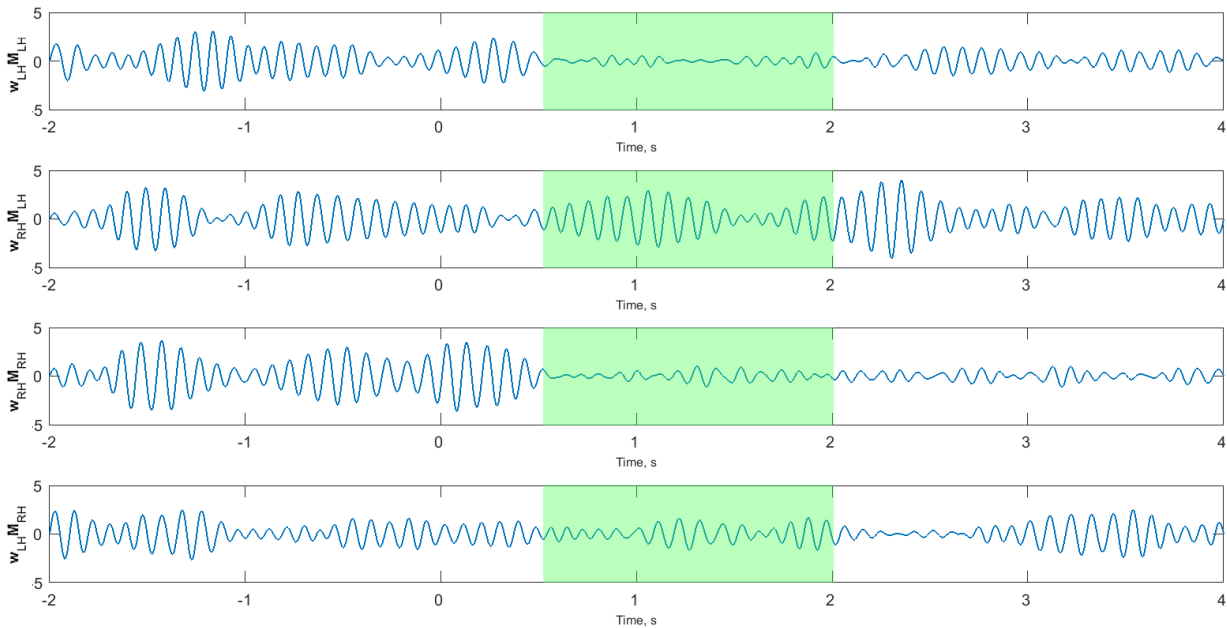
FIGURE 5.6: Extraction of ERD effects using a set of spatial filters. The figure contains different combinations of left-hand and right-hand imagery signals ($\mathbf{M}_{LH}$ and $\mathbf{M}_{RH}$) projected onto CSP filters $\mathbf{w}_{LH}$ and $\mathbf{w}_{RH}$. The time interval highlighted in green was used for feature extraction.

Feature selection and classification.

Next the extracted FBCSP features were ranked by their class separability. For this purpose we have utilized the relative entropy criterion, also known as Kullback-Leibler distance or divergence, which quantifies the difference between two probability distributions (Bishop 2006; Theodoridis and Koutroumbas 2006). Such feature ranking was performed in a one-vs-rest manner, separately for each variable in $\mathbf{F}_{full}$ and each class of data. Let q denote the class of data, for which all the features are being ranked, and let p represent the particular feature. Within the ranking process for predictor p and class q the two distributions for were defined as follows: the first distribution was comprised by the values of p from trials of class q, the second distribution then was formed by the values of the same feature p extracted from trials of all classes except q. The Kullback-Leibler distance between the two distributions is then the measure of how useful is the feature p for classification of class q. An example of feature ranking results for a single subject in the dataset is shown in figure 5.7.

After the predictor variables were ranked, the sequential forward feature selection was utilized in order to find a subset of features
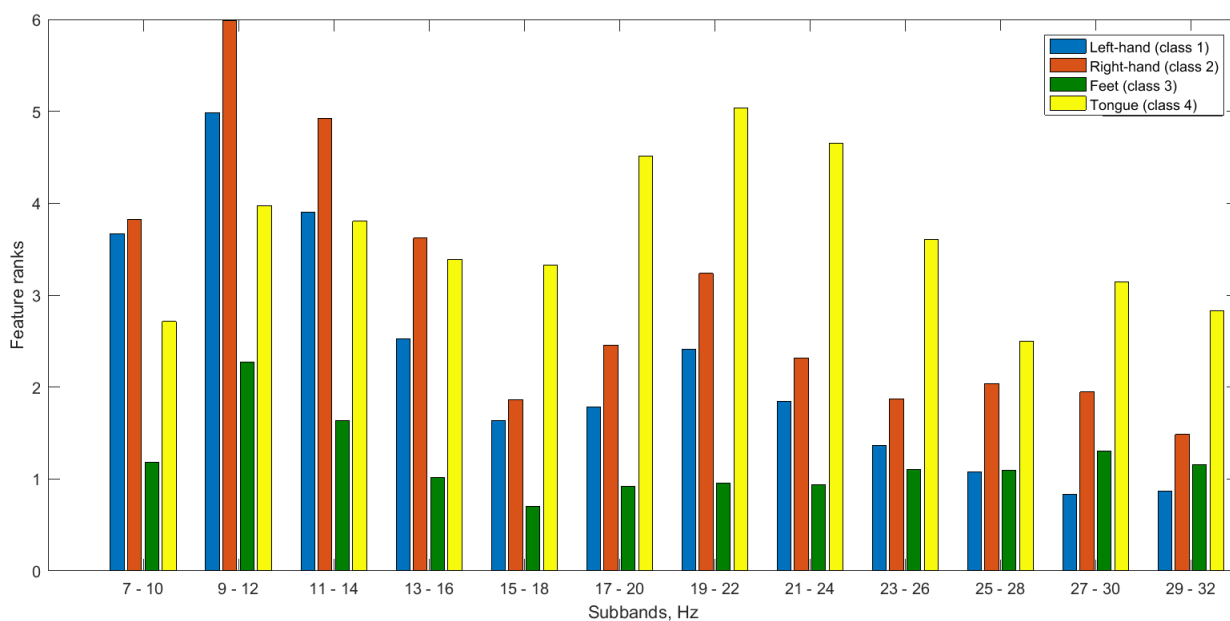
FIGURE 5.7: The distribution of feature ranks over the subbands estimated for a single subject in the dataset.

yielding the best classification reliability. Within such a selection process a number of LDA classifiers were trained iteratively with different number of the highest ranked features, and their performance was assessed using the evaluation protocol defined in BCI competition IV. The evaluation procedure was defined as follows: first, for each subject the classifier was trained using the feature vectors extracted only from training data, where the correct class labels are given for each EEG trial. Next, this classifier was tested on the feature vectors extracted from the evaluation data recorded on a different day, where the class labels were not embedded in EEG, but given separately after the competition. Such evaluation procedure describes the classifier's generalization capabilities, i.e., its performance given a certain degree of control signal's inter-session variability. At the feature selection stage no more than 3 subbands were chosen for each subject in the dataset as the further increase in number of bands resulted in reduced classification reliability. The highest achieved classification accuracies for each subject in the dataset are presented in table 5.1.

5.1.4 Stage 2. Analysis in source space.

After the feature selection and classifier training/evaluation stages the selected frequency bands were used to decompose the raw EEG data in preparation for the further source reconstruction and analysis in source space. As was mentioned previously, the band selection may be alternatively conducted by the visual assessment of TFRs normalized to the average power during rest, in cases when the ERD/ERS effects are evident. Prior to source reconstruction the raw EEG data was segmented and preprocessed as described in section 5.1.3 and filtered into separate subbands selected at the sensor space analysis.

Source reconstruction.

Source reconstruction was implemented using the forward model based on the same ICBM 152 head geometry and source grid as described in section 4.2.1. However, the dataset used consists of EEG recordings from a different electrode montage with 22 sensors. The
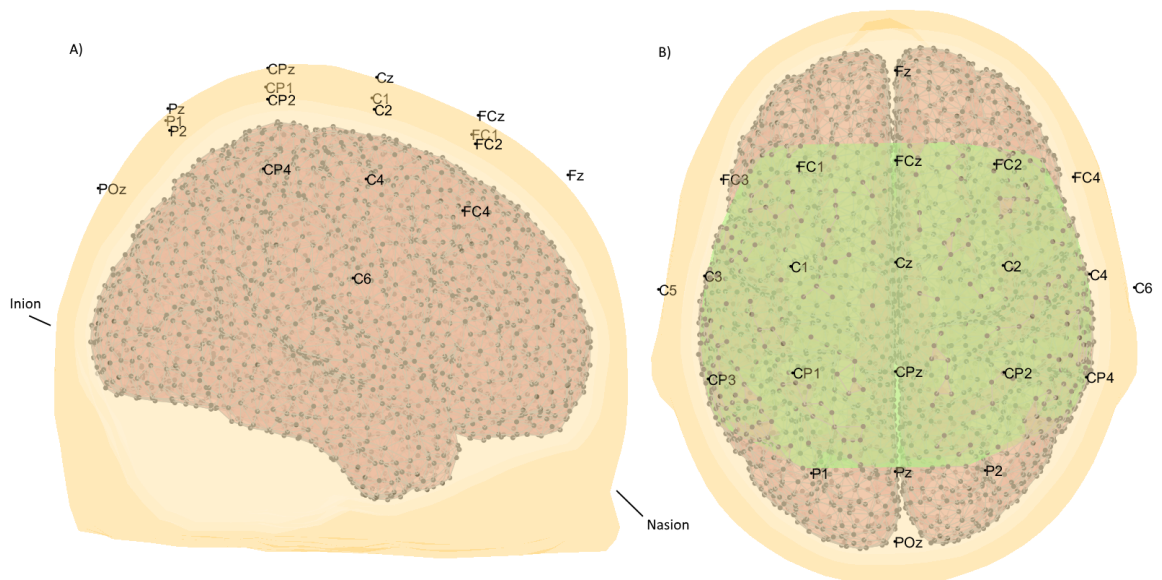
FIGURE 5.8: Visualization of forward head model used in simulations. EEG sensor locations are marked by channel labels and source locations on the cortical surface are represented by black dots. A) Side view from the right. B) Top down view with region-of-interest (ROI) highlighted in green.

forward model together with the EEG electrode locations is displayed in figure 5.8. The ROI was defined heuristically as 1735 locations (38.5 % of sources) spanning the expected area of ERD/ERS effects associated with motor imagery.

Within the source analysis, the cortical current estimates were obtained using the WMNE method. The linear inverse operator $\mathbf{G}$ with regularization parameter $\lambda = 0.01$ and source depth compensation matrix $\mathbf{W}$ was calculated as described in section 4.1.2:

$$\mathbf{G} = (\mathbf{W}^T\mathbf{W})^{-1}\mathbf{L}^T(\mathbf{L}(\mathbf{W}^T\mathbf{W})^{-1}\mathbf{L}^T + \lambda\mathbf{I}_m)^{-1} \tag{5.4}$$

Next, this operator was applied to each pre-filtered signal observation and only the source magnitudes from the ROI (shown in figure 5.8) were extracted and used in the following processing.

CSP estimation and feature extraction.

Next the reconstructed source activity from each trial's subband was used to estimate a set of CSP filters within the individual bands. This process was identical to the feature extraction described in section 5.1.3 with the difference that only the previously selected subbands were used and the dimensionality of source representation was much higher compared to the original sensor data. For each
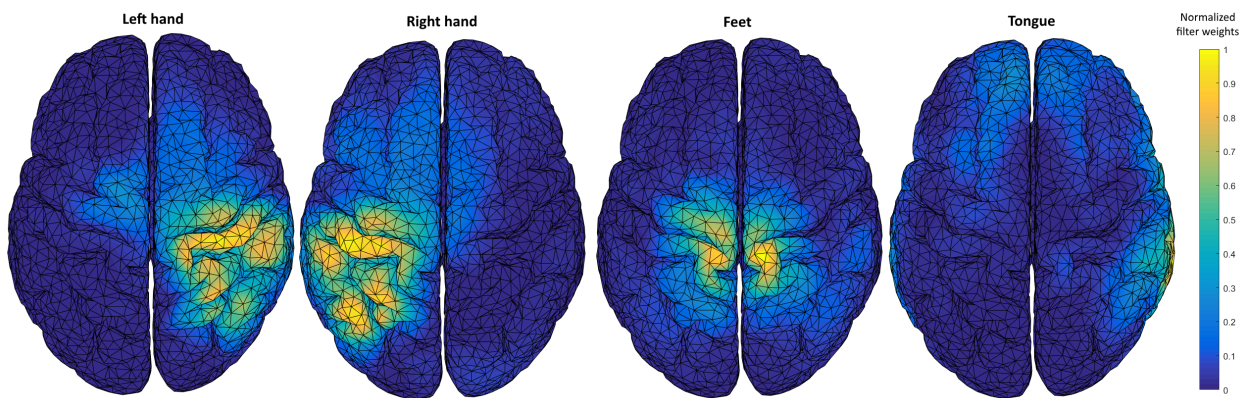
FIGURE 5.9: The most desirable CSP filters for all four classes of data. Distribution topographies of the normalized filter weights are shown in color over the standard cortical surface. For display purposes these filters were calculated over all sources in the model without the ROI extraction stage.

subband and subject in the dataset the multiclass set of filters $\hat{\mathbf{W}}_{\mathbf{csp}}^i$ was calculated by grouping and contrasting the source data in the OVR manner.

Figure 5.9 contains the normalized weight distribution topographies of the most desirable CSP filters for all given classes of mental tasks. These filters were obtained using the data for subject 8 in the dataset and a single subband of 9-12 Hz. For visualization purposes the filters presented were calculated over all sources in the model, without the ROI extraction stage. The reader may notice how closely the filter spatial profiles correspond to Penfield's sensory homunculus (see figure 1.5). As with sensor data, only the two most desirable CSP filters were selected per class of data and per subband, yielding a set of band-specific unmixing matrices $\hat{\mathbf{W}}_{\mathbf{csp}}^i$ with a total of 8 filters for each frequency band. Next, the subband filter sets $\hat{\mathbf{W}}_{\mathbf{csp}}^i$ were used as described in section 5.1.3 to obtain the feature vectors $\mathbf{F}_{full}$ representing a single motor imagery observation. Taking into account that no more than 3 frequency bands were used for each subject, the feature vectors $\mathbf{F}_{full}$ contained up to 24 predictor variables.

Feature selection and classification.

The projection of source trial data onto the CSP projection matrix $\hat{\mathbf{W}}_{\mathbf{csp}}^i$ greatly reduces dimensionality: within our settings 3×1735 current dipole moments from the ROI were decomposed into only 8 components per subband. Considering that only the indicative frequency bands were used in preprocessing and that only the strongest CSP filters were selected from the full set, the feature selection process was less beneficial in terms of further reduction of feature vector length and classification improvement. However, forward sequential feature selection was still performed for all subjects in the group and a small number of features (1-6 for different subjects) was selected if it resulted in classification accuracy increase. The same as with sensor data, a separate multiclass LDA classifier was then trained and evaluated according to the same procedure as described for sensor data (see section 5.1.3). A comparison of classification accuracy results for conventional wide band CSP, sensor FBCSP and source FBCSP methods is given in Table 5.1.

TABLE 5.1: Classification accuracy estimates.

Subject	CSP sens, %	FBCSP sens, %	FBCSP source, %
1	70.3	74.4	76.9
2	59.7	66.3	65.5
3	80.6	83.5	86.1
4	60.3	68.2	69.3
5	58.9	65.6	66.8
6	57	65.3	68.7
7	77.9	86	87.8
8	78.3	84.3	90.9
9	70.1	76.1	79.2
AVG $\pm$ STD	**68.1 $\pm$ 9.3**	**74.4 $\pm$ 8.5**	**76.8 $\pm$ 9.5**

Discussion.

According to our results, on the whole subjects have shown different capabilities for eliciting strong and consistent BCI control commands, which explains the large variance of the accuracy estimates. Within the 4-class classification paradigm the random classification accuracy is 25%. As can be seen from table 5.1, FBCSP feature extraction applied to reconstructed source components consistently outperforms conventional CSP method in sensor space. With source FBCSP features the highest classification accuracy of 90.9% was achieved for subject 8 in the dataset, which significantly exceeded the average rate of 76.8 $\pm$ 9.5% between all 9 subjects.

As described previously, within the SMR BCI paradigm the control signal may be defined as the frequency-specific variation in band power, relative to the resting condition, which is referred to as ERD or ERS effects. Thus, the aim of the proposed signal processing scheme is to lock such effects in time, frequency and space. With the given fixed trial-based dataset the locking in time corresponds to the time window selection, which can be done through visual assessment of

averaged data or heuristically, by applying several differently positioned time windows and selecting the one, which maximizes classification performance (or feature metrics). In real-time BCI applications this corresponds to a simple sliding window. Locking of characteristic signal in frequency was done by the application of a filter bank and further selection of indicative bands based on feature metrics or classification performance. The CSP filters, estimated from the grouped training data, correspond to locking of the ERD/ERS effects in space. Within such a time-frequency-space filtering approach the source reconstruction does not affect the performance of filtering in the time domain. Besides that, the WMNE inverse solutions are linear, in other words, they do not produce harmonics and, as shown in the simulated example (see section 4.2.4) are capable of accurate local oscillatory activity reconstruction. Therefore, the employed source imaging affected only the performance of CSP method by providing it with data of higher dimensionality and, at the same time, less linear interdependency. Besides, considering the capabilities of EEG imaging for isolation of source components based on their origin, the ROI extraction represents the partial removal of noise energy that appears to be more efficient and flexible compared to the simple channel selection in sensor space.

The positive effect of source localization can be demonstrated by performing a comparison of features extracted from sensor and source representations of the signal. Figure 5.10 contains the parallel coordinate visualization of all training feature vectors extracted from a single 9-12 Hz band of subject 3 in the dataset. This type of plot is often used to visualize multidimensional data such as a set of feature vectors. Here each line represents the observation (a feature vector) and the line color indicates the class of data, i.e., the type of mental task performed during the observation. The feature values are defined at the labeled points on the x-axis denoting the feature indices. With q denoting data class and i denoting the filter index in the full CSP set the feature values f_{qi} were ordered according to the utilized CSP filters as $(f_{11}, f_{12}, f_{21}, f_{22}, f_{31}, f_{32}, f_{41}, f_{42})$. As was described before, these values represent the logarithm of normalized variance calculated for the signal projections obtained using the selected CSP filters (two filters per class). For example, from the plot it can be seen
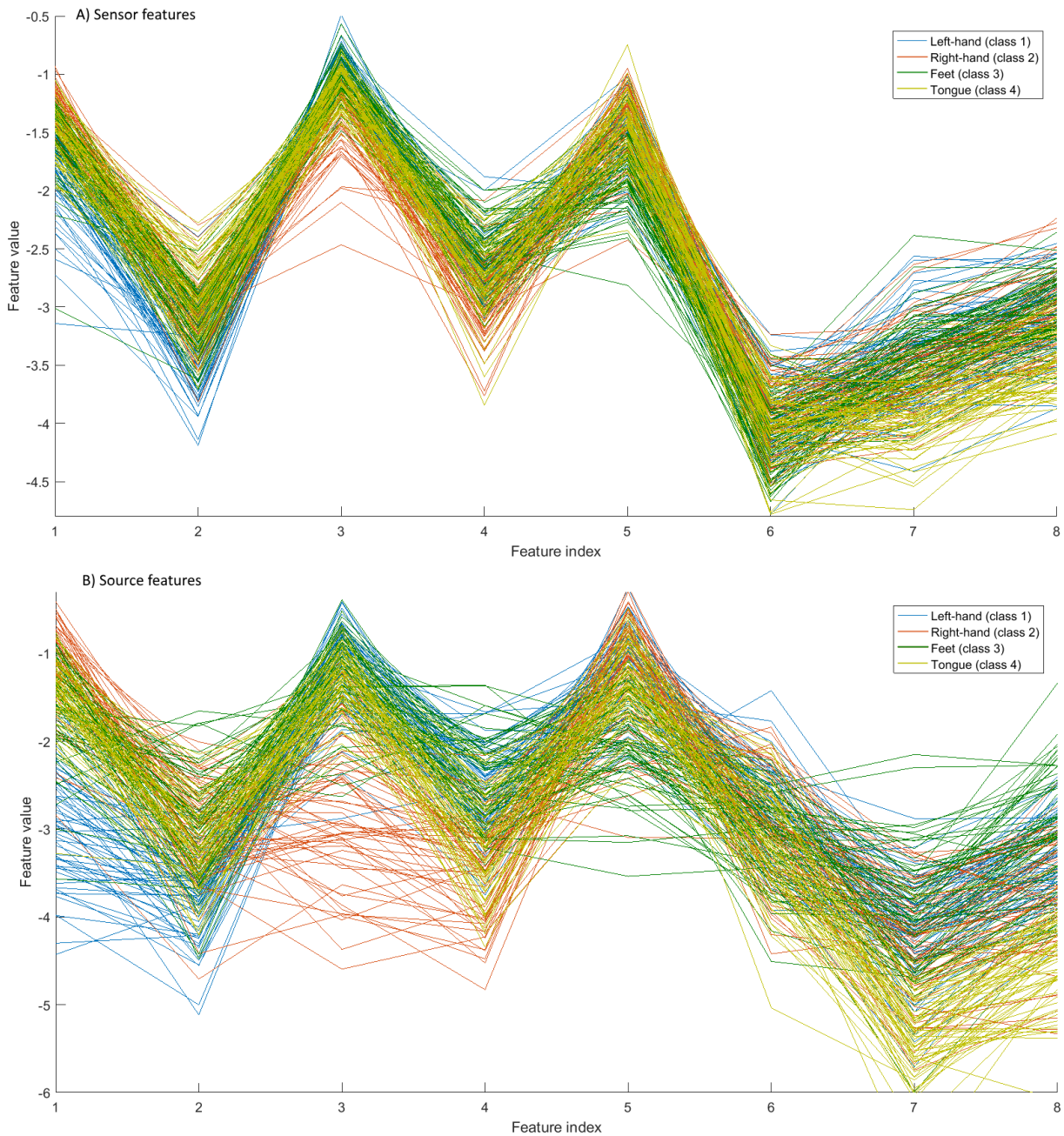
FIGURE 5.10: The parallel coordinate visualization of
sensor and source CSP features extracted from a sin-
gle subject and 9-12 Hz subband. A) Visualization of
sensor features. B) Visualization of source features.

that the values of features f_{21}, f_{22}, extracted from trials of right hand
imagery (class 2) using the CSP filters designed for this class, gener-
ally had lower values than features extracted from different classes
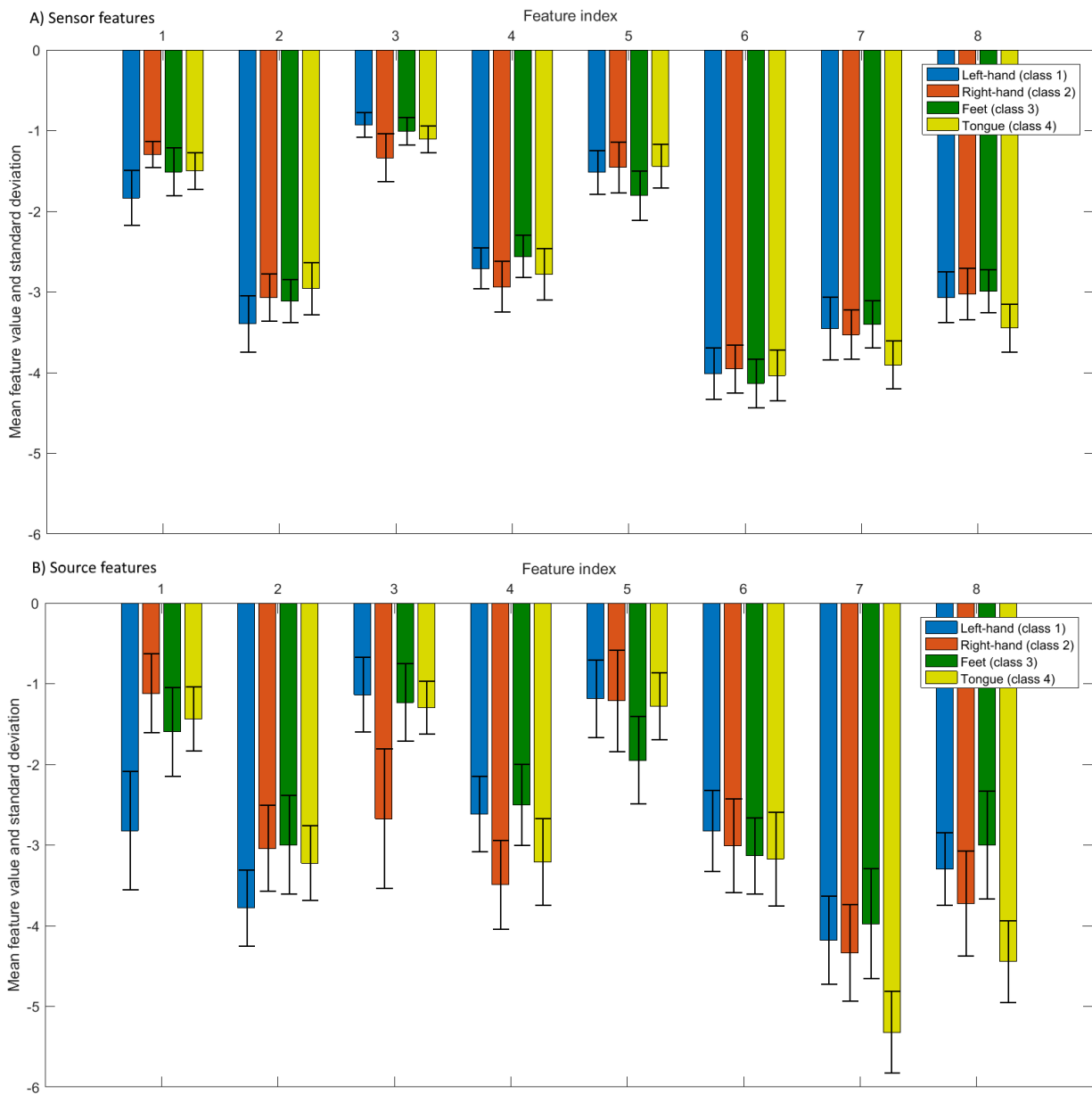
FIGURE 5.11: Class means and standard deviation of features shown in figure 5.10. The source features have clearly larger distance between the class means, which explains their better class separability compared to sensor features.

with the same filters. This corresponds to the extraction of ERD effect during the motor imagery.

Figure 5.11 demonstrates the effect of source reconstruction on feature class separability shown for the same set of feature vectors

as displayed in figure 5.10. This figure shows the class means of the given features and their standard deviations. Here the source reconstruction resulted in features with slightly higher variance, although significantly larger distance between the class means, which explains the observed increase in classification reliability in source space compared to sensor space.

5.2 Conclusion.

This chapter was dedicated to the overview of the proposed EEG signal processing and classification scheme for motor imagery BCIs. Source reconstruction technique described in chapters 3 and 4 of this thesis was combined here with the filter band selection procedure and CSP algorithm to achieve an enhanced extraction of spatial EEG features. This proposed signal processing method was applied to the benchmark motor imagery dataset from BCI competition and compared to a similar EEG classification scheme in sensor space.

As our results show, source reconstruction and subsequent ROI extraction reduced the impact of noise and artifacts on the indicative components of EEG, and resulted in features with better class separability qualities, which explains the observed increase in classification accuracy.

The proposed signal processing scheme was designed with due regard to its applicability in practical control BCIs. In order to facilitate quick and autonomous BCI calibration for each subject, the indicative frequency bands and spatial filters were selected automatically, through a feature selection procedure. Besides, the processing stages involved in EEG classification (band-pass filtering, linear source reconstruction, ROI extraction) can easily be implemented in real-time, which will be demonstrated in the next chapter.

Chapter 6

Design of asynchronous real-time BCI.

Chapter 5 demonstrated the benefits of source localization for BCI control signal classification. Primarily, the source data representation reduces the negative effects of inter-electrode coupling, which improves the class separability of the extracted variance features. It maps the sensor data onto a domain, where more flexible region-of-interest extraction is possible. In the source representation the components that constitute the recorded EEG measurements are segregated on the basis of their location on the modeled brain surface. Heuristic ROI definition and data-driven spatial filter estimation with CSP facilitate the selection of sources relevant to motor imagery classification. The signal components that lie outside the ROI are discarded, and thus, no longer contribute to the extracted variance features. All in all, this results in features with better class separability properties, which provide for more reliable classification performance as shown in the previous chapter.

In recent years there have been a number of reported BCI applications employing EEG source analysis (Wentrup et al. 2005; Congedo, Lotte, and Lécuyer 2006; Frolov et al. 2013; Bhattacharyya et al. 2015). However, such an approach is rarely validated in real-time motor imagery BCI implementations, but is generally tested on common datasets. Examples of recent online source-based BCI developments include (Congedo, Lubar, and Joffe 2004; Besserve, Martinerie, and Garnero 2011; Bauer and Pllana 2014). In this chapter our novel source CSP feature extraction method is validated in a real-time asynchronous SMR BCI application.

6.1   Cybathlon 2016.

The development of asynchronous control BCI was conducted in collaboration with the Team Gray Matter project, which aimed to compete at the BCI race at Cybathlon 2016, the World's First Championship for Robotic and Technology assisted "parathletes" (Cybathlon web page). Our goal was to develop a practical real-time 4-state EEG BCI for a quadriplegic user (subject 1) who was to operate it at the competition. The four states included 3 control commands and an idle state, during which the BCI must not send commands. According to the competition requirements the proposed system had to be capable of sending the command at any time (asynchronous BCI), free from any external stimulation (no SSVEP or P300) and capable of muscular artefact rejection, i.e., suppression of BCI output during the artifacts.

The Cybathlon BCI race represents a specifically designed computer game, where players control an avatar that passes through series of obstacles, which the users must overcome by executing the correct BCI command. The obstacles are represented by colored and animated platforms, where color gives a cue for the BCI command to be performed (see figure 6.4). When the user casts a correct control command, the avatar accelerates up to the maximum speed. When a wrong or no command is received by the game, the avatar moves with the default speed (quarter of the maximum). Since the game's objective is to reach the finish first, the player's goal is to not only execute the correct commands at the right time, but also to *maintain* the correct commands over the whole level comprised of multiple platforms. Considering that there are no rest periods during, in such a feedback training paradigm, the time it takes to reach the finish points to the very practically important metric of BCI performance, i.e., the fraction of time that the user managed to maintain the intended command.

Within this project a real-time BCI feedback training system with several different variations has been implemented, and our subject trained through a course of 14 sessions conducted over 3 months.

The training provided for improvement in BCI performance and allowed the subject to acquire confident control in 2-class training sessions. Unfortunately, due to health issues related to his condition, the subject could not finish the training for 3- and 4-state BCI and participate in the competition. However, a similar training paradigm for a different subject, a healthy adult (subject 2), has been implemented and the novel application of source CSP features to real-time motor imagery classification has been verified.

6.2   BCI user training.

The overall goal of this work was to design a control BCI, use it to train a subject, achieve reliable control over 3 BCI commands and thus maximize the subject's performance in the competitive Brain-Runners game. The latter depends on the two main aspects of BCI control: the user must be able to quickly switch between the control commands and also reliably maintain the chosen command for the required duration. Besides, the goal was to evaluate our proposed BCI signal processing scheme in a practical application.

With each participating subject the BCI training course was conducted over 3 essential stages schematically described in figure 6.1. First, a number motor imagery observations were obtained in a few trial-based recording sessions with no visual feedback. This data was used to test the suitability of various mental tasks (BCI commands) and train classifiers for the initial feedback training sessions.

Next, after a set of BCI commands has been defined, the subjects were trained to discriminate between two commands at a time in a feedback training procedure with BrainRunners. Here BrainRunners game was used to provide visual cues for different BCI commands and visual indication of classification results to facilitate the feedback training process. The CSP feature extraction is strongly affected by
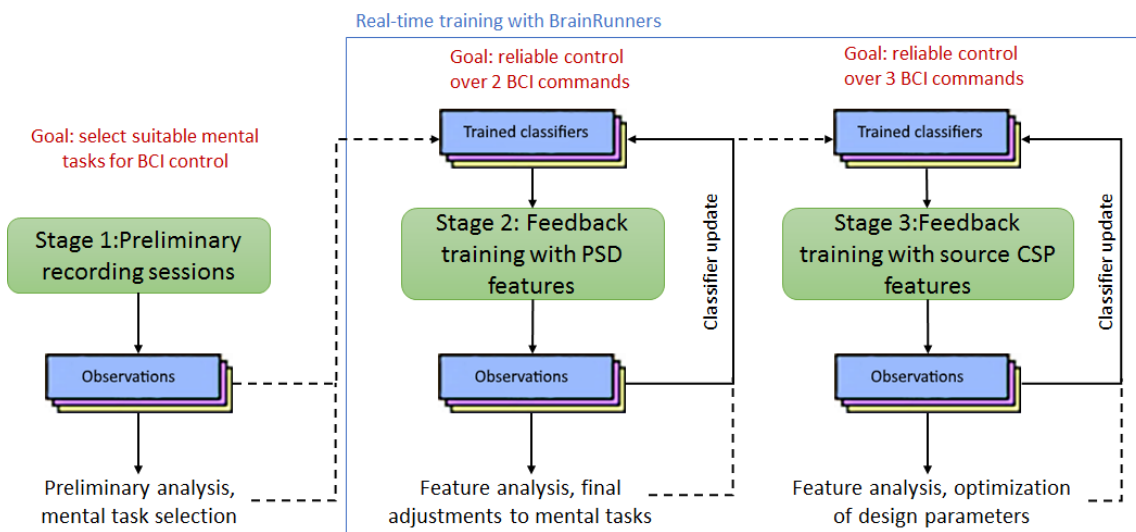
FIGURE 6.1: Stages of the BCI training course.

outliers, and considering the amount of noise and artifacts in the preliminary recordings, it was found that a simpler BCI based on PSD features was more suitable for the initial feedback training. Therefore, the subjects were allowed to train switching between different pairs of commands in several feedback training sessions with PSD BCI.

After the subjects had sufficiently improved their consistency of BCI command execution, the number of outliers in data was reduced and the CSP filters extracted from motor imagery observations became more focal and produced more indicative features. Therefore, the final stage of training course consisted of multiple sessions of feedback training focused on discrimination between 3 control commands with source CSP BCI. The following sections give further details on the employed signal processing and training results.

6.2.1 The EEG headset.

The EEG data from both subjects were acquired using the g.Nautilus headset provided by the g.tec company for the competition (g.Nautilus product page). This headset has an embedded lightweight amplifier,
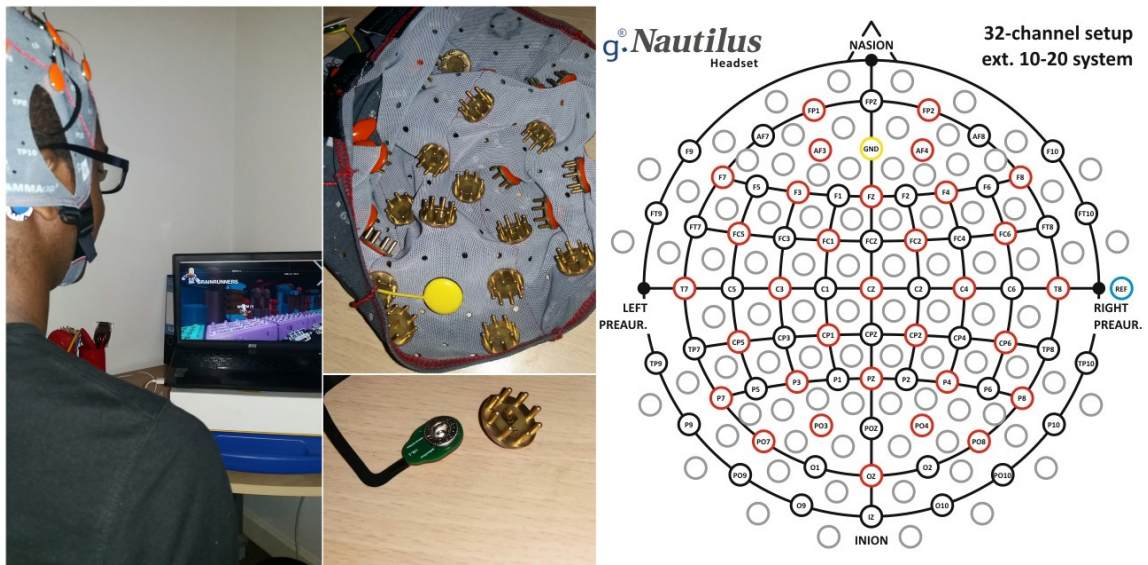
FIGURE 6.2: Photos of subject 2 during the BCI feedback session, g.Sahara electrode close up and sensor layout of g.Nautilus 32-channel headset (available positions are shown in red).

which forms the digitized EEG signal with a 500 Hz sampling rate, and transmits it over a wireless connection. The signal is recorded from a 32-channel montage, shown in figure 6.2. This system relies on a set of g.SAHARA dry electrodes, which allow for EEG signal detection with an impedance of up to 100 kΩ. In practice this means that these electrodes do not require the lengthy process of conductive gel application and subsequent cleaning, and hence, the subject preparation for recordings took only 5-10 minutes, which is a crucial factor considering that 30-50 minutes are generally required for conventional gel sensor preparation. However, the signal provided by g.Nautilus is very noisy and susceptible to muscular artifacts compared to gel electrode systems. The product page states that the g.SAHARA dry EEG electrodes were specifically designed for rapid prototyping and preliminary experiments prior to large scale research. The provided signal quality is considered to be sufficient for analysis up to the beta band of EEG (g.SAHARA product page). Although we found the rapid deployment of experiments to be a great advantage, achieving robust signal quality in real-time training sessions was a challenging task.

The EEG data from g.Nautilus can only be obtained using the proprietary Simulink model blocks bundled with the headset. Therefore, preparatory analysis was performed in Matlab and the real-time experiments were conducted in the Simulink environment.

6.2.2   Organization of recording sessions.

Prior to the user's real-time feedback training it is necessary to have a sufficient amount of EEG observations in order to train an initial classifier. For this reason the first recording sessions were dedicated
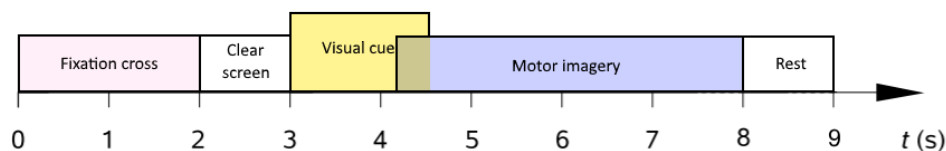
FIGURE 6.3: Timing scheme of the trial-based recording paradigm.
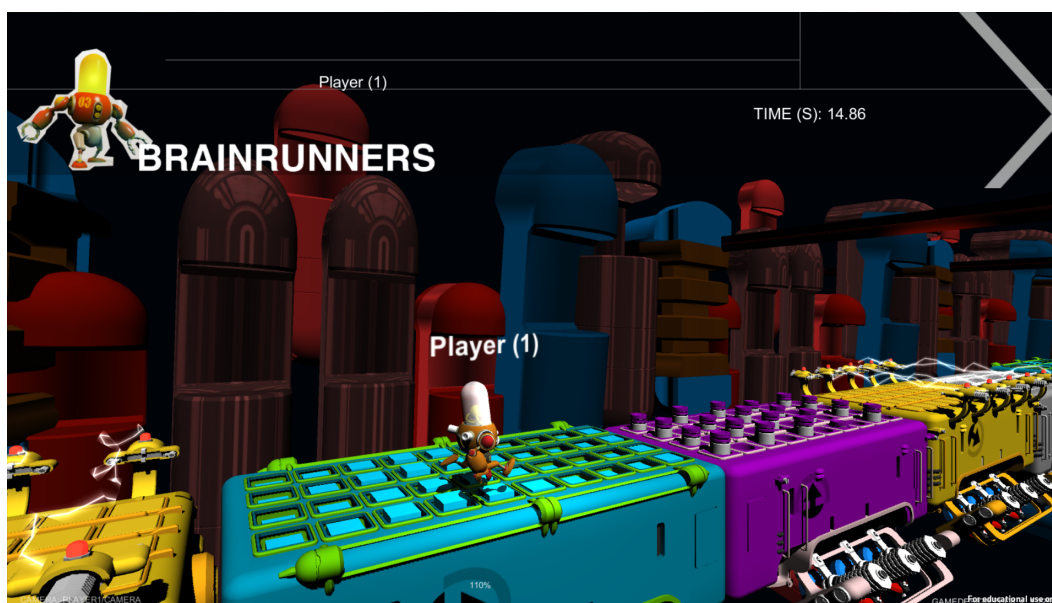
FIGURE 6.4: Screenshot of the Brainrunners BCI game.

to the collection of this data in no-feedback trial-based sessions structured similarly to what is shown in figure 5.1. The timing structure of our trial-based recording paradigm is illustrated in figure 6.3. Markers denoting the trial onset and the type of cue were embedded into the EEG signal as an additional channel, facilitating the trial segmentation. Each trial-based recording session typically consisted of 3-5 runs of 45 trials each.

The feedback training sessions were conducted using the Brainrunners BCI game (screenshot in figure 6.4), provided by the competition organizers. This software receives the encoded BCI commands and sends the event markers for trial segmentation using UDP. The user visual feedback indicating success or failure of the correct mental task execution is given by the avatar's action (run, jump or slide) and its pace. As mentioned previously, the correct control command results in acceleration up to the maximal speed, otherwise the avatar moves with the default speed (quarter of the maximal).

Tasks for BCI control were chosen with respect to the general framework of SMR BCI design and preliminary analysis of initial recording sessions, where the data was collected for a variety of mental tasks. Subject 1, who suffers from severe spinal cord trauma, used three classes of commands: right hand motor imagery (class 1), left hand motor imagery (class 2) and arithmetic subtraction (class 3). For

classes 1 and 2 the user was instructed to imagine repetitive ballistic hand movement - punching with the right hand and reaching for a target with the left hand. Although arithmetic subtraction does not correspond to the voluntary SMR regulation it has shown better discriminability compared with, for example, feet or tongue movement imagery. For this task the user was instructed to serially subtract 7 from a large two-digit number. Conforming to the findings in relevant research (Penny et al. 2000; Curran and Stokes 2003), such a cognitive task was found to be detectable using the patterns of PSD features (see section 2.2.2). For subject 2 only the motor imagery tasks were selected, namely right hand (class 1, repetitive punching), left hand (class 2, repetitive reaching and grabbing) and feet (class 3, raising both feet).

6.2.3 Neurofeedback training using PSD features.

Preparation for training session.

After several recording sessions with no feedback, we had obtained a sufficient amount of EEG data to train the initial classifiers and start the feedback training with Brainrunners. The BCI for the first several training sessions was designed using the simple PSD features that were found to perform more reliably with untrained subjects (Boostani et al. 2007; Mason et al. 2007).

The signal processing scheme of the employed PSD BCI is schematically described in figure 6.5. Preparation for training sessions consisted of offline analysis, where the EEG observations from the latest 3-4 sessions were used to train the classifiers. For feature classification three separate OVR SVM classifiers were used, each trained to discriminate a single class against the remaining ones. The final interpretation decision was made by voting: the classifier with the highest score defined the type of command sent to Brainrunners. The
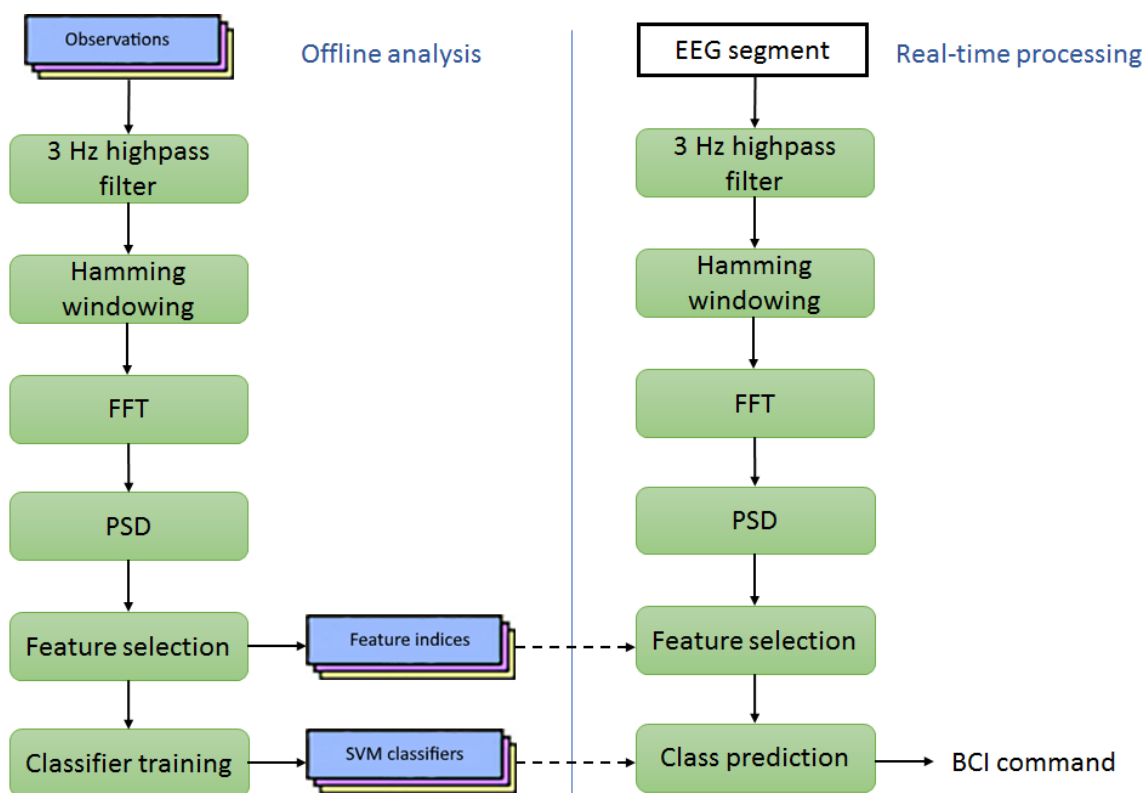

FIGURE 6.5: Signal processing scheme of the employed PSD-based BCI.

two main outputs of this analysis are the three trained SVM classifier objects and the three sets of selected feature indices.

First, at the preprocessing stage the available EEG data was segmented into trials using the event markers. Each trial was defined as a 5 second recording segment centered on the border of two platforms in the game. Next, the signal was filtered using the 3 Hz FIR highpass filter in order to center the data and remove irrelevant low frequency components. Short time segments containing the motor imagery observations were extracted from each trial and subsequently windowed using Hamming window function, which reduced the negative effects of spectral leakage on PSD estimation. Different lengths of time windows in the range of 0.5 to 2 seconds were tried during the training sessions. Longer time windows result in more stable BCI behavior, while shorter windows provide for better BCI responsiveness. In general, 0.8-1 second long time windows yielded a good compromise between the two.

A power spectrum for each extracted time segment was calculated as described in section 2.2.2. The resulting PSD values for each EEG channel were then "stretched" into a vector, which represented a single motor imagery observation. For example, with 1 second long time window the FFT of each EEG channel was defined over $N_f = 257$ frequency points. Considering that the number of channels $N_{ch} = 32$, this resulted in feature vectors having the dimensionality of $N_{ch} \times N_f = 8224$, which makes it necessary to apply some degree of feature selection before the SVM training.

Within the feature selection process, the PSD values corresponding to frequencies outside the 3-48 Hz range were discarded, due to prior >3 Hz highpass filtering, and because no evidence of class-indicative activity was found for frequencies above 48 Hz. Next, the remaining features were selected in the same manner as described in section 5.1.3. The features were ranked by their class separability using the relative entropy criterion. A forward feature selection procedure was then applied to find an optimal number of the most discriminative predictors. With PSD features 65-110 variables were selected to represent each observation. Considering the chosen OVR classification approach, both within the feature selection and classifier training processes the trials were grouped to contrast each class

against the remaining ones. The resulting feature vectors were then used to train three separate linear SVM classifiers.

Real-time BCI training.

The BCI training paradigm was implemented in the Simulink environment. Figure 6.6 shows the architecture of the BCI processing scheme that was utilized in real-time feedback training sessions. A description of the numbered functional blocks is given in the following list:

1. FIR 3 Hz highpass filter.

2. Buffer implementing the sliding time window. The length of a time window is 1 second, which with the given sampling rate corresponds to 500 samples. Time windows overlap by 75 % meaning that a new block of data is returned by the buffer every 0.25 seconds.

3. Block implementing the Hamming window. Suppresses the amplitudes at the time window edges, reducing the effect of spectral leakage.

4. PSD feature extraction block. Takes a second long interval of preprocessed EEG and returns the PSD values of each channel, stretched into a single vector.

5. Feature selection. Uses the three sets of PSD feature indices obtained during the preparatory analysis to extract the subsets of class-specific predictors.

6. Classification. The three SVM objects trained during the preparatory analysis return the SVM classification score every 0.25 second as defined by the sliding window. Here classification score stands for the signed distance of the input feature vector to the nearest point on the decision boundary. The final classification decision for each time window is made based on the highest SVM score (voting).
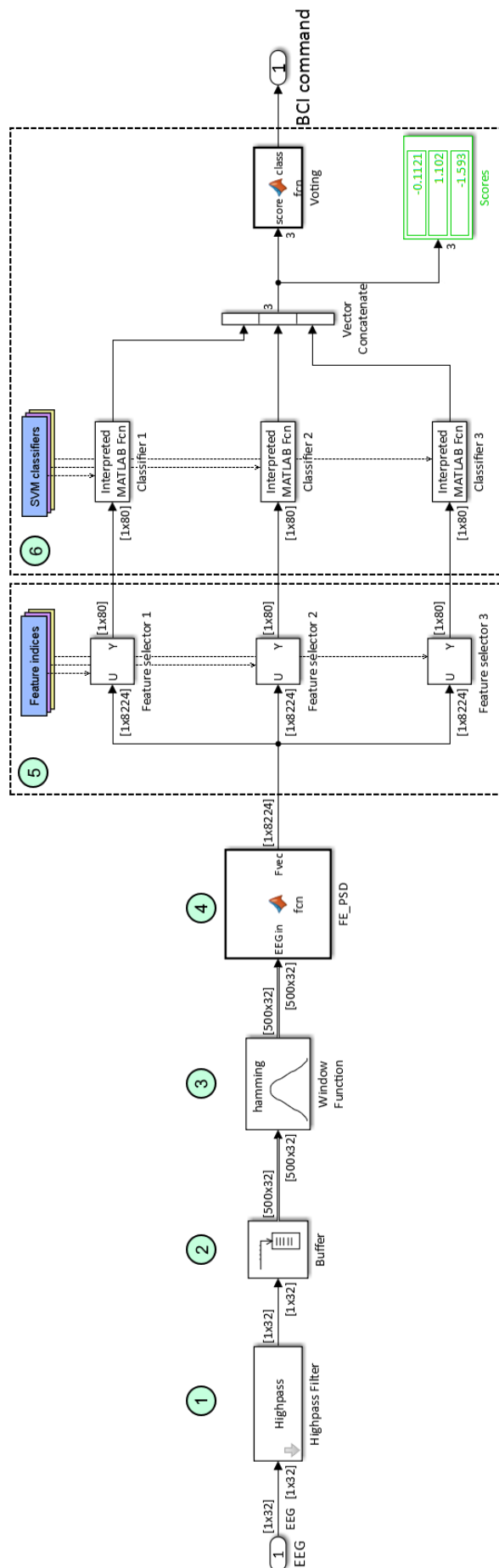
FIGURE 6.6: The real-time EEG processing system for BCI training. The image shows the Simulink model used for BCI training with PSD features. Steps of EEG signal processing are numbered and their brief description is given in the text.

6.2.4 Neurofeedback training using source CSP features.

Preparation for training session.

After several training sessions with PSD-trained classifiers, the subjects started showing progress in BCI control capabilities. As was mentioned earlier, subject 1, who was preparing for the BCI race at Cybathlon, could not continue training due to health issues, so the performance of source CSP features in real-time BCI was evaluated only by subject 2. The signal processing scheme used for classifier update and real-time EEG classification is described in figure 6.7. Preparatory analysis conducted before the feedback training included almost the same processing sequence as described in section 5.1.4 with the main difference being the subband selection process. Here the frequency bands were chosen based on visual assessment of TFRs of different mental tasks.

The whole EEG processing sequence is shown in figure 6.7. The
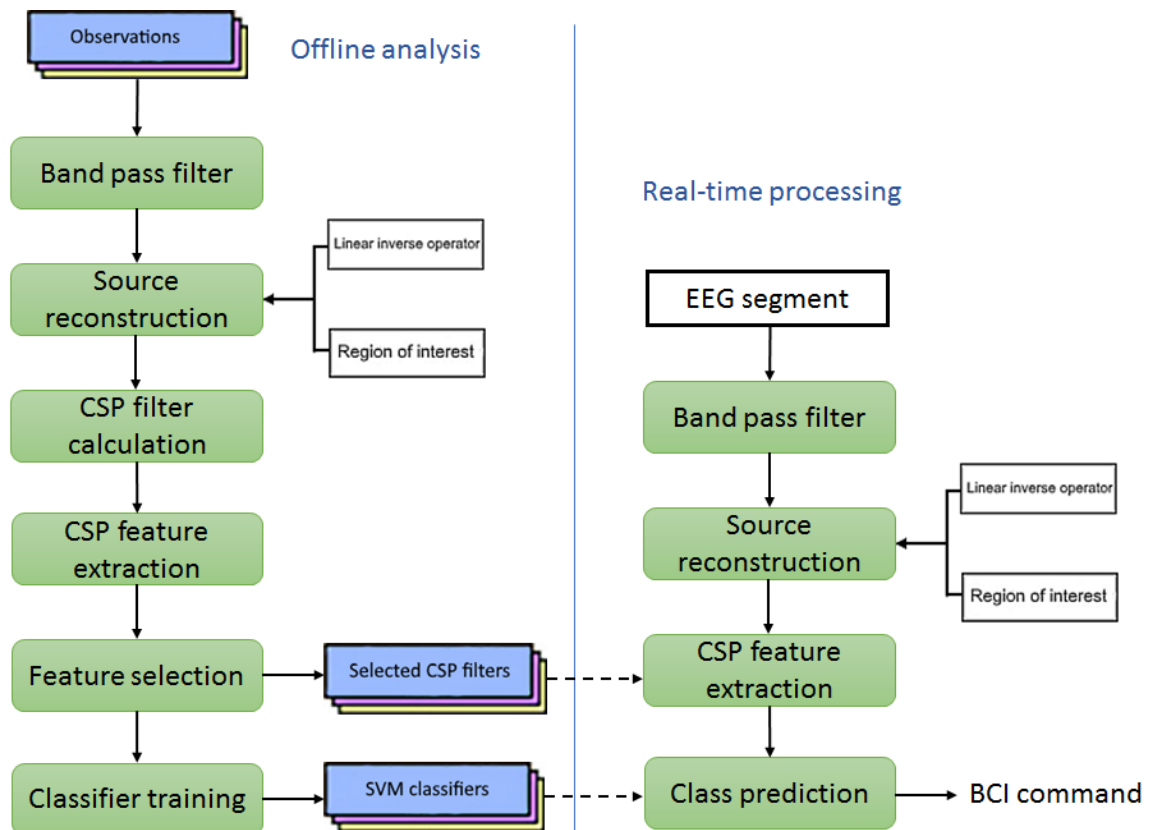
FIGURE 6.7: Signal processing scheme of the employed source CSP BCI.
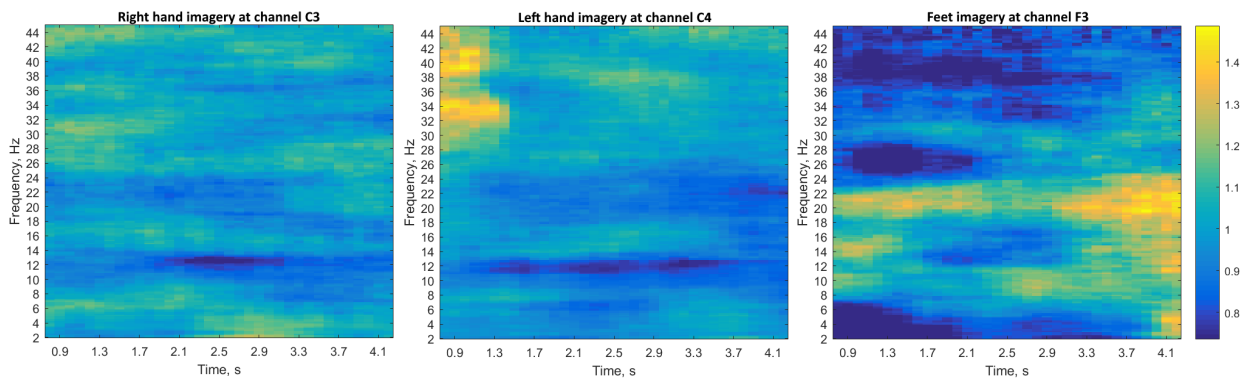
FIGURE 6.8: Time-frequency represenations of class-averaged trials from the last 5 training sessions. Left to right: TFR of class 1 at channel C3, TFR of class 2 at channel C4, TFR of class 3 at channel FZ. TFR images were obtained by using the Hanning windowing, 1.5 second long time windows and 4 Hz smoothing.

aim of preparatory analysis was to prepare the trained SVM classifier objects and selected spatial filters necessary for real-time feature extraction and classification. First, within this sequence the segmented trials from the latest 3-4 training sessions were band pass filtered to a frequency band defined from visual assessment of class-average TFRs (see figure 6.8). One second long time windows were utilized in the feature extraction process, since this length was found to provide a good tradeoff between the BCI stability and responsiveness. As was explained in section 1.3.2, ERD/ERS effects indicative of the motor imagery task generally occur in mu (7-13 Hz) and beta (16 - 31 Hz) bands of the EEG. According to findings described in, e.g., (Pichiorri et al. 2011), for some subjects the BCI feedback training gradually improves the consistency of ERD/ERS effects in the beta band. In our settings subject 2 had shown a certain improvement in beta band separability, however the most reliable real-time control was achieved using the band of 10-15 Hz, thus only this frequency bin was selected for further processing.

Next, WMNE source reconstruction was applied to the filtered training trials. The forward BEM volume conduction model based on general ICBM 152 head geometry was used to calculate the linear inverse WMNE operator with regularization parameter $\lambda = 0.01$ as
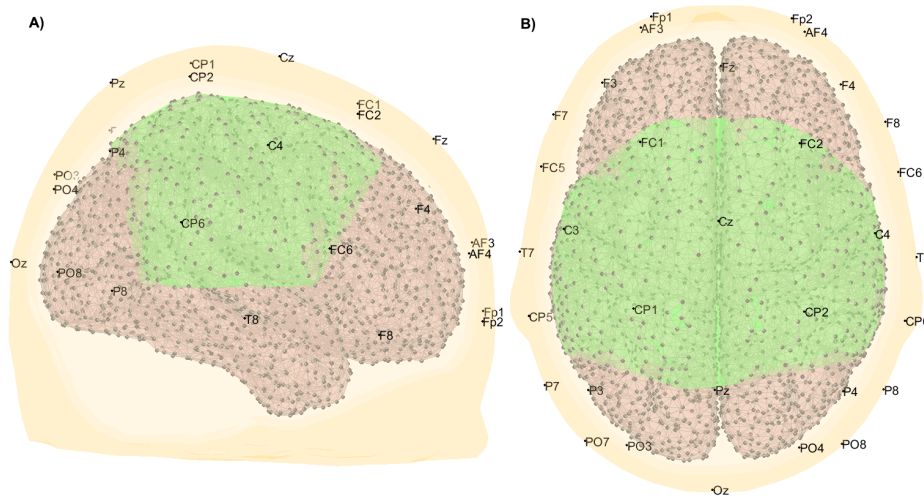
FIGURE 6.9: Visualization of the forward model and ROI shown by green color. A) Side view from the left. B) Top-down view.

described in section 4.1.2:

$$\mathbf{G} = (\mathbf{W}^T\mathbf{W})^{-1}\mathbf{L}^T(\mathbf{L}(\mathbf{W}^T\mathbf{W})^{-1}\mathbf{L}^T + \lambda\mathbf{I}_m)^{-1} \qquad (6.1)$$

The source space was defined over 4504 cortical surface vertices with three dipoles set at each point, yielding an inverse solution space of 13512 variables. Illustration of the forward model together with the ROI comprised of 1201 locations highlighted by green is shown in figure 6.9. Given the one second long time windows, after the ROI extraction each trial was represented by a matrix of 3603×500 variables.

The reconstructed source training data was used to calculate the class-average covariances necessary for CSP filter generation. The CSP feature extraction was implemented similarly to that described in sections 5.1.4 and 5.1.3 with the difference that only a single sub-band was used. As mentioned previously, the dry electrode g.Nautilus was found to be highly susceptible to noise and muscular artifacts compared to the traditional gel electrode systems. In such settings the conventional selection of CSP filters may not provide the desired results (see section 2.2.3), as CSPs with the largest eigenvalues may often extract the artifacts instead of the signal of interest. Therefore,

within the preparatory analysis all available spatial filters were employed in the feature extraction process, and the set of filters used in real-time training was picked based on the feature selection results. Sequential forward selection based on relative entropy predictor ranking was implemented identically to what was described in section 5.1.3. The best results in real-time training were achieved by using two filters per data class, which means that in a 3-class BCI training paradigm a single observation of motor imagery was represented by 6 predictor variables. Next, the same as with PSD features, the resulting labeled feature vectors were used to train three separate OVR SVM classifiers capable of discriminating each class against the remaining ones.

Real-time BCI training.

A combination of selected spatial filters, trained SVM objects and a linear inverse operator obtained within the preparatory analysis were used in real-time BCI training sessions. The same as with PSD feedback paradigm, BCI training with source CSP features was implemented as a Simulink model shown in figure 1.9. Description of the numbered functional blocks is given in the following list:

1. FIR 10-15 Hz band pass filter.

2. Buffer implementing the sliding time window. The length of time window is 1 second, which with the given sampling rate corresponds to 500 samples. Time windows overlap by 75 % meaning that a new block of data is returned by the buffer every 0.25 seconds.

3. Block implementing the EEG source reconstruction. Uses the WMNE linear inverse operator $\mathbf{G}$ to obtain the current density estimates $\hat{\mathbf{D}}$ from EEG data $\mathbf{M}$ as $\hat{\mathbf{D}} = \mathbf{GM}$. Only the source components from the ROI are propagated for the further processing.

4. Source CSP feature extraction block. Calculates the projection of a 1 second long interval of reconstructed source estimates

onto the selected set of 6 CSP filters. Logarithm of the normalized variances calculated for the resulting projections correspond to a single feature vector.

5. Classification. The three SVM objects trained during the preparatory analysis return the SVM classification score every 0.25 second as defined by the sliding window. Here classification score stands for the signed distance of the input feature vector to the nearest point on the decision boundary. The final classification decision for each time window is made based on the highest SVM score (voting).

For subject 2 the BCI feedback training with source CSP features was conducted over a course of 8 sessions. The relevant findings and training outcomes are given in the next section.
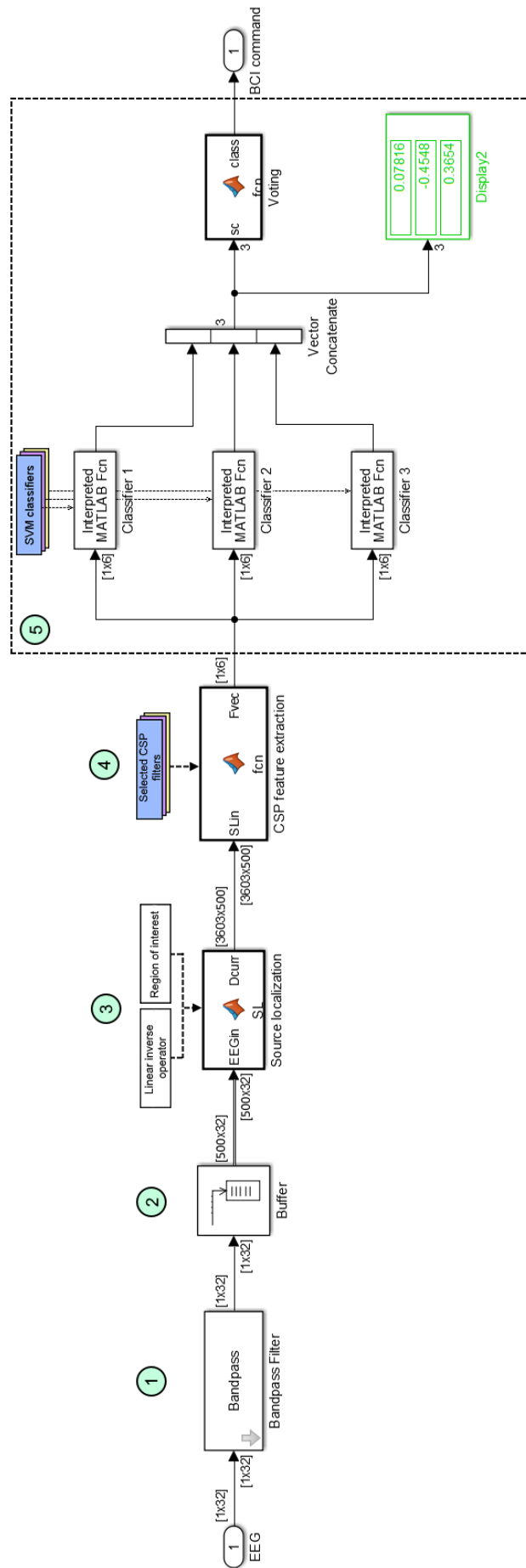
FIGURE 6.10: The real-time EEG processing system for BCI training based on source CSP features. The image contains the Simulink model, implementing the real-time feature extraction and classification of continuous input. Steps of EEG signal processing are numbered and their brief description is given in this section. The dimensions of signals at processing block ports are given in square brackets.

6.3 Results and conclusion.

Within the course of work with subjects 1 and 2 different BCI systems were produced based on various approaches for signal representation and interpretation. The overall goal of this work was to achieve the highest possible BCI performance, allowing for confident and comfortable control of the Brainrunners game. While the initial work mostly consisted of achieving sufficient EEG quality, parser scripts and preliminary recording analysis, at the later stages aspects were addressed such as co-adaptive training, feature extraction and classification approaches. In practice this means that the BCIs utilized in feedback training with subject 1, as well as the training protocol itself, were usually modified from session to session. As a result this obstructed the comprehensive comparative analysis of the gradual BCI training effect on the user's EEG. However, during the BCI practice course with subject 2 the training protocol was mostly left intact with only established and tested designs being utilized in real-time sessions. During each training session subject 2 completed 3-10 runs, where he had to go through a level consisting of 21 BCI tasks represented by colored platforms with color denoting the expected BCI command (see figure 6.4). The timing was defined in a way so that a single pane lasted 16.15 seconds, when no or an incorrect BCI command was cast, and 3.8 seconds when the correct command was received during the whole platform duration. Hence, a more reliable BCI control resulted in shorter run durations.

Figure 6.11 gives the run times throughout the whole BCI training course with subject 2. The orange vertical line here denotes the start of training with source CSP features. As can be seen from the figure, initial training with PSD-based BCI did not always result in increased classification performance, although the user reported that after several sessions the execution of BCI commands became less exhausting. After switching to the source CSP training paradigm we observed an evident increase in BCI performance, which resulted in significantly shorter run times. More specifically the BCI user found it much easier to *maintain* the control command, however its initial execution was somewhat less responsive compared to PSD BCI. The
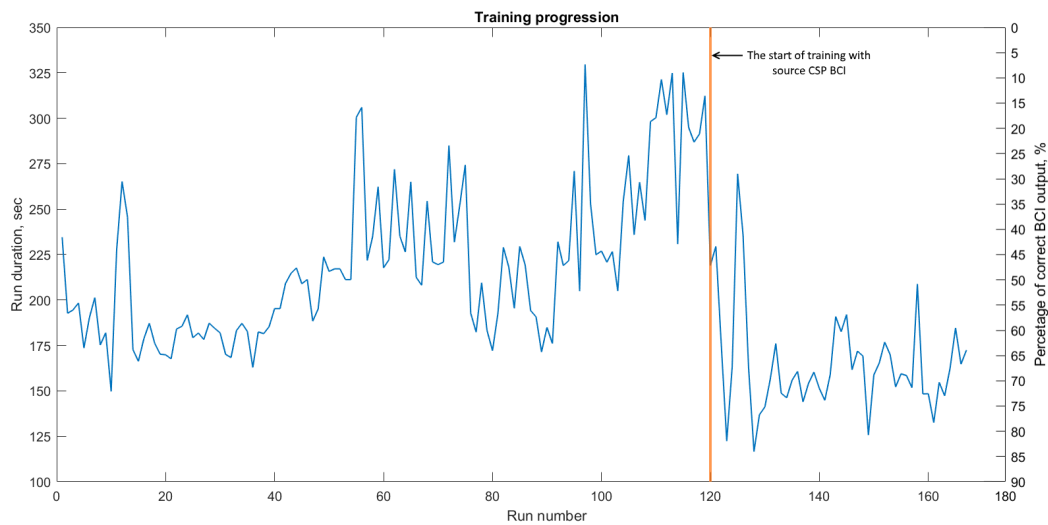
FIGURE 6.11: Run duration throughout the course of BCI training. The orange vertical line denotes the start of training with source CSP BCI. The fastest run took only 116.6 seconds, which corresponds to the BCI user holding the correct command during 83.3 % of the run duration.

best run with source CSP BCI lasted only 116.6 seconds, which corresponds to the BCI user holding the correct command during 83.3 % of the run duration. Besides the increase in feature separability, the source representation reduced the influence of noise and artifacts providing for more robust feature extraction with noisy signal from dry electrodes. The real-time BCI feedback allowed the subject to gradually improve their self regulation skills and achieve a more consistent mental task execution. For example, the preparatory source CSP analysis for the last several sessions resulted in spatial filters corresponding to the physiological expectations about the origins of ERD/ERS effects. Figure 6.12 contains the source CSP filters corresponding to the highest ranked features for different classes, shown over the cortical surface mesh. These filters were obtained using the data from the last 5 training sessions. The spatial distributions of filter weights resemble the CSPs that were produced from trials in BCI competition IV dataset 2a (see figure 5.9). It is important to note that within this work the application of heuristic ROI (shown on figure 6.9) did not significantly affect the classification performance in real-time sessions, as the CSP filters generally pointed at the regions
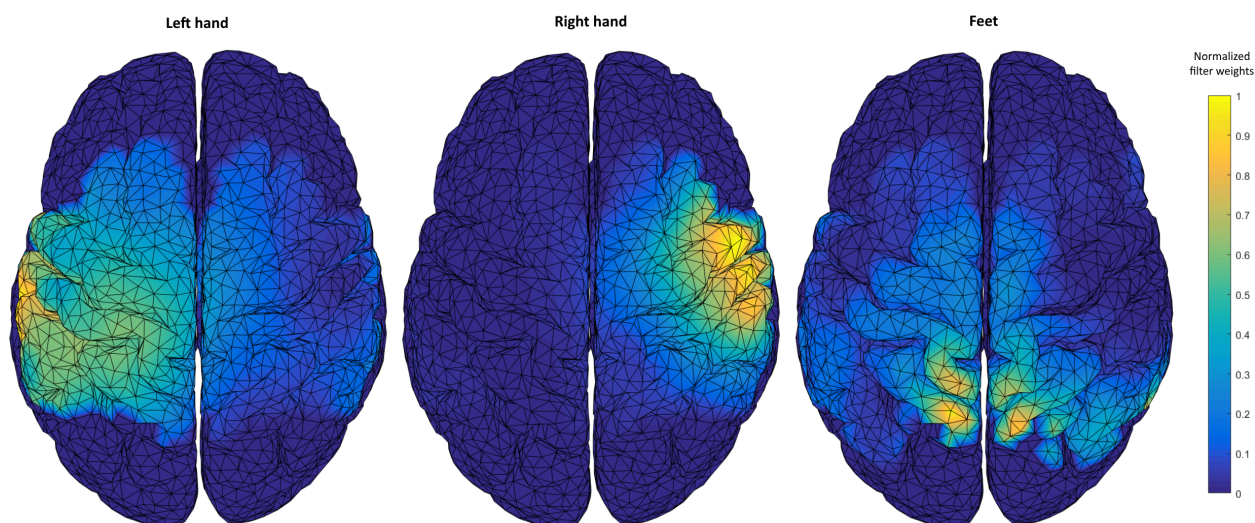
FIGURE 6.12: The most desirable CSP filters for all three classes of data. Distribution topographies of the normalized filter weights are shown in color over the standard cortical surface.

around central sulcus and parietal lobe. It was applied mainly to reduce the dimensionality of source data, and thus facilitate the real-time implementation of the proposed system.

The effect of continuous training on the BCI generalization performance can be illustrated by the classifier training/evaluation procedure, similar to that described in chapter 5 section 5.1.3. Such analysis was applied to all 40 available recordings from subject 2, where each recording contained 5-8 level runs. Within the evaluation process trials from each recording were classified using the SVMs trained by the four preceding recordings, which is identical to the data selection approach used to prepare for each feedback session. Generalization accuracy here was defined as the percentage of correctly predicted trials. By repeating this procedure for all recording files starting from the fifth we have acquired the dynamics of BCI generalization capabilities throughout the training course. Graphs in figure 6.13 show the results of such an evaluation procedure for both PSD and source CSP feature extraction methods. In addition to that, after each of the 8 latest training sessions with source CSP BCI supplementary trial-based recordings of motor imagery were made
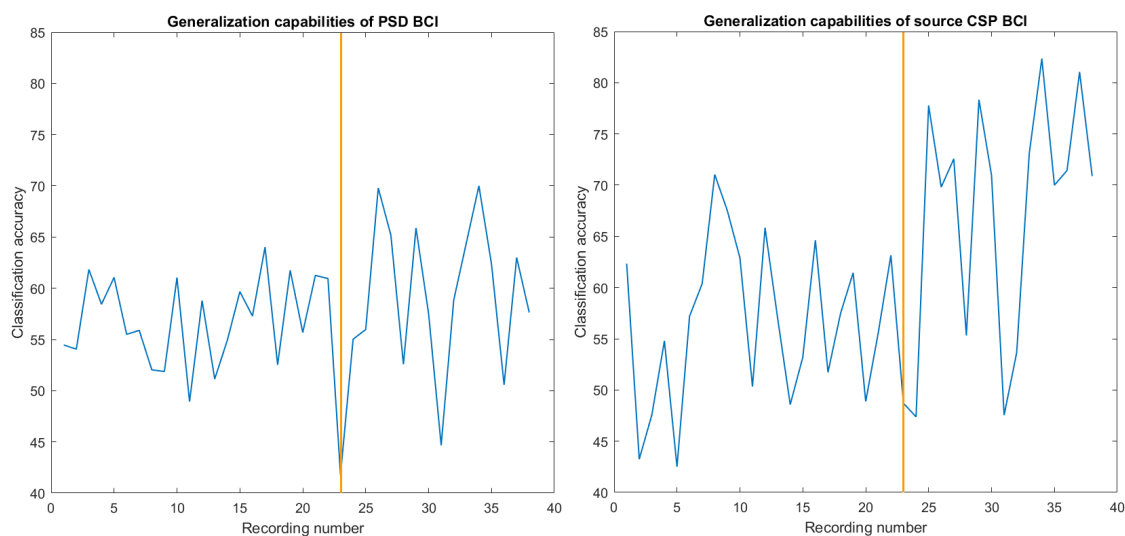
FIGURE 6.13: Classifier generalization test applied to the available recordings from feedback training sessions. The vertical orange line denotes the first training session with source CSP BCI.

for subject 2. A similar evaluation procedure to that described previously was performed by training a single classifier with the latest data and then by using it to predict the trials from all available recordings. Figure 6.14 shows the results of such a generalization
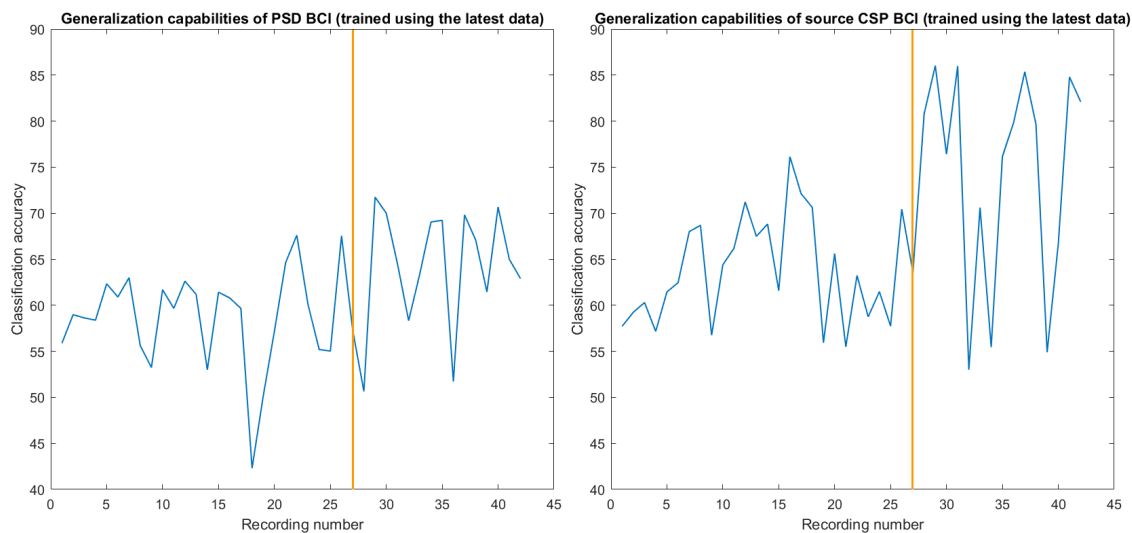
FIGURE 6.14: Classifier generalization test applied to the available recordings from feedback training sessions using the latest recorded data. The vertical orange line denotes the first training session with source CSP BCI.

test for PSD and for source CSP classifiers.

The figures 6.13 and 6.14 show that source CSP features performed better with an experienced BCI user and achieved the highest generalization accuracy, while the PSD features were generally more separable when the user was untrained. Because only short time segments at the border of task cues were used for feature extraction, such analysis does not reflect the BCI performance during the whole duration of level and figure 6.11 gives a better idea of the overall training progression.

Figures 6.11, 6.13 and 6.14 illustrate the fact that the BCI performance varied significantly even in the later stages of training with source CSP features. The shortest run times in BrainRunners (in figure 6.11), as well as the highest peaks in generalization accuracy (in figures 6.13 - 6.14) were achieved when only the EEG data from the same day was used to train the BCI classifiers. There are two major factors that may explain this observed effect. First, it is the general inter-session variability of user BCI control signals - besides the day-to-day changes in mood and concentration, at every new recording session the subjects also tried to adapt their motor imagery commands to achieve better results in BrainRunners. Secondly, despite our efforts to keep the EEG electrode positioning constant between the training sessions, there was still some inevitable degree of inconsistency, since the EEG location digitizer was not utilized during recordings. Such a discrepancy in electrode positioning can be interpreted as a forward modelling error, which causes a certain distortion bias in source reconstruction results as was explained in section 3.5.3 of this thesis. Intuitively this means that every separate recording session had a different distortion bias which did not affect the BCI performance as long as only the observations from a single recording session was used. Potentially this effect could have been alleviated by implementing a more appropriate feature normalization method.

Although subject 1 had to discontinue the training course and did not achieve reliable control of BCI, the work conducted with him highlighted various important aspects of practical BCI development for the quadriplegic users. Achieving a robust signal quality at the recording sessions was a challenging task, due to the amount artifacts and noise contaminating the EEG. Although subject 1 has lost

his ability for body perception and control below the neck, his body was affected by periodical strong spasms, which overwhelmed the signal for up to 10 seconds. Besides that, the lack of spine control means that his posture in the wheelchair was maintained mainly by the strap belts and by his neck. The constant tension of neck muscles that are so close to the EEG electrodes strongly interfered with the recorded signal and discouraged us from use of several posterior electrodes. Considering these challenges and the observed benefits of source reconstruction for noise reduction, the application of source BCI for real-time feedback training represents a reasonable direction for further work on practical assistive BCIs for disabled users.

Chapter 7

Thesis summary and conclusions.

7.1   Summary.

This PhD thesis has been aimed at the development of motor imagery BCIs that incorporate general knowledge about head anatomy and biophysics of EEG generation. First of all, the design process was guided by the definition of the signal of interest, i.e., characterization of physical effects indicative of brain state. In section 1.3.2 it was stated that imagination of movement is generally associated with modulation of sensorymotor rhythms in the mu and beta bands of the EEG. Kinesthetic imagery of limb movement generates spatial patterns of ERD/ERS effects occurring predominantly in the primary somatosensory cortex (S1). Spatial segregation of brain areas responsible for kinesthetic perception of different muscles makes it possible to identify the type of motor imagery from the patterns of ERD/ERS effects associated with muscles involved in mental tasks.

In general our approach to motor imagery classification is based on the locking of ERD/ERS effects in time, frequency and space. Locking in time is represented by the selection of a time window in offline analysis or the definition of a sliding window in real-time EEG processing. In the frequency domain of the signal the indicative bands are selected according to the class separation capabilities of features extracted from these bands. The spatial patterns of signal of interest are captured by the CSP spatial filters, estimated in a data-driven manner from the available observations. The CSP filters

employed in the EEG processing scheme largely define the classification accuracy and overall BCI performance. An overview of methods for EEG preprocessing, feature extraction, selection and classification algorithms that are generally employed in EEG BCI analysis, is given in chapter 2.

Since spatial properties of the characteristic signal are crucial for mental task interpretation, accentuation of such features leads to an improvement in motor imagery classification. For this purpose in our proposed BCI system the electromagnetic source reconstruction has been employed, which is the centerpiece of this research. In EEG source analysis the scalp electrode data is represented as a linear instantaneous superposition of electric fields generated by sources at multiple points spanning the cortical surface. Chapter 3 is dedicated to the forward problem of source localization, which aims to estimate the degree of coupling between brain cortical currents and the resulting scalp potentials that are measured by the EEG. With respect to the biophysics of EEG generation the individual sources are typically modelled as current dipoles, and given the source grid definition, head geometry and co-registered electrode coordinates it is possible to calculate the forward coupling through the application of a particular numerical method such as BEM or FEM.

With the forward source-electrode coupling formulated as a lead field matrix, it is possible to solve the inverse problem of EEG source localization, in other words, find a combination of active dipole sources that realistically explains the observed EEG. Since typically the number of dipole sources largely exceeds the number of EEG channels, the inverse problem is ill-posed, so a unique solution can only be found by incorporating additional constraints. Chapter 4 gives an overview of commonly applied inverse solutions and characterizes an EEG imaging system with regard to its resolution and spatial decorrelation capabilities based on simulation case studies.

Source representation of EEG is the signal domain comprised by multiple linear combinations of the original sensor data. The number of such combinations is defined by the dimensionality of source model and their validity is justified by the assumptions utilized in

forward modelling and inverse operator calculation. It may be speculated that after the source reconstruction stage the BCI feature extraction, selection and classification methods that aim to discriminate the data based on its spatial properties operate in a more natural domain, considering the anatomical segregation of functional brain areas. This rationale is what lies behind the proposed EEG signal processing system examined in chapter 5 based on the offline BCI analysis scenario from BCI competition IV. This novel approach extends the conventional CSP feature extraction method to source analysis. The results show that classification of motor imagery data in source space from 9 subjects yielded an evident improvement in accuracy compared to the conventional sensor-based methods.

In chapter 6 the proposed approach for motor imagery classification was applied in a real-time BCI system with visual feedback. This work was focused on achieving the highest possible BCI performance in a computer game designed for Cybathlon 2016 BCI race. Generally within the BCI user training process there are two co-adaptive entities - the BCI user, who gradually improves the consistency of BCI control commands, and the BCI classifier, which must adapt to these changes. Over the course of six months we have gradually built up BCIs based on different signal processing principles and employed them in more than 47 recording and feedback training sessions with two subjects, a quadriplegic adult patient and a healthy adult. Although the training process did not always result in progressive BCI performance improvement, the application of source-based motor imagery classification in the later training stages yielded an immediate increase in BCI reliability and responsiveness.

7.2 Conclusions.

In this PhD manuscript EEG signal processing and classification techniques applicable to real-time control BCI applications have been studied. The work was conducted with three main objectives:

1. Design an EEG BCI signal processing and classification system employing background knowledge about biophysics and EEG signal generation.

2. Investigate the effects of source reconstruction on indicative signal features in EEG BCIs based on imagination of movement.

3. Validate the performance of the proposed source analysis approach with practical real-time motor imagery BCI implementation.

Regarding objective 1, the source analysis utilized in the proposed BCI signal processing scheme employs background knowledge about the generation of EEG signal and propagation of electric fields in the head volume. Forward head modelling necessary for source localization relies on human anatomy (head geometry), neurophysiological origins of EEG (source model) and properties of electric field propagation (used in BEM/FEM/FDM). Besides that, additional neurophysiological assumptions such as sparsity, minimal energy, local autoregressive source coupling or multimodal priors are generally expressed in the form of functional constraints that define a certain type of inverse solution. Altogether this results in a flexible EEG imaging system capable of continuous cortical current monitoring, that can be customized to a particular subject.

Objective 2 was the focus of work described in chapter 5. Benefits of source analysis for BCI reliability were validated on motor imagery data from 9 subjects. Compared to conventional sensor-based feature extraction methods the application of source localization in the BCI signal processing scheme resulted in improved motor imagery classification accuracy for all subjects in the dataset. More specifically, source reconstruction reduced the degree of linear dependence between the signal components, and spatially segregated these components based on their cortical origin. In addition, it was shown that source reconstruction and subsequent ROI extraction reduces the influence of noise and artifacts on the extracted CSP features, which is more flexible and efficient than simple channel selection. As a result the obtained source FBCSP features provided for better class separability, i.e., more efficient encoding of the ERD/ERS effects indicative of motor imagery type. Our results show that by utilizing knowledge about EEG physics it is possible to achieve superior brain activity interpretation accuracy even with low-density

EEG montages, and without subject-specific anatomical head models.

Finally, the advantages of proposed approach were verified based on a real-time BCI training study, which corresponds to objective 3. The training process aimed at achieving the highest possible BCI reliability in a 3-state classification paradigm. Although the proposed BCI design was utilized in real-time sessions with only one subject, its incorporation in the training process yielded an immediate increase in BCI performance. Considering the low SNR of dry electrode EEG and its high susceptibility to artifacts, our results show that real-time EEG source analysis is applicable and advantageous in practical control BCI applications outside the laboratory settings.

7.3 Future work.

Based on the work with source BCI described in chapter 6 it is possible to identify directions for further work, which could improve the ease of use and validate our findings:

1. **Idle state implementation**. Cybathlon 2016 BCI race implied the availability of an idle state, when no BCI control command must be sent to the application. Considering the voluntary, endogenous nature of control command generation, implementation of an idle state in motor imagery BCIs is a challenging task that has become a separate niche in BCI research (Zhang et al. 2007; Dyson et al. 2009; Lee et al. 2015). Given the robust idle state detection our proposed BCI system could be applied to traditional control applications such as mouse movement or text input. Idle state detection was tried in early training sessions, however at that point it significantly hindered the classification of other BCI commands. Further work in this area suggests the continuation of feedback training specifically focused on achieving robust idle state detection.

2. **Implementation of visual feedback based on real-time EEG imaging**. Within the employed BCI training paradigm a simple indication of successful BCI command execution was given

by the Brainrunners game. From the user perspective identifying a productive strategy for mental task execution requires a more informative visual feedback that gives additional details about resulting brain activity rather than a simple binary indication. In this context, by providing the opportunity for individuals to monitor their own cortical activity during BCI command execution it is possible to more efficiently employ their cognitive abilities and as a result reduce the training times. Advantages of such visual feedback were recently investigated in MEG-based BCI training ((Florin, Bock, and Baillet 2014)) and in EEG BCIs (Ahn, Cho, and Jun 2011).

3. **Comparative study with multiple subjects**. The work described in chapter 6 involved BCI training of only two individuals and the proposed source-based BCI was applied to only one of them. Besides, the BCI employed in feedback sessions was being developed and tested in parallel with the training course. Due to that the training protocol was often modified from session to session. Although the use of source-based BCI resulted in immediate reliability increase, a comprehensive study involving multiple subjects and standardized session protocol is necessary for a more thorough validation of the proposed design.

In the context of BCI design in general EEG neuroimaging represents a versatile technique that can serve as a basis for more advanced functional modelling and feature extraction approaches. Based on recent publications it is possible to identify some promising directions in BCI research that employ EEG source localization:

1. **Hybrid BCIs.** Although EEG offers a number of advantages that makes it the preferred signal modality for BCI applications, it suffers from low SNR and spatial resolution, which limits the BCI performance. After source reconstruction the variables representing the observed EEG have multiple associated parameters, such as cortical location, orientation and list of neighbor sources. Given such parametrization it is possible to utilize measurements from other neuroimaging modalities such as fMRI or fNIRS, where data points are also defined in a

brain volume. According to recent research hybrid multimodal BCIs can significantly reduce the motor imagery training times and improve the classification reliability or allow for a larger number of BCI commands (Pfurtscheller et al. 2010; Fazli et al. 2012; Amiri et al. 2013).

2. **Finer, more natural BCI control commands**. Traditionally motor imagery BCIs rely on the functional segregation of muscle-specific somatosensory cortex regions for mental task selection. Although such an approach improves the class separability of motor imagery data in general, it creates a certain cognitive disconnection between the desirable action (mouse movement, wheelchair control) and the mental task that has to be performed (imaginary hand, feet movement), which hinders the BCI usability. Spatial resolution enhancement offered by source reconstruction allows for selection of finer and more natural control mental tasks, such as kinesthetic imagery of individual finger movement instead of whole limb motion. Preliminary research in this direction is described, for example, in (Edelman, Baxter, and He 2015; Edelman, Baxter, and He 2016).

3. **Brain connectivity for mental state detection.** The source variables calculated by the various EEG imaging techniques have associated spatial and orientation properties. Conventional feature extraction methods such as PSD or CSP generally represent the data in terms of some fundamental properties such as band power or spatial distribution of variance. Much like our proposed feature extraction method, EEG brain connectivity analysis also operates in source space and hence, generally requires source reconstruction as a preparatory step. However, within the framework of functional brain connectivity the nodes of the source model are generally allocated to functional brain regions (e.g., primary motor cortex, primary somatosensory cortex). Functional relationships between these segregated neuronal systems, which are in the focus of brain connectivity analysis, can be estimated from the complex patterns of information flow between these cortical areas. Based on information theoretic parameters, directed coherence, phase synchrony and

other metrics, these connectivity indices quantify the hidden properties of EEG data which have been shown to be beneficial for the task of motor imagery classification (Billinger, Brunner, and Müller-Putz 2013; Liang et al. 2016; Zhang, Chavarriaga, and Millán 2014). As opposed to the traditional BCI feature extraction techniques, brain connectivity features represent the semantics of the EEG signal rather than its fundamental physical properties.

Bibliography

Acar, Zeynep Akalin and Scott Makeig (2013). "Effects of forward model errors on EEG source localization". In: *Brain topography* 26.3, pp. 378–396 (cit. on p. 97).

Ahn, Minkyu, Hohyun Cho, and Sung Chan Jun (2011). "Calibration time reduction through source imaging in brain computer interface (BCI)". In: *International Conference on Human-Computer Interaction*. Springer, pp. 269–273 (cit. on p. 170).

Ahn, Minkyu et al. (2013). "Gamma band Activity Associated with BCI Performance: Simultaneous MEG/EEG Study". In: *Frontiers in Human Neuroscience* 7.December, p. 848 (cit. on p. 37).

Ahn, Minkyu et al. (2014). "A review of brain-computer interface games and an opinion survey from researchers, developers and users". In: *Sensors* 14.8, pp. 14601–14633 (cit. on p. 23).

Akhtar, MUhammad Tahir et al. (2012). "Recursive independent component analysis for online blind source separation". In: *2012 IEEE International Symposium on Circuits and Systems*. IEEE, pp. 2813–2816 (cit. on p. 50).

Alfred, Mertins (1999). *Signal Analysis Wavelets, Filter Banks, Time-Frequency Transforms and Applications*. John Wiley and Sons, New York (cit. on p. 56).

Alhaddad, Mohammed J (2012). "Common average reference (car) improves p300 speller". In: *International Journal of Engineering and Technology* 2.3, p. 21 (cit. on p. 47).

Aloise, F et al. (2007). "Multimodal stimulation for a P300-based BCI". In: *Int. J. Bioelectromagn* 9, pp. 128–130 (cit. on p. 25).

Amiri, Setare et al. (2013). "A review of P300, SSVEP, and hybrid P300/SSVEP brain-computer interface systems". In: *Brain-Computer Interface Systems—Recent Progress and Future Prospects* (cit. on pp. 26, 27, 171).

Ang, Kai Keng and Cuntai Guan (2016). "EEG-based strategies to detect motor imagery for control and rehabilitation". In: *IEEE Transactions on Neural Systems and Rehabilitation Engineering* (cit. on p. 22).

Ang, Kai Keng et al. (2012). "Filter bank common spatial pattern algorithm on BCI competition IV datasets 2a and 2b". In: *Frontiers in Neuroscience* MAR (cit. on pp. 45, 46, 61, 66).

Ans, Bernard, Jeanny Hérault, and Christian Jutten (1985). "Adaptive neural architectures: detection of primitives". In: *Proceedings of COGNITIVA* 85, pp. 593–597 (cit. on p. 50).

Argunsah, Ali Ozgur and Mujdat Cetin (2010). "AR-PCA-HMM approach for sensorimotor task classification in EEG-based brain-computer interfaces". In: *Pattern Recognition (ICPR), 2010 20th International Conference on*. IEEE, pp. 113–116 (cit. on p. 72).

Arvaneh, Mahnaz et al. (2011). "Optimizing the channel selection and classification accuracy in EEG-based BCI". In: *IEEE Transactions on Biomedical Engineering* 58.6, pp. 1865–1873 (cit. on p. 45).

Bach, F. R. and M. I. Jordan (2003). "Kernel independent component analysis". In: *Journal of Machine Learning Research* 3, pp. 1–48 (cit. on p. 50).

Baillet, S., J.C. Mosher, and R.M. Leahy (2001). "Electromagnetic brain mapping". In: *IEEE Signal Processing Magazine* 18.6. arXiv: 1053-5888 (cit. on pp. 18, 78, 82, 84, 88, 91).

Baillet, Sylvain (1998). "Toward functional brain imaging of cortical electrophysiology Markovian models for magneto and electroencephalogram source estimation and experimental assessments". In: *Orsay, France* (cit. on pp. 103, 109).

Balafar, Mohd Ali et al. (2010). "Review of brain MRI image segmentation methods". In: *Artificial Intelligence Review* 33.3, pp. 261–274 (cit. on p. 92).

Bashashati, Ali et al. (2007). "A survey of signal processing algorithms in brain–computer interfaces based on electrical brain signals". In: *Journal of Neural engineering* 4.2, R32 (cit. on p. 66).

Bashashati, Hossein et al. (2015). "Comparing different classifiers in sensory motor brain computer interfaces". In: *PloS one* 10.6, e0129435 (cit. on p. 66).

Bauer, Herbert and Avni Pllana (2014). "EEG-based local brain activity feedback training—tomographic neurofeedback". In: *Frontiers in human neuroscience* 8, p. 1005 (cit. on p. 141).

Bayford, Richard H and Bill R B Lionheart (2004). "Biomedical applications of electrical impedance tomography". In: *Physiological Measurement* 25.1 (cit. on p. 93).

Belkin, Mikhail, Jian Sun, and Yusu Wang (2008). "Discrete laplace operator on meshed surfaces". In: *Proceedings of the twenty-fourth annual symposium on Computational geometry*. ACM, pp. 278–287 (cit. on p. 105).

Bell, Anthony J and Terrence J Sejnowski (1995). "An information-maximization approach to blind separation and blind deconvolution". In: *Neural computation* 7.6, pp. 1129–1159 (cit. on p. 50).

Berger, Hans (1929). "Über das elektrenkephalogramm des menschen". In: *European Archives of Psychiatry and Clinical Neuroscience* 87.1, pp. 527–570 (cit. on pp. 17, 34).

Besserve, Michel, Jacques Martinerie, and Line Garnero (2011). "Improving quantification of functional networks with eeg inverse problem: Evidence from a decoding point of view". In: *NeuroImage* 55.4, pp. 1536–1547 (cit. on p. 141).

Bhattacharyya, Saugat et al. (2015). "A Review on Brain Imaging Techniques for BCI Applications". In: *Biomedical Image Analysis and Mining Techniques for Improved Health Outcomes*, p. 39 (cit. on p. 141).

Billinger, Martin, Clemens Brunner, and Gernot R Müller-Putz (2013). "Single-trial connectivity estimation for classification of motor imagery data." In: *Journal of neural engineering* 10.4, p. 046006 (cit. on p. 172).

Birbaumer, Niels et al. (2003). "The thought-translation device (TTD): neurobehavioral mechanisms and clinical outcome". In: *IEEE transactions on Neural Systems and rehabilitation engineering* 11.2, pp. 120–123 (cit. on p. 28).

Bishop, Christopher M (2006). *Pattern Recognition and Machine Learning*. Ed. by M Jordan, J Kleinberg, and B Schölkopf. Vol. 4. Information science and statistics 4. Springer. Chap. Graphical, p. 738. arXiv: 0-387-31073-8 (cit. on pp. 64, 131).

Blankertz, Benjamin et al. (2008). "Optimizing spatial filters for robust EEG single-trial analysis". In: *IEEE Signal Processing Magazine* 25.1, pp. 41–56 (cit. on p. 61).

Blankertz, Benjamin et al. (2010). "The Berlin brain–computer interface: non-medical uses of BCI technology". In: *Frontiers in neuroscience* 4, p. 198 (cit. on p. 23).

Blankertz, Benjamin et al. (2011). "Single-trial analysis and classification of ERP components—a tutorial". In: *NeuroImage* 56.2, pp. 814–825 (cit. on pp. 66, 68).

Blankertz, Benjamin et al. (2016). "The Berlin Brain-Computer Interface: Progress Beyond Communication and Control". In: *Frontiers in Neuroscience* 10 (cit. on p. 22).

Boostani, Reza et al. (2007). "A comparison approach toward finding the best feature and classifier in cue-based BCI". In: *Medical & biological engineering & computing* 45.4, pp. 403–412 (cit. on pp. 33, 51, 56, 149).

Borghini, Gianluca et al. (2014). *Measuring neurophysiological signals in aircraft pilots and car drivers for the assessment of mental workload, fatigue and drowsiness* (cit. on p. 24).

Boser, Bernhard E, Isabelle M Guyon, and Vladimir N Vapnik (1992). "A training algorithm for optimal margin classifiers". In: *Proceedings of the fifth annual workshop on Computational learning theory*. ACM, pp. 144–152 (cit. on pp. 68, 71).

Brouwer, Anne-Marie and Jan BF Van Erp (2010). "A tactile P300 brain-computer interface". In: *Frontiers in neuroscience* 4, p. 19 (cit. on p. 25).

Brown, Gavin et al. (2012). "Conditional likelihood maximisation: a unifying framework for information theoretic feature selection". In: *Journal of Machine Learning Research* 13.Jan, pp. 27–66 (cit. on p. 64).

Brunner, C et al. (2008). "BCI Competition 2008–Graz data set A". In: *Institute for Knowledge Discovery (Laboratory of Brain-Computer Interfaces), Graz University of Technology*, pp. 136–142 (cit. on pp. 20, 121, 122).

Brunner, Clemens et al. (2011). "A comparison of univariate, vector, bilinear autoregressive, and band power features for brain–computer interfaces". In: *Medical & biological engineering & computing* 49.11, pp. 1337–1346 (cit. on pp. 33, 51).

Brunner, Clemens et al. (2015). "BNCI Horizon 2020: towards a roadmap for the BCI community". In: *Brain-computer interfaces* 2.1, pp. 1–10 (cit. on p. 22).

Buccino, Alessio Paolo, Hasan Onur Keles, and Ahmet Omurtag (2016). "Hybrid EEG-fNIRS asynchronous brain-computer interface for multiple motor tasks". In: *PLoS ONE* 11.1 (cit. on p. 40).

Carlson, Tom and Jose del R Millan (2013). "Brain-controlled wheelchairs: a robotic architecture". In: *IEEE Robotics & Automation Magazine* 20.1, pp. 65–73 (cit. on p. 22).

Cecotti, Hubert (2010). "Classification of steady-state visual evoked potentials based on the visual stimuli duty cycle". In: *2010 3rd International Symposium on Applied Sciences in Biomedical and Communication Technologies (ISABEL 2010)*. IEEE, pp. 1–5 (cit. on p. 66).

Cecotti, Hubert and Axel Graeser (2008). "Convolutional neural network with embedded fourier transform for EEG classification". In: *Pattern Recognition, 2008. ICPR 2008. 19th International Conference on*. IEEE, pp. 1–4 (cit. on p. 75).

Cecotti, Hubert and Axel Graser (2011). "Convolutional neural networks for P300 detection with application to brain-computer interfaces". In: *IEEE transactions on pattern analysis and machine intelligence* 33.3, pp. 433–445 (cit. on p. 75).

Chang, Wei-Tang et al. (2015). "Combined MEG and EEG show reliable patterns of electromagnetic brain activity during natural viewing." In: *NeuroImage* 114, pp. 49–56 (cit. on p. 37).

Cheng, Alexander H-D and Daisy T Cheng (2005). "Heritage and early history of the boundary element method". In: *Engineering Analysis with Boundary Elements* 29.3, pp. 268–302 (cit. on p. 96).

Cincotti, Febo et al. (2003). "Comparison of different feature classifiers for brain computer interfaces". In: *Neural Engineering, 2003. Conference Proceedings. First International IEEE EMBS Conference on*. IEEE, pp. 645–647 (cit. on p. 72).

Cincotti, Febo et al. (2008). "Non-invasive brain–computer interface system: towards its application as assistive technology". In: *Brain research bulletin* 75.6, pp. 796–803 (cit. on p. 22).

Clerc, Maureen et al. (2010). "The symmetric BEM: bringing in more variables for better accuracy". In: *17th International Conference on Biomagnetism Advances in Biomagnetism–Biomag2010*. Springer, pp. 109–112 (cit. on p. 111).

Coan, James A and John JB Allen (2004). "Frontal EEG asymmetry as a moderator and mediator of emotion". In: *Biological psychology* 67.1, pp. 7–50 (cit. on p. 61).

Collinger, Jennifer L et al. (2013). "Functional priorities, assistive technology, and brain-computer interfaces after spinal cord injury". In: *Journal of rehabilitation research and development* 50.2, p. 145 (cit. on p. 23).

Collins, D Louis et al. (1999). "ANIMAL+ INSECT: improved cortical structure segmentation". In: *Biennial International Conference on Information Processing in Medical Imaging*. Springer, pp. 210–223 (cit. on pp. 97, 110).

Congedo, Marco, Fabien Lotte, and Anatole Lécuyer (2006). "Classification of movement intention by spatially filtered electromagnetic inverse solutions". In: *Physics in medicine and biology* 51.8, p. 1971 (cit. on p. 141).

Congedo, Marco, Joel F Lubar, and David Joffe (2004). "Low-resolution electromagnetic tomography neurofeedback". In: *IEEE Transactions on Neural Systems and Rehabilitation Engineering* 12.4, pp. 387–397 (cit. on p. 141).

Cooley, James W and John W Tukey (1965). "An algorithm for the machine calculation of complex Fourier series". In: *Mathematics of computation* 19.90, pp. 297–301 (cit. on p. 44).

Coyle, Damien, T Martin McGinnity, and Girijesh Prasad (2010). "Improving the separability of multiple EEG features for a BCI by neural-time-series-prediction-preprocessing". In: *Biomedical Signal Processing and Control* 5.3, pp. 196–204 (cit. on p. 73).

Coyle, Shirley et al. (2004). "On the suitability of near-infrared (NIR) systems for next-generation brain-computer interfaces." In: *Physiological measurement* 25.4, pp. 815–822 (cit. on pp. 39, 40).

Coyle, Shirley M, Tomás E Ward, and Charles M Markham (2007). "Brain-computer interface using a simplified functional near-infrared spectroscopy system." In: *Journal of neural engineering* 4.3, pp. 219–26 (cit. on p. 40).

Curran, Eleanor A and Maria J Stokes (2003). "Learning to control brain activity: a review of the production and control of EEG components for driving brain–computer interface (BCI) systems". In: *Brain and cognition* 51.3, pp. 326–336 (cit. on p. 148).

Dabek, Juhani et al. (2016). "Determination of head conductivity frequency response in vivo with optimized EIT-EEG". In: *NeuroImage* 127, pp. 484–495 (cit. on p. 93).

Daly, Janis J and Jonathan R Wolpaw (2008). "Brain–computer interfaces in neurological rehabilitation". In: *The Lancet Neurology* 7.11, pp. 1032–1043 (cit. on p. 22).

Dang, Hung V and Kwong T Ng (2011). "Finite difference neuroelectric modeling software". In: *Journal of neuroscience methods* 198.2, pp. 359–363 (cit. on p. 96).

Daubechies, Ingrid (1990). "The wavelet transform, time-frequency localization and signal analysis". In: *IEEE transactions on information theory* 36.5, pp. 961–1005 (cit. on p. 59).

Davis, Geoff, Stephane Mallat, and Marco Avellaneda (1997). "Adaptive greedy approximations". In: *Constructive approximation* 13.1, pp. 57–98 (cit. on p. 108).

Dornhege, Guido et al. (2004). "Boosting bit rates in noninvasive EEG single-trial classifications by feature combination and multiclass paradigms". In: *IEEE Transactions on Biomedical Engineering* 51.6, pp. 993–1002 (cit. on p. 52).

Dyson, Matthew et al. (2009). "Sequential classification of mental tasks vs. idle state for EEG based BCIs". In: *2009 4th International IEEE/EMBS Conference on Neural Engineering*. IEEE, pp. 351–354 (cit. on p. 169).

Edelman, Brad, Bryan Baxter, and Bin He (2015). "Decoding and mapping of right hand motor imagery tasks using EEG source imaging". In: *2015 7th International IEEE/EMBS Conference on Neural Engineering (NER)*. IEEE, pp. 194–197 (cit. on p. 171).

Edelman, Bradley J, Bryan Baxter, and Bin He (2016). "EEG Source Imaging Enhances the Decoding of Complex Right-Hand Motor

Imagery Tasks". In: *IEEE Transactions on Biomedical Engineering* 63.1, pp. 4–14 (cit. on p. 171).

Efron, Bradley et al. (2004). "Least angle regression". In: *The Annals of statistics* 32.2, pp. 407–499 (cit. on p. 108).

Fang, Qianqian and David A Boas (2009). "Tetrahedral mesh generation from volumetric binary and grayscale images". In: *2009 IEEE International Symposium on Biomedical Imaging: From Nano to Macro*. IEEE, pp. 1142–1145 (cit. on p. 110).

Fazli, Siamac et al. (2012). "Enhanced performance by a hybrid NIRS-EEG brain computer interface". In: *NeuroImage* 59.1, pp. 519–529 (cit. on pp. 40, 171).

Felzer, Torsten and B Freisieben (2003). "Analyzing EEG signals using the probability estimating guarded neural classifier". In: *IEEE Transactions on Neural Systems and Rehabilitation Engineering* 11.4, pp. 361–371 (cit. on p. 74).

Fisher, Ronald A (1936). "The use of multiple measurements in taxonomic problems". In: *Annals of eugenics* 7.2, pp. 179–188 (cit. on pp. 66, 67).

Florin, Esther, Elizabeth Bock, and Sylvain Baillet (2014). "Targeted reinforcement of neural oscillatory activity with real-time neuroimaging feedback". In: *Neuroimage* 88, pp. 54–60 (cit. on p. 170).

Fonov, Vladimir et al. (2011). "Unbiased average age-appropriate atlases for pediatric studies". In: *NeuroImage* 54.1, pp. 313–327 (cit. on pp. 97, 110).

Fonov, Vladimir S et al. (2009). "Unbiased nonlinear average age-appropriate brain templates from birth to adulthood". In: *NeuroImage* 47, S102 (cit. on pp. 97, 110).

Friston, Karl J (2011). "Functional and effective connectivity: a review". In: *Brain Connectivity* 1.1, pp. 13–36 (cit. on p. 77).

Frolov, AA et al. (2017). "PRINCIPLES OF MOTOR RECOVERY IN POST-STROKE PATIENTS USING HAND EXOSKELETON CONTROLLED BY THE BRAIN-COMPUTER INTERFACE BASED ON MOTOR IMAGERY". In: *Neural Network World* 107, p. 137 (cit. on p. 23).

Frolov, Alexander et al. (2013). "Sources of electrical brain activity most relevant to performance of brain-computer interface based

on motor imagery". In: *Brain-Computer Interface Systems-Recent Progress and Future Prospects*, pp. 175–193 (cit. on p. 141).

Future BNCI Project (2012). *A Roadmap for Future Directions in Brain / Neuronal Computer Interaction Research*. Tech. rep. (cit. on p. 35).

Galway, Leo et al. (2015). "The Potential of the Brain-Computer Interface for Learning: A Technology Review". In: *Computer and Information Technology; Ubiquitous Computing and Communications; Dependable, Autonomic and Secure Computing; Pervasive Intelligence and Computing (CIT/IUCC/DASC/PICOM), 2015 IEEE International Conference on*. IEEE, pp. 1554–1559 (cit. on p. 23).

Gao, Jun Feng et al. (2010). "Automatic removal of eye-movement and blink artifacts from EEG signals". In: *Brain topography* 23.1, pp. 105–114 (cit. on p. 50).

Garipelli, Gangadhar, Ricardo Chavarriaga, and José del R Millán (2013). "Single trial analysis of slow cortical potentials: a study on anticipation related potentials". In: *Journal of neural engineering* 10.3, p. 036014 (cit. on p. 29).

Garrett, Deon et al. (2003). "Comparison of linear, nonlinear, and feature selection methods for EEG signal classification". In: *IEEE Transactions on neural systems and rehabilitation engineering* 11.2, pp. 141–144 (cit. on p. 33).

Gerjets, Peter et al. (2015). "Cognitive state monitoring and the design of adaptive instruction in digital environments: lessons learned from cognitive workload assessment using a passive brain-computer interface approach". In: *Using Neurophysiological Signals that Reflect Cognitive or Affective State*, p. 20 (cit. on p. 23).

Golub, Gene H, Michael Heath, and Grace Wahba (1979). "Generalized cross-validation as a method for choosing a good ridge parameter". In: *Technometrics* 21.2, pp. 215–223 (cit. on p. 114).

Gonçalves, Sónia I et al. (2003). "In vivo measurement of the brain and skull resistivities using an EIT-based method and realistic models for the head". In: *IEEE Transactions on Biomedical Engineering* 50.6, pp. 754–767 (cit. on p. 93).

Goodfellow, Ian, Yoshua Bengio, and Aaron Courville (2016). *Deep Learning*. http://www.deeplearningbook.org. MIT Press (cit. on p. 74).

Gramfort, Alexandre et al. (2010). "OpenMEEG: opensource software for quasistatic bioelectromagnetics". In: *Biomedical engineering online* 9.1, p. 1 (cit. on p. 111).

Grant, Michael, Stephen Boyd, and Yinyu Ye (2008). *CVX: Matlab software for disciplined convex programming* (cit. on p. 114).

Grant, Michael C and Stephen P Boyd (2008). "Graph implementations for nonsmooth convex programs". In: *Recent advances in learning and control*. Springer, pp. 95–110 (cit. on p. 114).

Grech, Roberta et al. (2008). "Review on solving the inverse problem in EEG source analysis." In: *Journal of neuroengineering and rehabilitation* 5, p. 25 (cit. on pp. 103, 109, 114).

Grosse-Wentrup, Moritz and Martin Buss (2008). "Multiclass common spatial patterns and information theoretic feature extraction". In: *IEEE transactions on Biomedical Engineering* 55.8, pp. 1991–2000 (cit. on p. 61).

Hajinoroozi, Mehdi et al. (2015). "Feature extraction with deep belief networks for driver's cognitive states prediction from EEG data". In: *Signal and Information Processing (ChinaSIP), 2015 IEEE China Summit and International Conference on*. IEEE, pp. 812–815 (cit. on p. 75).

Hallez, Hans et al. (2007). "Review on solving the forward problem in EEG source analysis." In: *Journal of neuroengineering and rehabilitation* 4, p. 46 (cit. on pp. 78, 83, 86, 87, 91).

Hämäläinen, Matti S and Risto J Ilmoniemi (1994). "Interpreting magnetic fields of the brain: minimum norm estimates". In: *Medical & biological engineering & computing* 32.1, pp. 35–42 (cit. on pp. 104, 109).

Hansen, Per Christian (1999). *The L-curve and its use in the numerical treatment of inverse problems*. IMM, Department of Mathematical Modelling, Technical Universityof Denmark (cit. on p. 114).

Haselsteiner, Ernst and Gert Pfurtscheller (2000). "Using time-dependent neural networks for EEG classification". In: *IEEE transactions on rehabilitation engineering* 8.4, pp. 457–463 (cit. on p. 74).

Haufe, Stefan et al. (2011). "EEG potentials predict upcoming emergency brakings during simulated driving". In: *Journal of neural engineering* 8.5, p. 056001 (cit. on p. 23).

Hjorth, Bo (1970). "EEG analysis based on time domain properties". In: *Electroencephalography and clinical neurophysiology* 29.3, pp. 306–310 (cit. on p. 52).

Hoffmann, Ulrich et al. (2008). "An efficient P300-based brain–computer interface for disabled subjects". In: *Journal of Neuroscience methods* 167.1, pp. 115–125 (cit. on p. 66).

Hortal, Enrique et al. (2013). "Online classification of two mental tasks using a SVM-based BCI system". In: *Neural Engineering (NER), 2013 6th International IEEE/EMBS Conference on*. IEEE, pp. 1307–1310 (cit. on p. 71).

Hoshi, Y and M Tamura (1997). "Near-infrared optical detection of sequential brain activation in the prefrontal cortex during mental tasks." In: *NeuroImage* 5.4 Pt 1, pp. 292–7 (cit. on p. 40).

Hsu, Wei-Yen and Yung-Nien Sun (2009). "EEG-based motor imagery analysis using weighted wavelet transform features". In: *Journal of neuroscience methods* 176.2, pp. 310–318 (cit. on p. 59).

Hwang, Han-Jeong, Chang-Hwan Im, and Sun-Ae Park (2013). "Evaluation of feature extraction methods for motor imagery-based bcis in terms of robustness to slight changes of electrode locations". In: *Brain-Computer Interface (BCI), 2013 International Winter Workshop on*. IEEE, pp. 76–78 (cit. on p. 54).

Hyvärinen, Aapo, Juha Karhunen, and Erkki Oja (2004). *Independent component analysis*. Vol. 46. John Wiley & Sons (cit. on p. 50).

Hyvärinen, Aapo and Erkki Oja (1997). "A fast fixed-point algorithm for independent component analysis". In: *Neural Computation* 9(7), 1483–1492 (cit. on p. 50).

Jia, Yangqing et al. (2014). "Caffe: Convolutional Architecture for Fast Feature Embedding". In: *arXiv preprint arXiv:1408.5093* (cit. on pp. 74, 75).

Jöbsis, F F (1977). "Noninvasive, infrared monitoring of cerebral and myocardial oxygen sufficiency and circulatory parameters." In: *Science* 198.4323, pp. 1264–1267 (cit. on p. 38).

Jung, Tzyy-Ping et al. (2000). "Removal of eye activity artifacts from visual event-related potentials in normal and clinical subjects". In: *Clinical Neurophysiology* 111.10, pp. 1745–1758 (cit. on p. 50).

Kaiser, Vera et al. (2014). "Cortical effects of user training in a motor imagery based brain-computer interface measured by fNIRS and EEG". In: *NeuroImage* 85, pp. 432–444 (cit. on pp. 30, 77).

Kaper, Matthias et al. (2004). "BCI competition 2003-data set IIb: support vector machines for the P300 speller paradigm". In: *IEEE Transactions on Biomedical Engineering* 51.6, pp. 1073–1076 (cit. on p. 71).

Kauhanen, Laura et al. (2006). "EEG and MEG brain-computer interface for tetraplegic patients". In: *IEEE Transactions on Neural Systems and Rehabilitation Engineering*. Vol. 14. 2, pp. 190–193 (cit. on p. 37).

Khan, M Jawad, Melissa Jiyoun Hong, and Keum-Shik S Hong (2014). "Decoding of four movement directions using hybrid NIRS-EEG brain-computer interface". In: *Frontiers in human neuroscience* 8.1 APR, p. 244 (cit. on p. 40).

Khorshidtalab, A and Momoh Jimoh Emiyoka Salami (2011). "EEG signal classification for real-time brain-computer interface applications: A review". In: *Mechatronics (ICOM), 2011 4th International Conference On*. IEEE, pp. 1–7 (cit. on p. 66).

Kirschstein, Timo and Rüdiger Köhling (2009). "What is the Source of the EEG?" In: *Clinical EEG and neuroscience* 40.3, pp. 146–149 (cit. on pp. 82, 83).

Koles, Zoltan J, Michael S Lazar, and Steven Z Zhou (1990). "Spatial patterns underlying population differences in the background EEG". In: *Brain topography* 2.4, pp. 275–284 (cit. on p. 61).

Krusienski, Dean J, Dennis J McFarland, and Jonathan R Wolpaw (2006). "An evaluation of autoregressive spectral estimation model order for brain-computer interface applications". In: *Engineering in Medicine and Biology Society, 2006. EMBS'06. 28th Annual International Conference of the IEEE*. IEEE, pp. 1323–1326 (cit. on pp. 52, 57).

— (2012). "Value of amplitude, phase, and coherence features for a sensorimotor rhythm-based brain–computer interface". In: *Brain research bulletin* 87.1, pp. 130–134 (cit. on pp. 54, 55).

Krusienski, Dean J et al. (2006). "A comparison of classification techniques for the P300 Speller". In: *Journal of neural engineering* 3.4, p. 299 (cit. on p. 66).

Kuhlman, William N (1978). "EEG feedback training: enhancement of somatosensory cortical activity". In: *Electroencephalography and clinical neurophysiology* 45.2, pp. 290–294 (cit. on p. 30).

Kybic, Jan et al. (2005). "A common formalism for the integral formulations of the forward EEG problem". In: *IEEE transactions on medical imaging* 24.1, pp. 12–28 (cit. on p. 111).

Lachaux, Jean-Philippe et al. (1999). "Measuring phase synchrony in brain signals". In: *Human brain mapping* 8.4, pp. 194–208 (cit. on p. 53).

Lal, Thomas Navin et al. (2005). "A Brain Computer Interface with Online Feedback based on Magnetoencephalography". In: *22Nd International Conference on Machine Learning*, pp. 465–472 (cit. on p. 37).

LeCun, Yann, Yoshua Bengio, and Geoffrey Hinton (2015). "Deep learning". In: *Nature* 521.7553, pp. 436–444 (cit. on pp. 74, 75).

Lederman, Dror and Joseph Tabrikian (2012). "Classification of multichannel EEG patterns using parallel hidden Markov models". In: *Medical & biological engineering & computing* 50.4, pp. 319–328 (cit. on p. 72).

Lee, Jong Hwan et al. (2009). "Brain-machine interface via real-time fMRI: Preliminary study on thought-controlled robotic arm". In: *Neuroscience Letters* 450.1, pp. 1–6 (cit. on p. 38).

Lee, Min-Ho et al. (2015). "Subject-dependent classification for robust idle state detection using multi-modal neuroimaging and data-fusion techniques in BCI". In: *Pattern Recognition* 48.8, pp. 2725–2737 (cit. on p. 169).

Li, Jing and Dandan Yan (2009). "Solving the EEG Forward Problem by FDM and FEM". In: *2009 2nd International Conference on Biomedical Engineering and Informatics*. IEEE, pp. 1–4 (cit. on p. 96).

Li, Yuanqing et al. (2010). "An EEG-based BCI system for 2-D cursor control by combining Mu/Beta rhythm and P300 potential". In: *IEEE Transactions on Biomedical Engineering* 57.10, pp. 2495–2505 (cit. on p. 70).

Liang, Shuang et al. (2016). "Discrimination of motor imagery tasks via information flow pattern of brain connectivity". In: *Technology and Health Care* Preprint, pp. 1–7 (cit. on p. 172).

Lin, Dongyu, Dean P Foster, and Lyle H Ungar (2010). "A risk ratio comparison of l0 and l1 penalized regressions". In: *Dept. Stat., Univ. Pennsylvania, Philadelphia, PA, USA, Tech. Rep* (cit. on p. 108).

Liu, JP, CX Zheng, and C Zhang (2009). "[Amplitude coupling analysis of EEG using nonlinear regressive coefficients during mental fatigue]." In: *Zhongguo yi liao qi xie za zhi= Chinese journal of medical instrumentation* 33.4, pp. 259–261 (cit. on p. 55).

Lotte, Fabien et al. (2007a). "A review of classification algorithms for EEG-based brain–computer interfaces". In: *Journal of neural engineering* 4.2, R1 (cit. on pp. 66, 70, 71).

Lotte, Fabien et al. (2007b). "Studying the use of fuzzy inference systems for motor imagery classification". In: *IEEE transactions on neural systems and rehabilitation engineering* 15.2, pp. 322–324 (cit. on p. 56).

Malmivuo, Jaakko and Robert Plonsey (1995). *Bioelectromagnetism: principles and applications of bioelectric and biomagnetic fields*. Oxford University Press, USA (cit. on pp. 35, 47).

Marchetti, Mauro and Konstantinos Priftis (2015). "Effectiveness of the P3-speller in brain–computer interfaces for amyotrophic lateral sclerosis patients: a systematic review and meta-analysis". In: *Interaction of BCI with the underlying neurological conditions in patients: pros and cons* (cit. on p. 26).

Marin, Gildas et al. (1998). "Influence of skull anisotropy for the forward and inverse problem in EEG: simulation studies using FEM on realistic head models". In: *Human brain mapping* 6.4, pp. 250–269 (cit. on p. 93).

Mason, S G et al. (2007). "A comprehensive survey of brain interface technology designs." In: *Annals of biomedical engineering* 35.2, pp. 137–169 (cit. on pp. 51, 52, 56, 65, 66, 72, 121, 149).

McFarland, Dennis J (2015). "The advantages of the surface Laplacian in brain–computer interface research". In: *International Journal of Psychophysiology* 97.3, pp. 271–276 (cit. on p. 48).

McFarland, Dennis J et al. (1997). "Spatial filter selection for EEG-based communication". In: *Electroencephalography and clinical Neurophysiology* 103.3, pp. 386–394 (cit. on pp. 47, 48).

Mellinger, J??rgen et al. (2007). "An MEG-based brain-computer interface (BCI)". In: *NeuroImage* 36.3, pp. 581–593 (cit. on p. 37).

Michel, Christoph M et al. (2004). "EEG source imaging". In: *Clinical neurophysiology* 115.10, pp. 2195–2222 (cit. on p. 106).

Miller, Erik G. and John W. Fisher III (2003). "Independent components analysis by direct entropy minimization". In: *Tech.Rep. UCB/CSD-03-1221* (cit. on p. 50).

Millett, David (2001). "Hans Berger: From psychic energy to the EEG". In: *Perspectives in biology and medicine* 44.4, pp. 522–542 (cit. on p. 34).

Mori, Hiromu et al. (2012). "Vibrotactile stimulus frequency optimization for the haptic BCI prototype". In: *Soft Computing and Intelligent Systems (SCIS) and 13th International Symposium on Advanced Intelligent Systems (ISIS), 2012 Joint 6th International Conference on*. IEEE, pp. 2150–2153 (cit. on p. 25).

Mori, Hiromu et al. (2013). "Multi-command tactile and auditory brain computer interface based on head position stimulation". In: *arXiv preprint arXiv:1301.6357* (cit. on p. 25).

Müller, Klaus-Robert et al. (2004). "Machine learning techniques for brain-computer interfaces". In: *Biomed. Tech* 49.1, pp. 11–22 (cit. on p. 68).

Muller, Klaus Robert et al. (2008). "Machine learning for real-time single-trial EEG-analysis: From brain-computer interfacing to mental state monitoring". In: *Journal of Neuroscience Methods* 167.1, pp. 82–90 (cit. on p. 24).

Munck, J C de and M J Peters (1993). "A fast method to compute the potential in the multisphere model." In: *IEEE transactions on bio-medical engineering* 40.11, pp. 1166–1174 (cit. on p. 95).

Najeeb, AR et al. (2016). "Review of Parameter Estimation Techniques for Time-Varying Autoregressive Models of Biomedical Signals". In: (cit. on p. 52).

Nakanishi, Masaki et al. (2014). "A high-speed brain speller using steady-state visual evoked potentials". In: *International journal of neural systems* 24.06, p. 1450019 (cit. on p. 27).

Nakayama, Kenji and Kiyoto Inagaki (2006). "A brain computer interface based on neural network with efficient pre-processing". In: *2006 International Symposium on Intelligent Signal Processing and Communications*. IEEE, pp. 673–676 (cit. on p. 73).

Naseer, Noman and Keum-Shik Hong (2015). "fNIRS-based brain-computer interfaces: a review." In: *Frontiers in human neuroscience* 9.January, p. 3 (cit. on pp. 39, 40).

Nicolas-Alonso, Luis Fernando and Jaime Gomez-Gil (2012). *Brain Computer Interfaces, a Review* (cit. on pp. 24, 25, 29, 32, 35, 52, 65, 66, 121).

Nijboer, Femke et al. (2008). "An auditory brain–computer interface (BCI)". In: *Journal of neuroscience methods* 167.1, pp. 43–50 (cit. on p. 25).

Nunez, Paul L and Ramesh Srinivasan (2006). *Electric fields of the brain: the neurophysics of EEG* (cit. on pp. 80, 83).

Nunez, PL et al. (1994). "A theoretical and experimental study of high resolution EEG based on surface Laplacians and cortical imaging". In: *Electroencephalography and clinical Neurophysiology* 90.1, pp. 40–57 (cit. on pp. 47, 48).

Obermaier, Bernhard et al. (2001a). "Hidden Markov models for online classification of single trial EEG data". In: *Pattern recognition letters* 22.12, pp. 1299–1309 (cit. on p. 53).

Obermaier, Bernhard et al. (2001b). "Information transfer rate in a five-classes brain-computer interface". In: *IEEE Transactions on neural systems and rehabilitation engineering* 9.3, pp. 283–288 (cit. on p. 72).

Oh, Seung-Hyeon, Yu-Ri Lee, and Hyoung-Nam Kim (2014). "A novel EEG feature extraction method using Hjorth parameter". In: *International Journal of Electronics and Electrical Engineering* 2.2, pp. 106–110 (cit. on p. 53).

Oostenveld, Robert et al. (2010). "FieldTrip: open source software for advanced analysis of MEG, EEG, and invasive electrophysiological data". In: *Computational intelligence and neuroscience* 2011 (cit. on pp. 96, 97).

Oppenheim, Alan V and Ronald W Schafer (2010). *Discrete-time signal processing*. Pearson Higher Education (cit. on p. 45).

Ortner, Rupert et al. (2010). "SSVEP based brain-computer interface for robot control". In: *International Conference on Computers for Handicapped Persons*. Springer, pp. 85–90 (cit. on p. 66).

Palaniappan, Ramaswamy (2006). "Utilizing gamma band to improve mental task based brain-computer interface design". In: *IEEE Transactions on Neural Systems and Rehabilitation Engineering* 14.3, pp. 299–303 (cit. on p. 61).

Palaniappan, Ramaswamy et al. (2002). "A new brain-computer interface design using fuzzy ARTMAP". In: *IEEE Transactions on Neural Systems and Rehabilitation Engineering* 10.3, pp. 140–148 (cit. on p. 74).

Pascual-Marqui, Roberto D, Christoph M Michel, and Dietrich Lehmann (1994). "Low resolution electromagnetic tomography: a new method for localizing electrical activity in the brain". In: *International Journal of psychophysiology* 18.1, pp. 49–65 (cit. on pp. 105, 109).

Pearson, Karl (1901). "On lines and planes of closest fit to systems of points in space". In: *The London, Edinburgh, and Dublin Philosophical Magazine and Journal of Science* 2.11, pp. 559–572 (cit. on p. 49).

Penny, William D et al. (2000). "EEG-based communication: a pattern recognition approach". In: *IEEE Transactions on Rehabilitation Engineering* 8.2, pp. 214–215 (cit. on p. 148).

Peralta Menendez, Rolando Grave de et al. (2004). "Electrical neuroimaging based on biophysical constraints". In: *Neuroimage* 21.2, pp. 527–539 (cit. on pp. 106, 109).

Pfurtscheller, G (1989). "Functional topography during sensorimotor activation studied with event-related desynchronization mapping". In: *Journal of Clinical Neurophysiology* 6.1, pp. 75–84 (cit. on p. 30).

Pfurtscheller, G et al. (2006). "Mu rhythm (de)synchronization and EEG single-trial classification of different motor imagery tasks." In: *NeuroImage* 31.1, pp. 153–159 (cit. on pp. 30, 77, 123).

Pfurtscheller, Gert and Christa Neuper (2001). "Motor imagery and direct brain-computer communication". In: *Proceedings of the IEEE* 89.7, pp. 1123–1134 (cit. on p. 56).

Pfurtscheller, Gert and FH Lopes da Silva (1999). "EEG event-related desynchronization (ERD) and event-related synchronization (ERS)". In: *Electroencephalography: basic principles, clinical applications and related fields*, 958 (cit. on p. 66).

Pfurtscheller, Gert et al. (2010). "The hybrid BCI". In: *Frontiers in neuroscience* 4, p. 3 (cit. on p. 171).

Pichiorri, F et al. (2011). "Sensorimotor rhythm-based brain–computer interface training: the impact on motor cortical responsiveness". In: *Journal of neural engineering* 8.2, p. 025020 (cit. on p. 154).

Pierce, John R (1980). "An introduction to information theory: Symbols". In: *Signals and Noise E* 2 (cit. on p. 18).

Pion-Tonachini, Luca et al. (2015). "Real-time EEG Source-mapping Toolbox (REST): Online ICA and source localization". In: *Engineering in Medicine and Biology Society (EMBC), 2015 37th Annual International Conference of the IEEE*. IEEE, pp. 4114–4117 (cit. on p. 50).

Plumbley, Mark D (2006). "Recovery of sparse representations by polytope faces pursuit". In: *International Conference on Independent Component Analysis and Signal Separation*. Springer, pp. 206–213 (cit. on p. 108).

Pocock, Adam and Gavin Brown (2016). *FEAST: A Feature Selection Toolbox for C and Matlab*. `http://mloss.org/software/view/386/` (cit. on p. 64).

R Millan, J et al. (2002). "A local neural classifier for the recognition of EEG patterns associated to mental tasks". In: *IEEE transactions on neural networks* 13.3, pp. 678–686 (cit. on p. 73).

Ramoser, Herbert, Johannes Müller-Gerking, and Gert Pfurtscheller (2000). "Optimal spatial filtering of single trial EEG during imagined hand movement". In: *IEEE Transactions on Rehabilitation Engineering* 8.4, pp. 441–446 (cit. on p. 62).

Regan, D (1979). "Electrical responses evoked from the human brain". In: *Sci. Am.* 241.6, pp. 134–146 (cit. on p. 47).

Ren, Yuanfang and Yan Wu (2014). "Convolutional deep belief networks for feature extraction of EEG signal". In: *Neural Networks (IJCNN), 2014 International Joint Conference on*. IEEE, pp. 2850–2853 (cit. on p. 75).

Robinson, Neethu et al. (2013). "EEG-based classification of fast and slow hand movements using wavelet-CSP algorithm". In: *IEEE Transactions on Biomedical Engineering* 60.8, pp. 2123–2132 (cit. on p. 59).

Roffo, Giorgio (2016). "Feature Selection Techniques for Classification: A widely applicable code library". In: *arXiv:1607.01327 [cs.CV]* (cit. on p. 64).

Rosas-Cholula, Gerardo et al. (2010). "On signal P-300 detection for BCI applications based on wavelet analysis and ICA preprocessing". In: *Electronics, Robotics and Automotive Mechanics Conference (CERMA), 2010*. IEEE, pp. 360–365 (cit. on p. 59).

Ruiz, Sergio et al. (2014). *Real-time fMRI brain computer interfaces: Self-regulation of single brain regions to networks* (cit. on p. 38).

Rupp, Rüdiger et al. (2014). "Brain–computer interfaces and assistive technology". In: *Brain-Computer-Interfaces in their ethical, social and cultural contexts*. Springer, pp. 7–38 (cit. on p. 22).

Sakkalis, V. (2011). "Review of advanced techniques for the estimation of brain connectivity measured with EEG/MEG". In: *Computers in Biology and Medicine* 41.12, pp. 1110–1117 (cit. on p. 77).

Salu, Y et al. (1990). "An improved method for localizing electric brain dipoles." In: *IEEE transactions on bio-medical engineering* 37.7, pp. 699–705 (cit. on p. 94).

Sanei, Saeid and J Chambers (2007). *EEG Signal Processing*. Ed. by Wiley. Vol. 1. January. Wiley-Blackwell. Chap. One, p. 289 (cit. on p. 80).

Schlögl, Alois et al. (2005). "Characterization of four-class motor imagery EEG data for the BCI-competition 2005". In: *Journal of neural engineering* 2.4, p. L14 (cit. on p. 71).

Schreuder, Martijn, Thomas Rost, and Michael Tangermann (2011). "Listen, you are writing! Speeding up online spelling with a dynamic auditory BCI". In: *Frontiers in neuroscience* 5, p. 112 (cit. on p. 25).

Strangman, Gary, David A. Boas, and Jeffrey P. Sutton (2002). *Non-invasive neuroimaging using near-infrared light* (cit. on p. 40).

Sturm, J.F. (1999). "Using SeDuMi 1.02, a MATLAB toolbox for optimization over symmetric cones". In: *Optimization Methods and Software* 11–12, pp. 625–653 (cit. on p. 108).

Sulaiman, Norizam et al. (2010). "Stress features identification from EEG signals using EEG Asymmetry & Spectral Centroids techniques". In: *Biomedical Engineering and Sciences (IECBES), 2010 IEEE EMBS Conference on*. IEEE, pp. 417–421 (cit. on p. 61).

Summerer, Leopold, Dario Izzo, and Luca Rossini (2009). *Chapter 16 Brain-Machine Interfaces for Space Applications-Research, Technological Development, and Opportunities* (cit. on p. 24).

Sun, Hongyu et al. (2010). "On-line EEG classification for brain-computer interface based on CSP and SVM". In: *Image and Signal Processing (CISP), 2010 3rd International Congress on*. Vol. 9. IEEE, pp. 4105–4108 (cit. on p. 70).

Tadel, François et al. (2011). "Brainstorm: a user-friendly application for MEG/EEG analysis". In: *Computational intelligence and neuroscience* 2011, p. 8 (cit. on p. 110).

Tangermann, Michael et al. (2012). "Review of the BCI competition IV". In: *Frontiers in neuroscience* 6, p. 55 (cit. on p. 123).

Thangudu, Kedarnath (2009). "Practicality of Discrete Laplace Operators". PhD thesis. The Ohio State University (cit. on p. 105).

Theodoridis, Sergios and Konstantinos Koutroumbas (2006). *Pattern Recognition, Third Edition*. Vol. 11, p. 984 (cit. on pp. 64, 131).

Tibshirani, Robert (1996). "Regression shrinkage and selection via the lasso". In: *Journal of the Royal Statistical Society. Series B (Methodological)*, pp. 267–288 (cit. on pp. 107, 109).

Ting, Wu et al. (2008). "EEG feature extraction based on wavelet packet decomposition for brain computer interface". In: *Measurement* 41.6, pp. 618–625 (cit. on p. 59).

Toh, Kim-Chuan, Michael J Todd, and Reha H Tütüncü (1999). "SDPT3—a MATLAB software package for semidefinite programming, version 1.3". In: *Optimization methods and software* 11.1-4, pp. 545–581 (cit. on p. 108).

Tütüncü, Reha H, Kim C Toh, and Michael J Todd (2003). "Solving semidefinite-quadratic-linear programs using SDPT3". In: *Mathematical programming* 95.2, pp. 189–217 (cit. on p. 108).

Vallabhaneni, Anirudh and Bin He (2013). "Motor imagery task classification for brain computer interface applications using spatiotemporal principle component analysis". In: *Neurological research* (cit. on p. 70).

Vattaa, Federica et al. (2010). "Solving the EEG forward problem by realistic and spherical head modeling: a comparative cortex-based analysis". In: *Computational Intelligence and Neuroscience* (cit. on p. 96).

Vidal, J J (1973). "Toward Direct Brain-Computer Communication". In: *Annual Review of Biophysics and Bioengineering* 2.1, pp. 157–180 (cit. on p. 17).

Vidaurre, Carmen et al. (2009). "Time domain parameters as a feature for EEG-based brain–computer interfaces". In: *Neural Networks* 22.9, pp. 1313–1319 (cit. on p. 53).

Volosyak, I, H Cecotti, and A Graser (2009). *Optimal visual stimuli on LCD screens for SSVEP based brain-computer interfaces* (cit. on p. 47).

Wallstrom, Garrick L et al. (2004). "Automatic correction of ocular artifacts in the EEG: a comparison of regression-based and component-based methods". In: *International journal of psychophysiology* 53.2, pp. 105–119 (cit. on p. 50).

Wang, Jiang et al. (2010). "Feature extraction of brain-computer interface based on improved multivariate adaptive autoregressive models". In: *2010 3rd International Conference on Biomedical Engineering and Informatics*. Vol. 2. IEEE, pp. 895–898 (cit. on p. 52).

Wang, Shaocheng, Ehsan Tarkesh Esfahani, and V. Sundararajan (2012). "EVALUATION OF SSVEP AS PASSIVE FEEDBACK FOR IMPROVING THE PERFORMANCE OF BRAIN MACHINE INTERFACES". In: *Proceedings of the ASME 2012 International Design Engineering Technical Conference & Computers and Information in Engineering Conference*. Chicago (cit. on p. 47).

Wang, Xiao-Wei, Dan Nie, and Bao-Liang Lu (2014). "Emotional state classification from EEG data using machine learning approach". In: *Neurocomputing* 129, pp. 94–106 (cit. on p. 61).

Wang, Yijun, YT Wang, and TP Jung (2010). "Visual stimulus design for high-rate SSVEP BCI". In: *Electronics letters* 46.15, p. 1 (cit. on p. 28).

Wang, Yijun et al. (2006). "Phase synchrony measurement in motor cortex for classifying single-trial EEG during motor imagery". In: *Engineering in Medicine and Biology Society, 2006. EMBS'06. 28th Annual International Conference of the IEEE*. IEEE, pp. 75–78 (cit. on p. 54).

Ward, B. Douglas and Yousef Mazaheri (2008). "Information transfer rate in fMRI experiments measured using mutual information theory". In: *Journal of Neuroscience Methods* 167.1, pp. 22–30 (cit. on p. 38).

Wei, Qingguo et al. (2007). "Amplitude and phase coupling measures for feature extraction in an EEG-based brain–computer interface". In: *Journal of Neural Engineering* 4.2, p. 120 (cit. on pp. 54, 55).

Weiskopf, Nikolaus et al. (2004). "Principles of a brain-computer interface (BCI) based on real-time functional magnetic resonance imaging (fMRI)". In: *IEEE Transactions on Biomedical Engineering* 51.6, pp. 966–970 (cit. on p. 38).

Wentrup, Moritz Grosse et al. (2005). "EEG source localization for brain-computer-interfaces". In: *Conference Proceedings. 2nd International IEEE EMBS Conference on Neural Engineering, 2005.* IEEE, pp. 128–131 (cit. on p. 141).

Wheeler, Robert E, Richard J Davidson, and Andrew J Tomarken (1993). "Frontal brain asymmetry and emotional reactivity: A biological substrate of affective style". In: *Psychophysiology* 30.1, pp. 82–89 (cit. on p. 61).

Wolpaw, Jonathan and Elizabeth Winter Wolpaw (2012). *Brain-computer interfaces: principles and practice*. OUP USA (cit. on pp. 30, 32).

Yi, Weibo et al. (2016). "EEG oscillatory patterns and classification of sequential compound limb motor imagery". In: *Journal of neuroengineering and rehabilitation* 13.1, p. 1 (cit. on p. 54).

Yosinski, Jason et al. (2015). "Understanding Neural Networks Through Deep Visualization". In: *Deep Learning Workshop, International Conference on Machine Learning (ICML)* (cit. on pp. 74, 75).

Yuan, Peng et al. (2013). "A study of the existing problems of estimating the information transfer rate in online brain–computer interfaces". In: *Journal of neural engineering* 10.2, p. 026014 (cit. on p. 26).

Zhang, Dan et al. (2007). "An algorithm for idle-state detection in motor-imagery-based brain-computer interface". In: *Computational Intelligence and Neuroscience* 2007, pp. 5–5 (cit. on p. 169).

Zhang, Huaijian, Ricardo Chavarriaga, and José del R Millán (2014). "Towards Implementation of Motor Imagery using Brain Connectivity Features". In: *6th International Brain-Computer Interface Conference*. EPFL-CONF-201757 (cit. on p. 172).

Zhang, Z (1995). "A fast method to compute surface potentials generated by dipoles within multilayer anisotropic spheres." In: *Physics in medicine and biology* 40.3, pp. 335–349 (cit. on p. 95).

Zou, Hui and Trevor Hastie (2005). "Regularization and variable selection via the elastic net". In: *Journal of the Royal Statistical Society: Series B (Statistical Methodology)* 67.2, pp. 301–320 (cit. on p. 109).